Nanoscale sensing with individual nitrogen-vacancy centers in diamond

A dissertation presented
by
Shimon Jacob Kolkowitz
to
The Department of Physics

in partial fulfillment of the requirements
for the degree of
Doctor of Philosophy
in the subject of
Physics

Harvard University
Cambridge, Massachusetts

December 2014

Dissertation Advisor: Professor Mikhail Lukin Shimon Jacob Kolkowitz

Nanoscale sensing with individual nitrogen-vacancy centers in diamond

Abstract

Nitrogen-vacancy (NV) centers in diamond have recently emerged as a promising new system for quantum information and nanoscale sensing applications. They have long coherence times at room temperature and can be positioned in proximity to the diamond surface, enabling magnetometry with high spatial resolution and coherent coupling to other quantum systems. This thesis presents three experiments in which single NV centers were used to sense magnetic fields at the nanometer scale. In the first experiment, the coherent evolution of a single NV spin is coupled to the motion of a magnetized mechanical resonator tens of nanometers from the NV. Coherent manipulation of the spin is used to sense the driven and Brownian motion of the resonator under ambient conditions, with picometer-scale sensitivity to motion. Future applications of this technique include the detection of the zero-point fluctuations of a mechanical resonator, the realization of strong spin-phonon coupling at a single quantum level, and the implementation of quantum spin transducers. In the second experiment, a single NV electronic spin is used to measure the quantum dynamics of distant individual nuclear spins from within a surrounding spin bath. The demonstrated sensing technique dramatically increases the potential size of NV based quantum registers for quantum information applications, and provides a new method for nanoscale magnetic resonance imaging of single nuclear spins. In the third experiment, single NV electronic spins are used to probe magnetic Johnson noise in the vicinity of conductive silver films. Measurements of polycrystalline silver films over a range of distances (20-200 nanometers)

and temperatures (10-300 Kelvin) are consistent with the classically expected behavior of the magnetic fluctuations. However, Johnson noise is found to be dramatically suppressed next to single-crystal films, indicative of a substantial deviation from Ohm's law arising from the ballistic motion of the electrons in the metal. These result demonstrate that our technique provides a general, non-invasive probe of local electron transport in samples of arbitrary size and dimensionality, which can be used to explore materials response to localized impurities and the interplay between transport, interactions and disorder at the nanoscale.

Contents

Listing of figures

For Liz, Ilan, Leah, and Dan.

Citations to previously published work

Chapter 3, in its entirety, has been published as

"Coherent Sensing of a Mechanical Resonator with a Single-Spin Qubit," S. Kolkowitz, A.C. Bleszynski Jayich, Q.P. Unterreithmeier, S.D. Bennett, P. Rabl, J.G.E. Harris, & M.D. Lukin, *Science* **335,** 1603 (2012).

Chapter 4, in its entirety, has been published as

"Sensing Distant Nuclear Spins with a Single Electron Spin," S. Kolkowitz, Q.P. Unterreithmeier, S.D. Bennett, & M.D. Lukin, *Physical Review Letters* **109,** 137601 (2012).

Chapter 5, in its entirety, has been published as

"Probing Johnson noise and ballistic transport in normal metals with a single spin qubit," S. Kolkowitz, A. Safira, A.A. High, R.C. Devlin, S. Choi, Q.P. Unterreithmeier, D. Patterson, A.S. Zibrov, V.E. Manucharyan, H. Park, & M.D. Lukin, *Science* **347,** 6226 (2015).

Acknowledgments

The work described in this thesis would not have been possible without the help, guidance, and support of many collaborators and friends. I would like to gratefully acknowledge their contributions here.

First, I would like to thank my PhD advisor, Mikhail Lukin. Over the past six and half years he has always been kind, encouraging, supportive, and patient with me. Misha has taught me a lot about physics, but just as importantly I have learned from his example how to maintain a happy work-life balance and a positive perspective. I could not be happier with how successfully the situation has developed.

I would also like to thank the other faculty who have collaborated with me on these experiments, Jack Harris from the Yale Physics department, Vladimir Manucharyan from the University of Maryland Physics department, and Hongkun Park from the Physics and Chemistry departments at Harvard. They provided invaluable resources, guidance, and comments, and I am very thankful for the opportunity to collaborate with such successful and impressive researchers. I also thank Amir Yacoby, Ron Walsworth, and Gerald Gabrielse for sitting on my qualifying exam and thesis committees.

Over the course of my PhD I was very lucky to have the honor of working closely with two fantastic post-docs, Ania Bleszynski Jayich and Quirin Unterreithmeier. Most of the experimental techniques, approaches to problem solving, and work ethic that I acquired during my PhD I owe to Ania and Quirin. I am fairly confident that other than members of my immediate family, no individuals have spent nearly as much one on one time with me as

Ania and Quirin have, and I thank them for putting up with me (it can't have been easy.) Not only did I learn a lot from them, but I also had a ton of fun along the way. Over the last two and half years I have also had the opportunity to work with fellow graduate student Arthur Safira, which has been a great experience. I thank him for all his hard work, and especially for being patient with me as I learned how to introduce and share an experiment with someone new. I would also like to thank my other experimental collaborators, Sasha Zibrov, David Patterson, Alex High, and Robert Devlin, for all their help and contributions to our experiments.

None of the work in this thesis would have been possible without the insights and support of several fantastic theorists, specifically Peter Rabl, who provided the original proposals for the work presented in Chapter 3, Steven Bennett, who helped interpret the results presented in Chapters 3 and 4, and Soonwon Choi, who helped with the theory presented in Chapter 5. It was a pleasure working with all of them.

I also want to recognize and thank my fellow lab mates, colleagues, and friends in the Lukin group, the Physics department, and the diamond community at Harvard, with whom I've had many stimulating discussions, and who have provided a lot of help and advice on my experiments over the years: Jeff Thompson, Nathalie de Leon, Tobias Tiecke, Igor Lovchinsky, Alex Sushkov, Nicholas Chilsholm, Alp Sipahigil, Michael Goldman, Ruffin Evans, Georg Kucsko, Peter Maurer, Brendan Shields, Alexey Akimov, Jero Maze, Patrick Maletinsky, Sungkun Hong, Mike Grinolds, Tim Baart, My Linh Pham, Nir Bar-Gill, Ofer Firstenberg, Norman Yao, Peter Komar, Frank Koppens, Dirk Englund, Jonathan Hodges, Yiwen Chu, Kristiaan de Greve, Eric Kessler, Emre Togan, Michael Gullans, Marc Warner, Elizabeth Petrik, Paul Hess, Ben Spaun, Alexey Gorshkov, Mohammad Hafezi, and Liang Jiang. It has been a pleasure and an honor to be in the company of so many distinguished, talented, and all-around nice individuals.

I also would like to acknowledge the NSF and the Defense Department for their financial

support throughout my PhD.

Finally, I would like to thank my family, friends, and my two cats, Luna and Io. I'd especially like to thank my bother Ilan, my mother Leah, my father Dan, and my wife Liz for their love and support. This thesis is dedicated to them.

Chapter 1

Introduction

1.1 Background

Since the invention of quantum mechanics roughly a century ago, the theoretical frameworks and technologies required for control over quantum systems have rapidly developed. In addition, over the last 30 years techniques to isolate single quantum systems have emerged, enabling the confinement and study of single electrons [1], atoms [2–4], ions [5], and molecules [6], and recently the engineering of "artificial atoms" in solid state materials [7–12]. These developments have given rise to the field of quantum information science, with promising applications such as quantum simulation, quantum computation, quantum communication, and quantum metrology. Just as importantly, if not more so, the same research has led to a number of fundamental technologies, such as lasers, atomic clocks, and nuclear magnetic resonance (NMR) spectroscopy and imaging (MRI), as well as a wide variety of applications in other branches of fundamental physics research, such as precision measurement of fundamental constants [13–15], laser frequency combs [16, 17], scanning tunneling microscopy (STM) [18], and superconducting quantum interference devices (SQUIDs) [19]. While the research presented in this thesis is motivated primarily by quantum information science applications, we also highlight and discuss applications to fundamental physics research and technology development.

1.1.1 Quantum information science

The unusual and counterintuitive properties of quantum mechanics, such as entanglement between particles at a distance, coherent superpositions of internal states, the Heisenberg uncertainty principle, and the no-cloning theorem, offer the tantalizing prospect of a new class of technologies which are impossible to implement classically speaking [20–23]. Broadly, these prospective technologies fall into four interrelated categories:

- **Quantum simulation, in which one "easy" to control quantum system is used to understand the behavior of another, less accessible, quantum system.** Some condensed matter phenomena, such as high temperature superconductivity, are not well understood, in part because they likely arise from complex quantum correlations. As a result, it is highly desirable to simulate complex quantum Hamiltonians to gain insights into these phenomena. Because the size of the Hilbert space of a quantum system scales exponentially with particle number, the simulation of interacting quantum systems on classical computers quickly becomes intractable. However, if the desired Hamiltonian can be reproduced using a different, well characterized quantum system, the number of quantum bits required will scale linearly with particle number [20, 21]. Early experiments in this direction have been performed using strings of ions [24, 25], and atoms in optical lattices [26, 27].

- **Quantum computation, in which computations are performed using quantum bits (qubits) and quantum gates.** It has been shown that a fully functioning quantum computer could solve certain classes of problems faster than a classical computer. For example, Grover's search algorithm can search an unsorted list of length N in a time that scales with $\sqrt{N}$ [28], while on a classical computer the time required scales linearly with N. Another well known example is Shor's algorithm for integer factorization [22], for which the computational time required to factor an integer scales

polynomial with the size of the integer, while for the best known classical algorithms the time scales exponentially. Consequently, the construction of a scalable quantum computer could render all classical public key encryption protocols insecure, as these protocols rely on the classical intractability of factorization of very large numbers. A quantum computer could also be used for "digital" quantum simulation of complex Hamiltonians. However, demonstrations of quantum algorithms have been limited to small numbers of bits [29–32], and at present the path towards scalable quantum computation remains unclear.

- **Quantum communication, in which secure communication at a distance is performed by sending a key using quantum bits over a quantum channel.** Fortunately, while the advent of quantum computing has the potential to disrupt present forms of secure public communication, quantum mechanics also offers a new way to securely distribute keys, with the privacy of the key physically guaranteed by the Heisenberg uncertainty principle and the no-cloning theorem [23]. Commercial systems for quantum key distribution are already on the market, but at present the distribution of keys with practical data rates is limited to distances of $\sim$5 mile or less, due to the exponential scaling of photon loss with length. This could be circumvented using quantum repeaters [33, 34], which can convert the exponential error scaling with distance to a linear scaling, but would require stationary qubits with long memories and strong coupling to single photons, and which have not yet been demonstrated at a practical level.

- **Quantum metrology, in which quantum systems are utilized for precision measurement and sensing applications.** Quantum systems are now widely used for sensing applications, such as clocks, magnetometers, gyroscopes, and accelerometers [35–40], for biological, medical and chemical applications such as NMR and MRI, and for the precision measurement of fundamental constants [13–15]. These measure-

ments rely on isolating the quantum system from the surrounding environment as much as possible in order to lengthen its coherence time, and thereby the sensitivity of the measurement, while simultaneously requiring the largest possible coupling to the signal of interest and excellent control and readout of the quantum system itself. Often an ensemble of many atoms or molecules is controlled and measured at once, in order to increase the signal-to-noise ratio of the measurement, and a growing area of quantum science research focuses on engineering non-classical states, such as spin-squeezed states [41–44] or maximally entangled Greenberger-Horne-Zeilinger (GHZ) states [45], to further increase the sensitivity of these ensembles.

While each of these categories has its own set of challenges, it is generally true that the largest outstanding hurdle to practical, scalable implementation of all four is the somewhat contradictory need for a well isolated qubit that still has strong, controllable, coherent interactions with other qubits or systems. There is therefore an active, field-wide search for the quantum system that can best satisfy this requirement, with a number of different promising systems currently being investigated.

1.1.2 Types of quantum systems

One of the most promising candidate systems for quantum information applications are trapped atoms. Neutral and charged atoms can be trapped and cooled in free space using electric and magnetic fields [2–5]. They have electronic orbital states with optical transitions between them that couple to photons, and hyperfine states that are insensitive to the environment and can be used as long-lived qubit states [46]. In addition, every atom of the same element is identical, enabling collective excitations of ensembles [34]. High fidelity two qubit gates have been demonstrated with trapped ions [47], and proof of principle experiments have demonstrated remote entanglement of atoms and ions [48, 49]. Quantum control of atoms has also found wide application in precision measurement and time-keeping,

with the second now defined using atomic clocks. The most accurate atomic clocks are now able to keep time so precisely that if one had been running constantly since the big bang, it would be accurate to better than one second [35]. In addition, there has been considerable research into the use of atoms and ions as ultrasenstive magnetometers [36], accelerometers [39], and gyroscopes [40].

Unfortunately, there are also drawbacks to the use of atoms for quantum information and sensing. A considerable amount of overhead is required to confine and cool atoms and ions, making scaling these systems up a daunting task. In addition, Casimir-Polder forces prevent the stable confinement of atoms less than $\sim$100 nm away from surfaces [50, 51], preventing atoms from taking full advantage of the large field enhancements afforded by plasmonic and nano-photonic devices[52], impeding integration with other quantum systems [53], and limiting the spatial resolution of atom-based magnetometers [54]. As a result, solid state "atom-like" systems, which reproduce many of the desirable properties of atoms inside a solid, have recently received considerable attention. A number of different promising solid state systems have emerged, including quantum dots, superconducting qubits, and atom-scale defects in crystals. This thesis presents research on quantum information and sensing applications with one particular member of the third category, the nitrogen-vacancy (NV) center in diamond.

1.2 Overview of this thesis

The rest of this thesis consists of five chapters. The first gives a basic introduction to nitrogen-vacancy centers in diamond. The bulk of the thesis then consists of three chapters, each describing a separate experiment performed using NV centers. Finally, there is a brief concluding chapter that summarizes the results presented in the previous three chapters, along with a discussion of ongoing work and future prospects.

1.2.1 Chapter 2: The nitrogen-vacancy center in diamond

In Chapter 2, we introduce the basic properties of NV centers, and some of the experimental techniques that are used throughout the experiments presented in the subsequent chapters.

1.2.2 Chapter 3: Sensing mechanical motion

In Chapter 3, we demonstrate coupling of the spin state of a single nitrogen-vacancy center to the motion of a macroscopic mechanical cantilever. We make use of one of the principle advantages of solid state defects, that they can be positioned remarkably close to surfaces while maintaining their desirable properties, to bring a magnetic tip on the end of an Atomic Force Microscopy (AFM) cantilever tens of nanometers from a single, optically resolvable, NV. We use continuous-wave electron spin resonance (CW ESR) to map the spatial profile of the magnetic fields emanating from the tip with the NV. Microwave manipulation of the spin is used to coherently sense the driven and Brownian motion of the resonator under ambient conditions. With future improvements, which we discuss, this technique could be used to realize strong spin-phonon coupling at a single quantum level. Entering this regime would enable the detection of zero-point fluctuations of the resonator and the implementation of a mechanical quantum spin transducer to engineer coherent coupling between NVs, or to efficiently couple the NV spin to optical or electrical signals for high-fidelity readout and long-range quantum communication applications.

1.2.3 Chapter 4: Sensing distant nuclear spins

In Chapter 4, we demonstrate that the same pulse sequences used in Chapter 3 to sense the motion of a mechanical resonator with an NV can be used to sense distant, weakly coupled ^{13}C nuclear spins in the diamond lattice. We show that the surrounding ^{13}C spin bath, often considered an undesirable nuisance, can serve as a useful resource. Specifically, we detect the evolution of distant individual ^{13}C nuclear spins coherently coupled to single

nitrogen vacancy centers in a diamond lattice with hyperfine couplings down to a factor of 8 below the electronic spin bare dephasing rate. We show that multiple ^{13}C spins coupled to a single NV can be isolated and identified, forming the basis for long-lived quantum registers. In addition, we discuss how these techniques could in principle be used to map the NV electron wave function, detect individual nuclear spins above the diamond surface, and to study the dynamics of spin baths.

1.2.4 Chapter 5: Probing Johnson noise and ballistic transport

In Chapter 5, we again take advantage of the proximity of shallow-implant NV centers to the diamond surface to probe magnetic field noise in the vicinity of conductive silver films. Thermally induced electrical currents, known as Johnson noise, cause fluctuating electric and magnetic fields in proximity to the silver, which are intrinsically related to the conductivity of the metal through Ohm's law and the fluctuation-dissipation theorem. Measurements of polycrystalline silver films over a range of distances (20-200 nm) and temperatures (10-300K) are consistent with the classically expected behavior of the magnetic fluctuations. However, we find that Johnson noise is dramatically suppressed next to single-crystal films, indicative of a substantial deviation from Ohm's law at length scales below the electron mean free path. Our results are in excellent agreement with a generalized model that accounts for the ballistic motion of electrons in the metal, indicating that under the appropriate conditions nearby electrodes may be used for controlling nanoscale optoelectronic, atomic and solid-state quantum systems. Our technique provides a general, non-invasive probe of local electron transport in samples of arbitrary size and dimensionality, which can be used to explore materials response to localized impurities and the interplay between transport, interactions and disorder at the nanoscale.

Chapter 2

The nitrogen-vacancy center in diamond

2.1 Introduction to nitrogen-vacancy centers

The nitrogen-vacancy (NV) center is a naturally occurring substitutional impurity in diamond, composed of a nitrogen atom that has replaced a carbon atom on one lattice site, and a missing carbon, or vacancy, on one of the four nearest neighbor lattice sites (see Fig. 2.1a). Although there are multiple stable charge states of the NV, all of experiments discussed in this thesis were performed with the NV^- configuration, which has 6 bound electrons; one from each of the three dangling bonds around the vacancy, two from the nitrogen atom, and one additional electron from a donor elsewhere in the diamond. For the remainder of this thesis we refer to the NV^- charge configuration when discussing the NV center. NVs can be selectively generated in an ultra-pure diamond samples at the desired depth and density, either through nitrogen ion implantation[55, 56], or by nitrogen introduction through doping during the diamond growth process [57].

The NV center has a number of unusual properties that make it promising for both quantum information and sensing applications. In particular, it has a ground state electronic spin triplet with long coherence times at room temperature (>1 ms) [58–60], a strong optical transition at 637 nm that can be close to lifetime limited when cooled below 10 K [61, 62], and spin-dependent transitions in the electronic excited state that give rise to both

spin dependent fluorescence rates and optical spin polarization at room temperature. The NV spin can be used as a probe of local magnetic [37, 38, 63–67] and electric [68] fields, temperature [69, 70], and strain [71]. In addition, NVs can display these same properties in particles of diamond less than 10 nm in diameter [72], enabling these measurements at the end of scanning tips [65, 73] or inside living cells [70].

2.2 Basic experimental techniques to control NV centers

While the NV level structure and the techniques for measuring and manipulating its electronic spin state are well established and have been discussed in detail in a number other works [11, 12, 74], a few of the basics are worth reviewing here, as they are used repeatedly throughout this thesis. A basic diagram of the NV level structure is shown in Figure 2.1b. The electronic ground state ($|g\rangle$) is a spin triplet, with a zero field splitting $\Delta \sim 2\pi\times 2.88$ GHz between the $|m_s = 0\rangle$ and the $|m_s = \pm 1\rangle$ spin states. Off-resonant excitation with 532 nm laser light pumps the NV into the optical excited state ($|e\rangle$), which has a lifetime of ∼12 ns in bulk diamond. An intersystem crossing in $|e\rangle$ takes some of the population from the $|m_s = \pm 1\rangle$ manifold to the metastable shelving singlet $|s\rangle$, which has a relatively long lifetime of ~ 300 ns, before preferentially decaying down to the $|m_s = 0\rangle$ spin state in $|g\rangle$. The fortuitous end result is that 532 nm illumination both optically polarizes the NV in the $|m_s = 0\rangle$ spin state, and also returns a spin-state dependent fluorescence rate. NVs can be individually addressed and read-out using a standard confocal microscope, as shown schematically in Figure 2.1c, with a 2-axis mirror galvanometer used for raster scanning the sample, and the resulting fluorescence detected using an avalanche photo diode (APD). A confocal image of a sample with a representative density of NVs implanted $\sim 10 - 20$ nm below the surface is shown in Figure 2.1d.

Once polarized, the spin of a single NV can be manipulated using resonant microwaves, which are applied via a coplanar waveguide (CPW) as shown in Figure 2.1c. The degeneracy

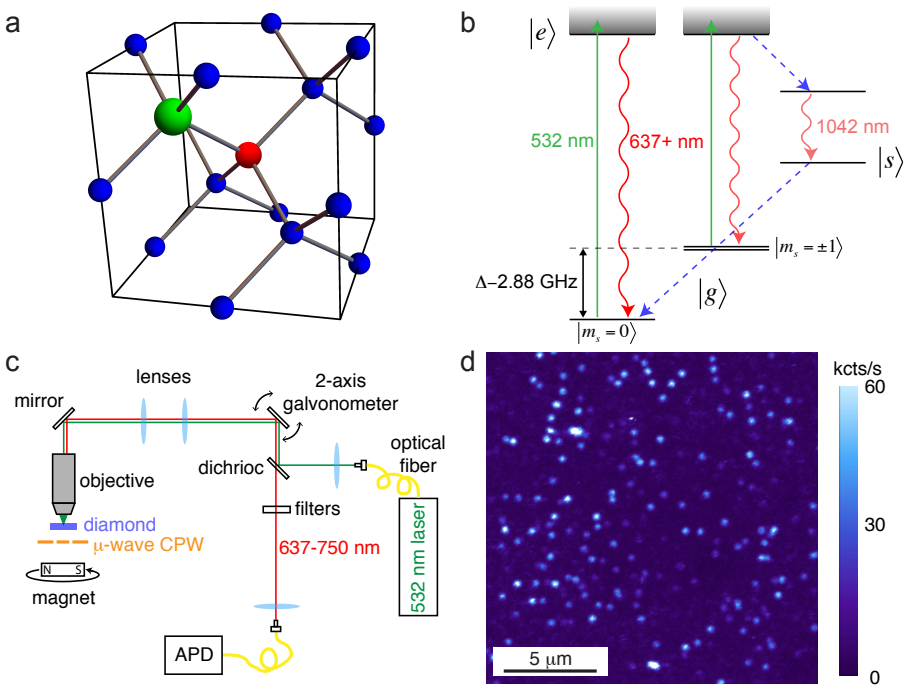

Figure 2.1: Nitrogen-vacancy centers in diamond. (a) Structure of a single nitrogen-vacancy defect center in a diamond lattice. Blue spheres are carbon atoms, the red sphere is a nitrogen atom, and the larger green sphere is a vacancy. (b) Simplified NV level structure. The ground state spin triplet ($|g\rangle$) has a zero field splitting $\Delta \sim 2\pi\times 2.88$ GHz between the $|m_s = 0\rangle$ and the $|m_s = \pm 1\rangle$ spin states. Illumination with 532 nm excites from $|g\rangle$ to the excited state $|e\rangle$ through the vibronic sideband (grey continuum). (c) Illustration of the confocal setup design used (with experiment specific modifications) for all work presented in this thesis. (d) Confocal image taken using the setup illustrated in (c) of single NV centers centers implanted ~20 nm below a diamond surface.

between the $|m_s = \pm 1\rangle$ states can be lifted by a applying a magnetic field ($B_{||}$) along the axis defined by the nitrogen-vacancy bond, resulting in a d.c. Zeeman shift of the $|\pm 1\rangle$ states by $\delta_B = \pm g\mu_B B_{||}$, with the magnetic moment $g\mu_B/\hbar = 2\pi\times$ 2.8 MHz/Gauss. The resulting shifts in energy can be measured using continuous-wave electron spin resonance (CW ESR), as shown in Figure 2.2a, in which the NV is continuously addressed with both microwaves and 532 nm laser light, and the resulting fluorescence is measured as a function of microwave frequency. The two dips in fluorescence correspond to the transitions from the brighter $|0\rangle$ state to the dimmer $|\pm 1\rangle$ states, at $\omega_\pm = \Delta \pm 2g\mu_B B_{||}/\hbar$. Tuning the microwaves to one of

these two transitions, for example ω_-, effectively converts the NV spin from a three level system to a two-level qubit, with population remaining entirely in the $|0\rangle, |-1\rangle$ states for any experiment that is shorter than the NV spin longitudinal relaxation time T_1, which at room temperature is ~ 5 ms, and at low temperature can be seconds or even minutes [75]. Applying resonant microwaves drives the transition, resulting in Rabi oscillations between the two states as shown in Figure 2.2b, which can be used to transfer population back and forth between the two spin states by applying the drive for a half period of the oscillation, known as a π-pulse.

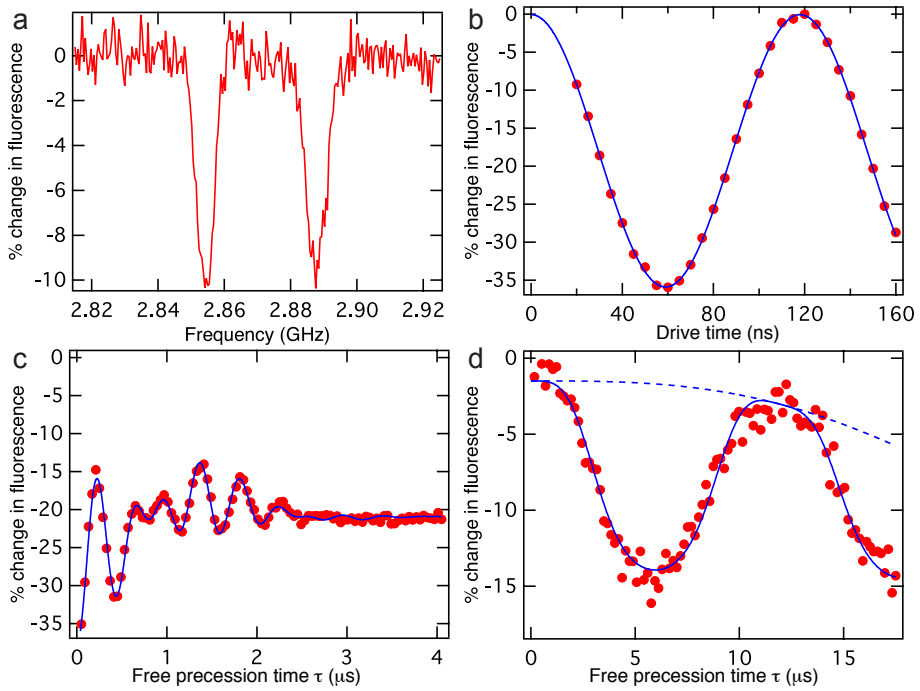

Figure 2.2: NV spin manipulation (a) Continuous-wave electron spin resonance (CW ESR) signal from a single NV center at a magnetic field of ~10 Gauss. (b) A pulsed Rabi experiment (red data) showing Rabi flopping between the $|m_s = 0\rangle$ and $|m_s = -1\rangle$ state as a function of microwave drive time. The blue curve is a cosine fit. (c) A pulsed Ramsey experiment (red data), with beating between the three ^{14}N hyperfine states visible. The blue curve is a fit to the sum of three cosines. (d) A pulsed spin echo experiment (red data) with a collapse and revival in coherence of the NV spin resulting from the Larmor precession of the surrounding C^{13} nuclear spin bath. The solid blue curve is a fit to the expected signal, while the dashed blue curve shows the extracted decay of the overall coherence envelope.

2.2.1 The Ramsey sequence

Driving for a quarter of a Rabi period, called a $\pi/2$-pulse, will leave the NV in a coherent superposition of the two spin states, $|\Psi\rangle = \frac{1}{\sqrt{2}}(|0\rangle + e^{i\phi}|-1\rangle)$, where ϕ is the relative phase between the $|0\rangle$ and $|-1\rangle$ states. Left in this state for time τ, the $|-1\rangle$ state will acquire a relative phase $\phi = \delta\tau$, where δ is the detuning between the driving field and the transition frequency ω_-. The application of a second $\pi/2$-pulse will convert the phase ϕ into a population difference between the two spin states, which can be measured by fluorescence. This is known as a Ramsey sequence [76], and as it is sensitive to the energy difference between the $|0\rangle$ and $|1\rangle$ states it can be used to the measure the d.c. magnetic field along the NV axis. The outcome of a Ramsey measurement is shown in Figure 2.2c, with the three visible oscillation frequencies ($\delta, \delta + 2.2$ MHz,$\delta - 2.2$ MHz) arising from the hyperfine coupling of the NV electronic spin state $|-1\rangle$ to the three nuclear spin states ($m_I = 0, -1, +1$) of this NV's nitrogen-14 (^{14}N) nucleus [12]. It is important to note that the experiments shown in Figure 2.2b,c and d are all the averaged outcome of many thousands of iterations of the same measurement sequence, as each sequence returns on average less than a single photon before the NV is re-polarized into the $|0\rangle$ state.

2.2.2 The nuclear spin bath and the spin echo sequence

Also apparent in Figure 2.2c is an overall exponential decay of the Ramsey oscillations with a timescale $T_2^* = 1.7$ μs. This timescale is the result of slowly varying magnetic fields that contribute a random accumulated phase for each measurement, which when averaged over multiple measurements results in dephasing of the superposition. These fluctuating fields are generated by the flip-flops of nearby carbon-13 (^{13}C) nuclear spins in the surrounding diamond lattice, which in a sample of natural isotopic abundance occupy 1.1% of the lattice sites. Unfortunately, this limits the d.c. sensitivity of NV based magnetometers, as it restricts the length of a Ramsey measurement sequence to T_2^*. One solution is to eliminate

the ^{13}C bath entirely, using artificial diamonds grown with isotopically enriched carbon [59, 60]. However, due to the expensive nature of the growth and enrichment processes very few of these samples currently exist, and in some cases, as discussed in Chapter 4 of this thesis, the ^{13}C bath can actually serve as a resource and it may be desirable not to eliminate it. Fortunately, T_2^* does not set a limit on the sensitivity of NV magnetometers to a.c. fields, nor on the NV coherence time for use as a quantum memory, thanks to a technique originally developed in NMR known as dynamical decoupling. The simplest version of this technique is the spin echo sequence, which is comprised of a Ramsey sequence of length 2τ, with a π-pulse applied half way through after free precession time τ. During the first period of free precession the superposition will acquire a relative phase $\phi_1 = \delta_1\tau$, where δ_1 is the detuning of the microwaves from resonance during that period, and includes the ^{13}C contribution. The π-pulse flips the sign of the phase to $-\phi_1 = -\delta_1\tau$, such that after the second precession period the total accumulated phase is given by $\phi_t = \phi_2 - \phi_1 = (\delta_1 - \delta_2)\tau$, and it is immediately apparent that if $\delta(t)$ is only slowly varying over the timescale 2τ, as is the case for the ^{13}C bath, the echo sequence will cancel it out entirely, while remaining maximally sensitive to a.c. fields with period 2τ. The outcome of a spin echo measurement is shown in Figure 2.2d, demonstrating that coherence can be extended far beyond T_2^*. The collapse and revivals in the coherence is a product of the Larmor precession of the surrounding ^{13}C spins in the applied magnetic field B at the Larmor frequency $\omega_L = \gamma_N B$ (here $\sim$80 kHz,) and illustrates the sensitivity of this measurement to a.c. magnetic fields. An overall decay in coherence of the spin echo signal is also visible (dashed line,) with a timescale of T_2 =50 μs, but the coherence can be extended even further using more sophisticated dynamical decoupling sequences [77–80], which are used and discussed in detail in Chapters 3 and 4.

Chapter 3

Coherent sensing of a mechanical resonator with a single NV spin

3.1 Introduction

Hybrid quantum systems offer many potential applications in quantum information science and quantum metrology. One example is cavity quantum electrodynamics (cQED), in which a quantum two-level system (a qubit) is strongly coupled to resonant photons in an electromagnetic cavity [76, 81, 82]. In the mechanical analogue of cQED the qubit is coupled to a mechanical resonator, with resonant phonons playing the role of cavity photons [83–86]. Mechanical resonators are promising components for hybrid quantum systems because they couple to a wide range of forces while maintaining high quality factors [53, 87–91], and can be fabricated using scalable techniques. A recent experiment demonstrated coupling of a superconducting phase qubit to the quantum motion of a piezo-electric resonator at milliKelvin temperatures [89]. However, this approach resulted in relatively short phonon lifetimes, and is not easily extended to other resonator-qubit systems. An important goal is to extend this technique to non-piezoelectric resonators that offer longer phonon lifetimes, and to qubits featuring longer coherence times [53, 83, 84, 88, 92, 93]. In particular, spin states of localized atom-like systems in solid-state can be manipulated individually and can serve as an exceptional quantum memory, even under ambient conditions. Moreover, exper-

iments have demonstrated that resonators can be sensitive to the magnetic force associated with a single electronic spin [94]. Control over a coupled spin-resonator hybrid quantum system could be used to mediate long-range spin-spin coupling for quantum information applications [95], or to manipulate mechanical motion at the single quantum level with long qubit and phonon coherence times [83, 89]. In addition, coherent control over spin-phonon interactions is of direct relevance for realizations of novel nanoscale sensors [63, 73, 96].

3.2 Key concepts of the experiment

In our experiment (Figure 3.1a) we utilize the electronic spin associated with an individual NV center to sense the motion of a nearby, magnetized atomic force microscopy (AFM) cantilever. The time-varying magnetic field generated by the displacement of the magnetic tip coherently drives the qubit evolution, which is subsequently detected via optical spin measurements. The essence of our approach (Figure 3.1b) is to synchronize the evolution of the single spin with the cantilever's oscillations. When the spin is driven by a pulse train with a period matching the mechanical period, the motion constructively impacts the spin evolution over a long interaction time, enhancing the spin's sensitivity in a narrow frequency band [97]. In addition, the pulses dynamically decouple the NV spin from the slow evolution of the surrounding environment, increasing the possible interrogation time [38, 77].

The NV centers are implanted ∼5 nm below the surface of a bulk diamond sample. The spin sublevels $|m_s = 0\rangle$ and$|m_s = \pm 1\rangle$ of the electronic ground state exhibit a zero-field splitting of ~ 2.88 GHz. In the presence of a static magnetic field the degeneracy between $|+1\rangle$ and $|-1\rangle$ is lifted, allowing us to selectively address the $|0\rangle \rightarrow |+1\rangle$ transition with microwave radiation. The magnetic field $\mathbf{B_{tip}}$ generated by the tip at the position of the NV results in an additional Zeeman shift of the splitting, given by $\Delta\omega = g_e \mu_B \mathbf{B_{tip}} \cdot \hat{\mathbf{z}}/\hbar$, where $g_e \approx 2$ is the electron g-factor, μ_B is the Bohr-magneton, $\hbar$ is Planck's constant divided by

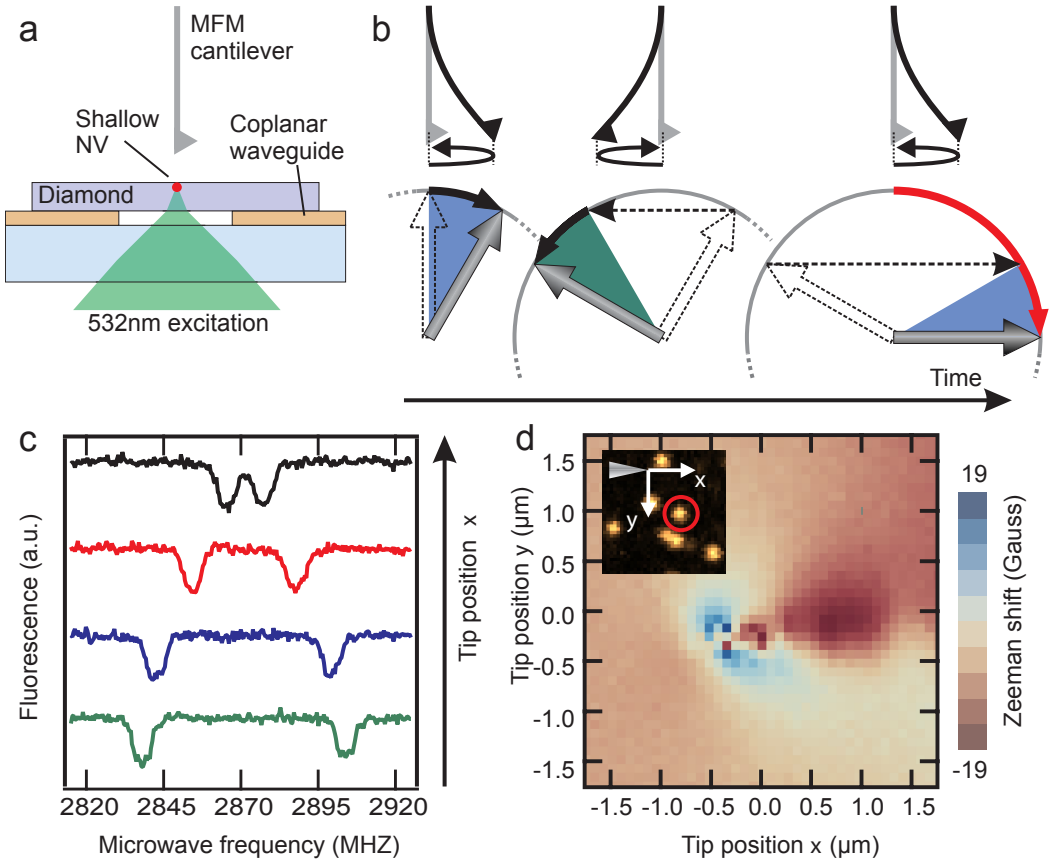

Figure 3.1: Concept of the experiment. (a) A magnetized AFM cantilever tip is positioned within tens of nanometers of a shallow implant NV in bulk diamond. (b) The control pulse sequence is matched to the period of the mechanical resonator in order to constructively accumulate phase from the oscillations. The green and blue shaded regions show the accumulated phase of the spin during one half period, and the horizontal dashed arrows the effect of the microwave π-pulses. (c) CW-ESR spectra showing the transitions between the $|m_s = 0\rangle$ and$|m_s = \pm 1\rangle$ ground states of the NV as the tip is moved parallel to the axis of cantilever oscillations. A 12 Gauss external magnetic field is applied opposite the static field from the tip. The four traces correspond to $\sim$ 100 nm steps towards the NV. (d) Scanning the tip at a fixed height above the surface we extract a 2D map of the DC field from the tip along the NV axis. Five pixels for which the shift could not be extracted were interpolated. The inset shows a fluorescence image of the diamond surface, with the NV used for this map circled in red.

2π, and $\hat{\mathbf{z}}$ is the unit vector along the NV axis. With the tip held at a constant position, the static Zeeman shift is detected by performing continuous wave (CW) electron spin resonance (ESR) measurements (Figure 3.1c) By scanning the tip at a fixed height above the diamond surface with a piezoelectric scanning stage and monitoring $\Delta\omega$ we map the projection of $\mathbf{B_{tip}}$ along the NV axis (Figure 3.1d). This provides an accurate measurement of the magnetic field gradient G_m produced by the tip along the NV axis, which reaches up to 10^5 T/m, see Appendix A.2 for further details.

The gradient G_m translates mechanical oscillations of the cantilever $x_{ac}(t)$ into an oscillating magnetic field $B_{tip,ac}(t) = G_m x_{ac}(t)$. Coherent control over the NV spin is used to measure $B_{tip,ac}$ via pulsed ESR techniques such as spin echo and longer dynamical decoupling sequences [37, 38, 63]. In order to probe Brownian motion, which has a characteristic frequency but a randomly varying amplitude and phase, our measurement sequence cannot be phase-locked to the mechanical oscillation. For this reason we measure the variance of the accumulated phase, yielding the mean square field amplitude $\langle B_{tip,ac}^2 \rangle$. From $\langle B_{tip,ac}^2 \rangle$ and G_m the mean square motional amplitude $\langle x^2 \rangle$ can be inferred, which for an undriven resonator is related to the thermal occupation number, $\bar{n}_{\mathrm{th}} = \frac{k\langle x^2 \rangle}{\hbar\omega_r}$.

3.3 Detecting driven motion

In the measurement sequence used to detect $\langle x^2 \rangle$ (Figure 3.2a) the NV's electronic spin is polarized in the $|0\rangle$ state via green illumination [12, 38]. Resonant microwaves tuned to the $|0\rangle \rightarrow |+1\rangle$ transition are applied to perform a Hahn echo sequence with free precession periods of length τ. The final $\pi/2$ pulse of the sequence converts the relative accumulated phase into a population difference that is read out via fluorescence [38] (Figure 3.2b). With the cantilever drive switched off the data (blue triangles) demonstrate collapses and revivals in spin coherence due to nearby Carbon-13 (^{13}C) nuclear spins undergoing Larmor precession at frequency $\omega_{nuc} = \gamma_{nuc} B_{dc}$, where $\gamma_{nuc}/2\pi$=1.07 kHz/Gauss is the gyromagnetic

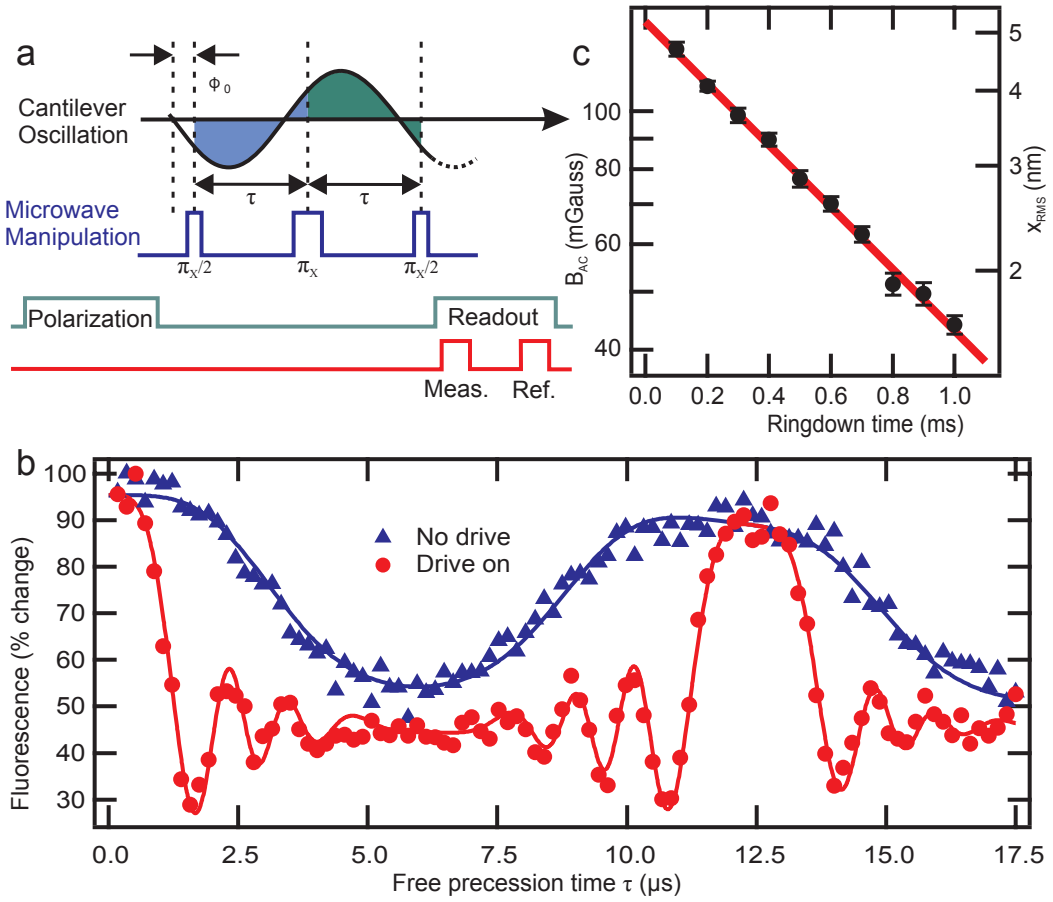

Figure 3.2: Detection of driven motion. (a) Hahn echo pulse sequence. The relative phase ϕ_o varies for each measurement. (b) Spin echo measurement with cantilever nearby with the drive switched off (blue triangles,) and with the drive on (red circles.) The Larmor precession of the ^{13}C is tuned close to the mechanical frequency $\omega_r/2\pi = 80.15$ kHz via an external magnetic field of $B_{dc} \approx 78$ Gauss. (c) Amplitude of a.c. magnetic field (left axis) and motional amplitude (right axis) as a function of wait time after switching off the drive, measured using spin echo. Here G_m=2707 $\pm$ 325 T/m. The error bars correspond to the uncertainty in a.c. magnetic field (left axis).

ratio of the ^{13}C nuclei [12, 38]. The ensemble of ^{13}C nuclei produces an oscillating field with fluctuating amplitude and phase, resulting in collapses in coherence at odd multiples of π/ω_{nuc}, and revivals at even multiples of π/ω_{nuc} [38]. Here the tip is positioned relatively far from the NV, producing a weak gradient of $G_m = 100 \pm 12$ T/m, so in the absence of an external drive the Brownian motion can be ignored and the field from the tip can be considered static. The red circles show the same measurement with the cantilever strongly driven. The evolution of the NV spin is dramatically affected by the cantilever motion. The revival is narrowed and shifted to $\tau = 2\pi/\omega_r$ due to $B_{tip,ac}$. Because the spin evolution is not phase-locked to the mechanical oscillation, $B_{tip,ac}$ has a constant amplitude but a uniformly distributed random initial phase ϕ_o for each measurement, resulting in an echo signal given by a zeroth order Bessel function (see Appendix A.5). By fitting to this data we determine the peak amplitude $B_{tip,ac} = 163 \pm 1$ milliGauss, and the oscillation frequency $\omega_r/2\pi = 80.14 \pm 0.07$ kHz, in agreement with the applied excitation frequency of 80.15 kHz. Incorporating the previously measured G_m, the root mean square (rms) amplitude of the tip motion, $x_{rms} = 114 \pm 14$ nm, can be extracted (see Appendix A.3).

To measure the quality factor of the resonator (Figure 3.2c) the resonator is driven to a fixed amplitude of motion, the drive is switched off, and we subsequently measure x_{rms} as a function of wait time after turning off the cantilever drive using the same protocol as in Figure 3.2b. A quality factor of $Q = 211 \pm 6$ is extracted from the exponential decay of x_{rms}, in agreement with measurements made independently using conventional interferometric readout of the cantilever motion which yield $Q = 221 \pm 4$.

3.4 Detecting thermal motion

Under ambient conditions the $\omega_r/2\pi = 80.15$ kHz resonator with a spring constant of $k \approx 3$ N/m has a thermal occupation number of $\bar{n}_{th} \approx 8 \times 10^7$ phonons, corresponding to Brownian motion with an rms amplitude of ~ 40 pm. To detect these oscillations with the single spin,

we use a pulse sequence composed of N π-pulses known as XY4 [77] (Figure 3.3a). This sequence further suppresses the effects of low frequency magnetic noise and enhances the a.c. sensitivity by a factor of $\sim 1/(N^{3/2})$ in a narrow bandwidth [77, 97]. It also has the advantage of self-correcting pulse errors to first order for any accumulated phase of the NV spin [77].

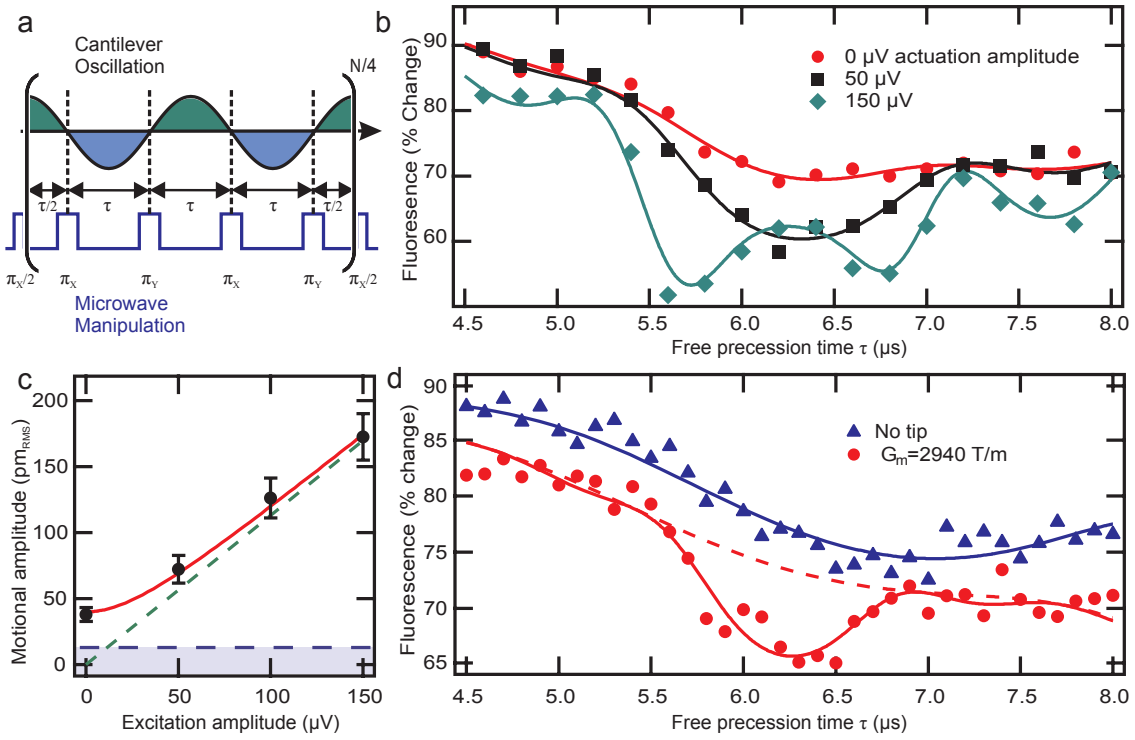

Figure 3.3: Detection of Brownian motion. (a) XY4 pulse sequence. (b) XY4 measurement with $N = 12$ π-pulses for four different driving voltages (the 100 μV curve is excluded for clarity) at G_m= 2978 $\pm$ 268 T/m. The fits account for Brownian and driven motion. (c) Extracted rms amplitude from (b) as a function of driving voltage. The red curve shows the expected rms amplitude based on independent calibrations including thermal and driven motion, while the green dashed line is expected from driven motion alone. Neither line has any free parameters. The dashed blue line shows the estimated minimum detectable motion for the measurements in (b). (d) XY4 measurement with $N = 16$ π-pulses, with the tip nearby at G_m =2940 $\pm$ 265 T/m (red circles) and without the tip (blue triangles). Solid lines are fits. The dashed red line shows the expected signal in the presence of a static tip with no Brownian motion.

We use an XY4 sequence with $N = 12$ π-pulses to measure resonator motion at excitation amplitudes of $\sim$(0,57,113,170) pm of rms driven motion (Figure 3.3b). Unlike the measurements shown in Figure 3.2, $B_{ext,dc}$ is tuned to a low value of $\sim$ 10 Gauss to extend the onset of the first collapse in spin coherence due to the ^{13}C nuclei's Larmor precession beyond the resonator induced partial collapse (see Appendix A). The multiple minima at 170 pm of rms driven motion (green diamonds) are described by a Bessel function as discussed above (see Appendix A.5). Extracting x_{rms} from the fits in Figure 3.3b and plotting against the a.c. driving voltage, the inclusion of Brownian motion is necessary to achieve good agreement with the data (Figure 3.3c). The impact of Brownian motion on the spin is also directly evident in Figure 3.3b in the slight dip in the undriven data (red circles) at $\tau = \pi/\omega_r$ =6.2 μs.

To further enhance the impact of Brownian motion on our NV spin we use an XY4 sequence with $N = 16$ π-pulses, allowing the spin to accumulate more motion-induced phase in a single measurement (Figure 3.3d). With the tip nearby at a gradient of 2940 $\pm$ 265 T/m, the Brownian motion induces a collapse in the NV spin coherence at $\tau = \pi/\omega_r$. The fits yield $x_{rms} = 40\pm5$ pm and $\omega_r/2\pi = 79.7\pm0.4$ kHz, in agreement with the expected value of $\sim$ 40 pm and the resonance frequency of 80.15 kHz. This corresponds to $B_{tip,ac} = 117 \pm 9$ nT rms. The tip's proximity to the NV affects the spin coherence, resulting in the offset between the two curves.

Several recent experiments have reported that strongly driven mechanical resonators can influence the electronic spin of NV centers through the broadening and shifting of the spin transitions [63, 93, 96]. Our approach takes advantage of the fact that the NV spin remains coherent for times much longer than the relatively short T_2^* [12]. This longer interaction time enhances the spin's sensitivity to the resonator's motion [37, 38], and enables the detection of picometer-scale oscillations without phase locking.

3.5 Present sensitivity and future outlook

To understand the present sensitivity limits and the potential for improvement, we consider a measurement of an undriven cantilever as in Figure 3.3d. When the pulse sequence is synchronized with the cantilever such that $\tau = \pi/\omega_r$, the probability P_1 to find the spin in state $|1\rangle$ after the sequence is $P_1 = \frac{1}{2}\left(1 + e^{-N(\pi/\omega_r T_2)^3}\right) - S$, where we isolated the signal S due to the cantilever motion (see Appendix A.6),

$$S \simeq \frac{1}{2} e^{-N(\pi/\omega_r T_2)^3} \left(1 - e^{-2N^2\lambda^2(2\bar{n}_{\rm th}+1)W/\omega_r^2}\right). \tag{3.1}$$

Here, the coupling rate $\lambda = g_e \mu_B G_m a_0/\hbar$ is the Zeeman shift from a single phonon in the resonator, and $a_0 = \sqrt{\hbar/2m\omega_r}$ is the zero point motion for a resonator of effective mass m. T_2 is the spin coherence time in the absence of the cantilever, while the exponent proportional to λ^2 describes the impact of the cantilever motion and depends on the mechanical Q as well as the bandwidth of the control sequence through the factor $W = (1 + N/2Q)^{-1}$. The contribution from thermal motion is proportional to $\bar{n}_{\rm th}$ and the remainder is due to quantum zero point motion. Using Eq. (3.1) and including spin projection and shot noise through the single parameter K [37], we obtain the phonon number sensitivity $\eta = \bar{n}_{\rm min}\sqrt{t_{\rm tot}} = \frac{\sqrt{\pi}}{2KW\lambda^2} e^{N(\pi/\omega_r T_2)^3} \left(\frac{\omega_r}{N}\right)^{3/2}$, where $\bar{n}_{\rm min}$ is the minimum detectable phonon occupation number in total measurement time $t_{\rm tot}$. For the experimental parameters of Figure 3.3d we obtain $\eta \approx 2.5 \times 10^8$ phonons/$\sqrt{\rm Hz}$, in agreement with the observed experimental sensitivity $\eta_{exp} \approx 4.9 \times 10^8$ phonons/$\sqrt{\rm Hz}$ (see Appendix A.6).

The main factor currently limiting our sensitivity is the coupling strength λ. While we measure gradients up to 10^5 T/m, which gives $\lambda/2\pi \approx 8$ Hz, our most sensitive measurements are taken at $\sim 3 \times 10^3$ T/m. The lower gradient is used because T_2 is found to decrease when the magnetic tip is very close to the NV; we observe a reduction of T_2 from ~ 160 μs when the tip is retracted to as low as ~ 5 μs when the tip is within 50 nm of

the surface. Our use of XY4 dynamical decoupling sequences partially compensates for this effect, indicating that the reduction in T_2 is due to low frequency noise, which we attribute to magnetic domain noise of the tip material. We expect this effect can be mitigated using alternative tip materials such as rare earth ferromagnets [98]. The coupling strength can be further improved by using customized nano-resonators with a larger zero point motion. Using state of the art nano-fabrication techniques resonators with $Q > 10^6$, $\omega_r/2\pi \sim 1$ MHz [99], $G_m \sim 10^5$ T/m, and a coupling strength of $\lambda/2\pi \sim 10$ kHz can be fabricated [83], which together with extended coherence times in isotopically purified diamond of $T_2 > 2$ ms [59] and faster pulse sequences with $N \sim 136$ pulses [77] yield a projected sensitivity of $\eta < 1$ phonon/$\sqrt{\text{Hz}}$. Combined with recently demonstrated single shot spin readout [100] this raises the intriguing prospect of using a single NV center to sense mechanical motion at the scale of zero point fluctuations in a single shot.

To assess the feasibility of sensing zero point motion (Figure 3.4a) we assume that the resonator is actively cooled near its motional ground state, using either the spin [83] or an additional system such as an optical or microwave cavity [90, 91]. Such cooling schemes are always accompanied by a decreased effective mechanical quality factor, $Q_{\text{eff}} = Q/\bar{n}_{\text{env}}$, where $\bar{n}_{\text{env}}$ is the phonon occupation number at the temperature of the surrounding environment. Inserting $\bar{n}_{\text{th}} = 0$ and $W = 2Q_{\text{eff}}/N$ into Eq. (3.1), a near maximal signal $S \sim 1/2$ is obtained provided that $C = \lambda^2 Q_{\text{eff}} \tilde{T}_2/\omega_r > 1$, where $\tilde{T}_2 = T_2 N^{2/3}$ is the extended spin coherence time due to dynamical decoupling [77]. This is verified in Figure 3.4b, which demonstrates that for a wide range of realistic parameters with $C > 1$ the zero point motion of the resonator results in $S \sim 1/2$. The parameter C is a fundamental quantity in the physics of spin-phonon interactions. In direct analogy to the so-called cooperativity in cQED, $C > 1$ marks the onset of coherent quantum effects in a coupled spin-phonon system. Taking the optimized but realistic values $\lambda/2\pi$ =10 kHz, $T_2 = 1$ ms, $Q = 10^6$, $\omega_r/2\pi = 1$ MHz, and N=160 pulses, we find that $C \sim 35$ can be reached at an environmental tem-

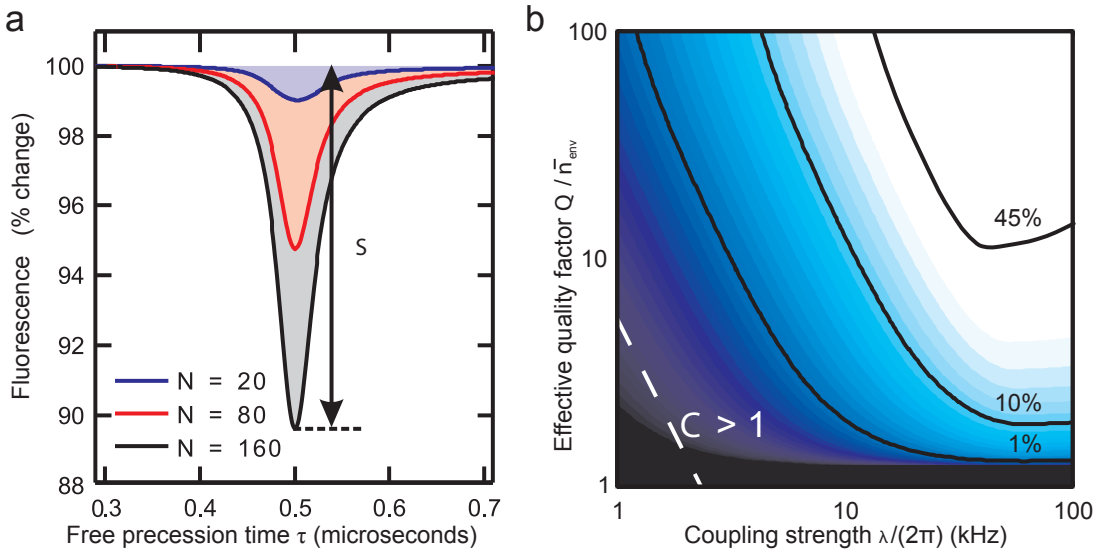

Figure 3.4: Prospects for detection of zero-point motion. (a) Calculated XY4 signal for a cantilever cooled near its ground state, starting from an environmental temperature of $T_{\rm env} = 4$ K. The signal S is the measurable impact from cantilever motion. Parameters are $\omega_r/2\pi = 1$ MHz, $\lambda/2\pi = 10$ kHz, $T_2 = 1$ ms, $Q = 10^6$. (b) Signal S versus coupling strength and effective quality factor. The white line marks the threshold of strong cooperativity, $C = \lambda^2 Q_{\rm eff}\tilde{T}_2/\omega_r > 1$. At each point we optimize the pulse number N within the experimental limitation of $N_{\rm max} \leq 160$, as shown to be feasible in recent experiments [77, 97]. The slight upturn of the contours at large coupling is due to cantilever-induced decoherence (see Appendix A); this small correction is neglected in Eq. (3.1).

perature of T= 4 K. Besides detection of zero point motion, entering this regime could also enable coherent, long-range interactions between individual spins mediated by a mechanical resonator [95], which are of great interest for developing scalable spin-based quantum information systems. Furthermore, by operating at lower environmental temperatures of $T \sim 100$ mK, it becomes possible to use the spin to cool the resonator down to its ground state [83] and to engineer quantum superpositions of mechanical motion, which could be read out using a coherent detection scheme like the one presented in this chapter.

The above considerations indicate that our approach provides an experimentally feasible route toward reaching strong coupling between single phonons and spins. Potential

applications ranging from the creation and detection of quantum states of mechanical motion and the realization of quantum spin transducers to novel approaches for nanoscale sensing and readout [73, 96] can be foreseen.

Chapter 4

Sensing distant nuclear spins with a single NV spin

4.1 Introduction

Detection and control of the magnetic signals from nuclear spins is an important problem in science and technology. Single nuclear spin detection remains an outstanding goal in magnetic resonance imaging (MRI), with far-reaching implications from physics to medicine [94, 101, 102]. Likewise, nuclear spins stand out in quantum information science for their exceptional isolation from their environment, making them attractive qubit candidates. However, individual nuclear spins are extremely difficult to isolate and control. Utilizing the electronic spin of a single NV center to detect and control surrounding nuclei is a promising approach to this challenge. Early work has demonstrated that NV centers can be used to sense strongly coupled proximal nuclear spins [12, 103, 104]. This approach has been used to create a few-qubit quantum register [105, 106], perform simple quantum algorithms [103, 107], implement single shot readout of both nuclear and electronic spins [100, 108], and demonstrate a multi-second quantum memory at room temperature [60].

In this chapter we show that the NV electronic spin can be used to isolate and probe the quantum dynamics of distant, weakly coupled individual Carbon-13 nuclear spins. Our approach relies on the same dynamical decoupling sequences utilized to sense the Brownian motion of a mechanical resonator in the previous chapter. We demonstrate that these

sequences can also enhance the sensitivity to individual nuclear spins while suppressing NV electronic spin decoherence [37, 77, 79, 109–112]. Crucially, this allows us to observe the coherent evolution of nuclear spins whose coupling to the NV is weaker than the limit imposed by the NV spin's inhomogenous dephasing rate, $1/T_2^*$. We demonstrate this capability by identifying single nuclear spins from amongst a bath of naturally abundant ^{13}C nuclear spins. The ability to isolate spins from within a bath is important for applications where surrounding nuclear spins cannot be avoided; moreover, it enables the use of these nuclear spins as a resource. In particular, our technique could be extended to harness weakly coupled nuclear spins in quantum registers [60, 100, 103, 106–108], investigate the spatial extent of the NV electronic wave function [113–116], or detect individual spins outside of the diamond lattice for single spin MRI applications [37, 38, 94, 101].

4.2 Key concepts of the experiment

The central idea of the work present in this chapter is depicted in Figure 4.1c, and can be understood in terms of the coherent evolution of a single ^{13}C nuclear spin interacting with the NV electronic spin sensor. Through their interaction, the magnitude and orientation of the local magnetic field experienced by the ^{13}C spin depends on the NV spin state. Consequently, when the NV spin is prepared in a superposition of its energy eigenstates, the ^{13}C spin undergoes conditional Larmor precession around two different axes. During this precession the electron and nuclear spin become entangled and disentangled [12]. However, if the NV-nuclear coupling is weak then the two precession axes are similar and the resulting entanglement is small. The key idea of this experiment is to increase the degree of entanglement, and thus the measurable signal, by applying periodic π-pulses, flipping the NV spin with a frequency matched to the precession of the ^{13}C spin. As shown schematically in Figure 4.1c, this constructively enhances the conditional evolution of the ^{13}C state, and thereby increases its entanglement with the NV spin.

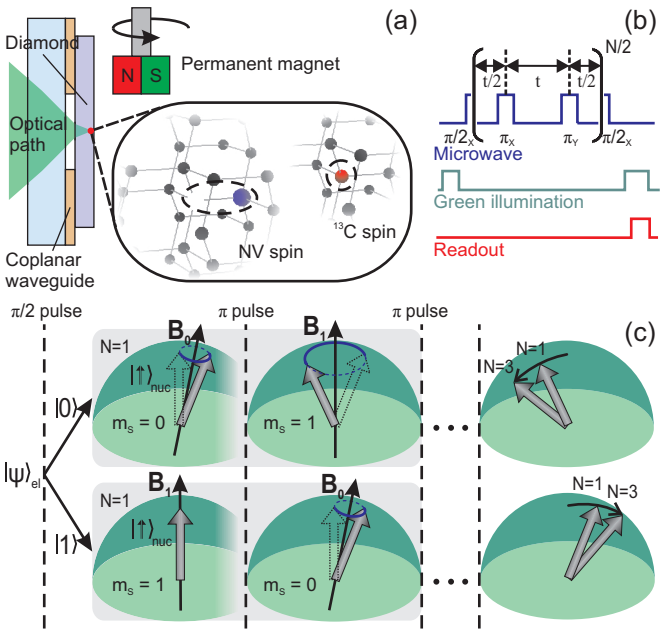

Figure 4.1: Central concepts of the experiment. (a) Schematic setup. We measure NV centers weakly coupled to ^{13}C nuclear spins. A dc magnetic field is applied using a movable permanent magnet. (b) Pulsed spin manipulation and readout. (c) Central concept. Conditional evolution of the ^{13}C on the Bloch sphere during NV spin manipulation for ^{13}C spin initially in state $|\uparrow\rangle$, where $|\uparrow\rangle, |\downarrow\rangle_{nuc}$ are defined as the eigenstates of the ^{13}C spin when the NV electron spin is in the state $m_s = 1$. Upper (lower) panel shows ^{13}C evolution with the NV spin is initially in state $|0\rangle$ ($|1\rangle$). Gray boxes show evolution during spin echo (single π-pulse). Additional π-pulses push the conditional nuclear spin evolution further apart, increasing its entanglement with the NV. For clarity a sequence with an odd number of π-pulses is shown; the result is qualitatively the same for the even numbered sequences used in this chapter, but is more difficult to visualize.

To describe the experimental sequence shown in Figure 4.1b, we consider the mutual interaction between a single NV electronic spin-1 and a single ^{13}C nuclear spin-$\frac{1}{2}$, which is governed by the Hamiltonian ($\hbar = 1$)

$$H = \Delta S_z^2 - \mu_e B_z S_z + (\mu_n \mathbf{B} + S_z \mathbf{A}) \cdot \mathbf{I}. \tag{4.1}$$

Here, $\mathbf{S}$ ($\mathbf{I}$) and μ_e (μ_n) are the electronic (nuclear) spin and magnetic moment respectively, $\mathbf{B}$ is the external magnetic field, and $\mathbf{A}$ is the hyperfine interaction. Due to the large

zero field splitting $\Delta/2\pi \simeq 2.87\,\mathrm{GHz}$, we have made the secular approximation conserving S_z. The nuclear spin evolves conditionally on the NV spin state according to $H_{\mathrm{nuc}}[m_s] = \frac{\omega_{m_s}}{2}\boldsymbol{\sigma}\cdot\mathbf{n}_{m_s}$, ($\boldsymbol{\sigma}$: Pauli spin matrices). Thus the nuclear spin precesses about an effective magnetic field axis $\mathbf{n}_{m_s} = (\mu_n\mathbf{B} + m_s\mathbf{A})/\omega_{m_s}$ with Larmor frequency $\omega_{m_s} = |\mu_n\mathbf{B} + m_s\mathbf{A}|$ when the NV spin is in state $|m_s\rangle$. We initialize the NV spin in a superposition of $|0\rangle$ and $|1\rangle$ and apply a periodic series of N π pulses spaced by evolution time t, during which $|0\rangle$ and $|1\rangle$ accumulate a relative phase. Converting the phase into a population difference, the normalized fluorescence signal at the end of the measurement of total length Nt is $p = (\mathcal{S}+1)/2$, where

$$\mathcal{S} = 1 - (\hat{\mathbf{n}}_0 \times \hat{\mathbf{n}}_1)^2 \sin^2\left(\tfrac{\omega_0 t}{2}\right)\sin^2\left(\tfrac{\omega_1 t}{2}\right)\frac{\sin^2(N\phi/2)}{\cos^2(\phi/2)} \tag{4.2}$$

and $\cos\phi = \cos\frac{\omega_0 t}{2}\cos\frac{\omega_1 t}{2} - \hat{\mathbf{n}}_0\cdot\hat{\mathbf{n}}_1\sin\frac{\omega_0 t}{2}\sin\frac{\omega_1 t}{2}$. This is the extension for arbitrary (even) N pulses of the well-known result for $N = 1$ corresponding to Hahn spin echo [12], and the derivation can be found in Appendix B.1. The factor of N multiplying the small angle ϕ is responsible for the enhanced signal that enables detection of weakly coupled nuclear spins.

4.3 Measurements

We study NVs implanted in a diamond sample with naturally abundant spin-$\frac{1}{2}$ ^{13}C nuclei (1.1% abundance). The NV electronic orbital ground state is a spin triplet which can be initialized in the $|m_s = 0\rangle$ state using green illumination, and read out via spin-dependent fluorescence [12]. The $|m_s = \pm 1\rangle$ degeneracy is lifted by a dc field applied using a permanent magnet. We coherently manipulate the NV spin using resonant microwaves delivered by a coplanar waveguide. The control pulse sequence used in this experiment is known as XY4-8 [77], and consists of N=8 π-pulses as shown in Figure 4.1b, phase alternated to mitigate microwave pulse errors.

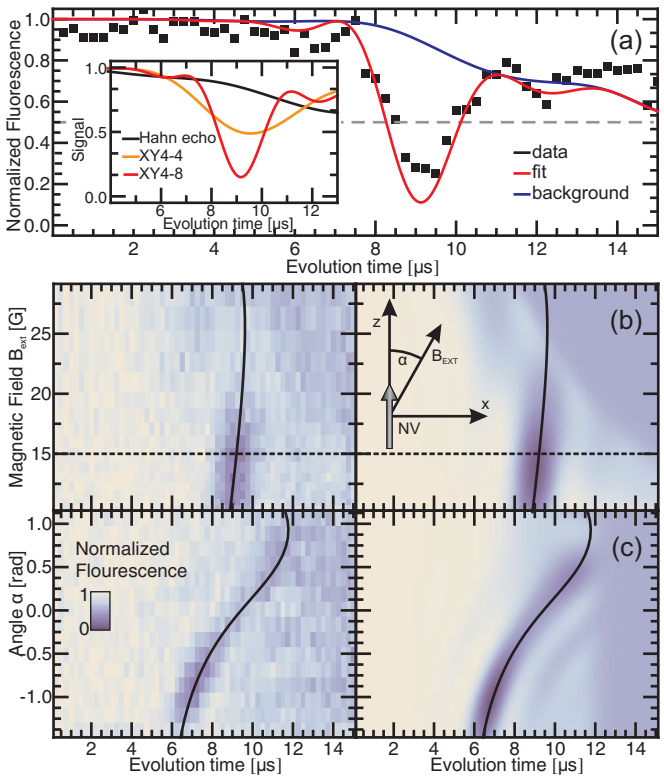

Figure 4.2: Coherent interaction of an NV center with a single ^{13}C. (a) The evolution time between π-pulses t is swept with a fixed magnetic field of 15 G, data (black) and fit (red). The blue line is the calculated response without the individual ^{13}C. The inset shows the calculated response to Hahn echo, XY4-4, and XY4-8. (b) The fluorescence is plotted as a function of t and magnetic field strength B, with magnetic field oriented along the NV $\hat{z}$ axis ($\alpha = 0$, as defined in the inset). The dashed line highlights the data shown in (a). (c) Fluorescence as a function of t and magnetic field orientation α, with B = 19 G. The black line displays the extracted dip position in both (b) and (c).

Detection of a single weakly coupled ^{13}C spin is shown in Figure 4.2a. The dip in the NV fluorescence signal at evolution time $t \approx 9$ μs results from the coherent interaction with the single ^{13}C spin and represents the signal. Importantly, this signal would go undetected using spin echo, as shown in the inset of Figure 4.2a. That the dip drops below a normalized fluorescence of 0.5 reflects the coherent nature of the interaction. By adding microwave control over the ^{13}C, this interaction could be exploited to perform a coherent rotation of the ^{13}C spin conditional on the state of the NV electron spin or vice versa. The overall

decay is a result of the Larmor precession of the surrounding bath of distant ^{13}C spins, which produces collapses and revivals in the NV coherence [12], with only the first collapse visible in Figure 4.2. The slight discrepancy between the data and the theory curve at $\sim$ 14 μs is a result of the random distribution of ^{13}C spins in the bath, which our model does not account for exactly (see Appendix B.2).

To confirm that the observed feature arises from a single ^{13}C, we plot the measured signal as a function of applied magnetic field strength (Figure 4.2b) and orientation (Figure 4.2c). We measure the NV response in both possible sets of magnetic sublevels ($|0\rangle \leftrightarrow |1\rangle$ and $|0\rangle \leftrightarrow |-1\rangle$, see Appendix B) and the entire data set is simultaneously fitted to Eq. (4.2). The only free parameters are the hyperfine vector $\mathbf{A}$, composed of three parameters defined relative to the NV axis and magnetic rotation axis, and two free parameters describing the strength and spectral width of the surrounding spin bath (see Appendix B.3). The calculated signal using the extracted fit parameters is shown in the right panels of Figure 4.2, and is in good agreement with the data. We obtain a robust, unique fit over a wide range of initial parameters. The fit gives a total coupling strength of $|\mathbf{A}|/2\pi \sim 125\,\mathrm{kHz}$, which is less than the bare dephasing rate of this NV, $1/T_2^* = 400\pm16$ kHz. T_2^* is measured using a Ramsey sequence (see Appendix B), and arises from the bath spin configuration varying from measurement to measurement. This demonstrates that we can simultaneously decouple the NV from the ^{13}C spin bath and still obtain a measurable signal from a target nuclear spin.

Figure 4.3 shows the measurement of the weakest coupled individual ^{13}C observed in this experiment. This single spin produces no discernible signal for the evolution times and magnetic field strengths shown in Figure 4.2 (measurement shown in Appendix B.5), because the weaker hyperfine coupling results in a dip that occurs after the first collapse induced by the bath and is therefore suppressed. In order to measure this weakly coupled spin at longer evolution times we increase the magnetic field, moving a bath-induced revival into the range

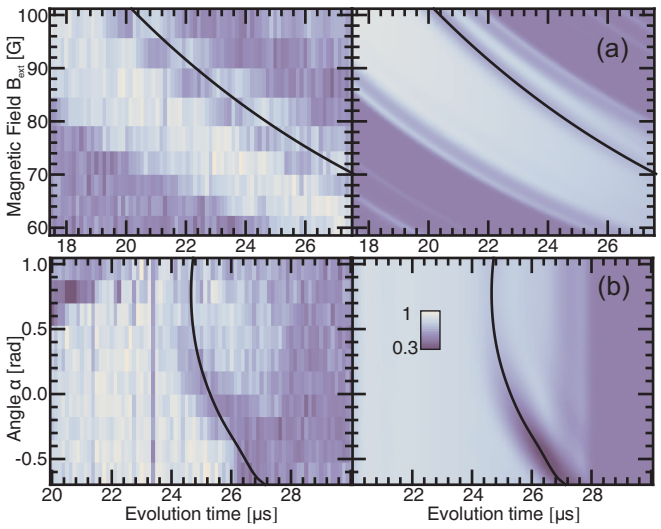

Figure 4.3: Detection of a distant ^{13}C with an XY4-8 sequence. As in Figure 4.2 the NV fluorescence is shown as a function of (a) magnetic field strength B with $\alpha = 0.26\,\text{rad}$, and (b) magnetic field orientation α, with $\text{B} = 80\,\text{G}$. The dip from the single ^{13}C is visible within a spin-bath revival centered at $2 \cdot 2\pi/\omega_0$.

of interest. We thereby observe a characteristic dip in the bath revival resulting from an individual nuclear spin. Again, this data is reproduced by a fit to our model; the extracted coupling strength is $|\mathbf{A}|/2\pi \sim 47\,\text{kHz}$, a factor of ~ 4.6 below the measured $1/T_2^* = 217 \pm 9$ kHz (see Appendix B.5).

Our technique also allows us to observe the impact of multiple ^{13}C spins coupled to a single NV. As the maximum mutual interaction strength of two ^{13}C spins on adjacent lattice sites is only 2 kHz [117], we can treat the ^{13}C spins as independent. Consequently, the signal given by Eq. (4.2) becomes a product of the individual contributions from each coupled spin, $\mathcal{S} = \Pi_j \mathcal{S}_j$ [12]. Figure 4.4 shows the impact of three ^{13}C spins. The double dip visible in the data results from the product of two overlapping dips from two ^{13}C spins with similar coupling strengths. This is emphasized in the inset of Figure 4.4c, where the calculated effect of each ^{13}C spins on $\mathcal{S}$ is displayed separately. The weakest coupled of the three ^{13}C spins has an extracted coupling strength of $|\mathbf{A}|/2\pi \sim 64\,\text{kHz}$, a factor of ~ 8

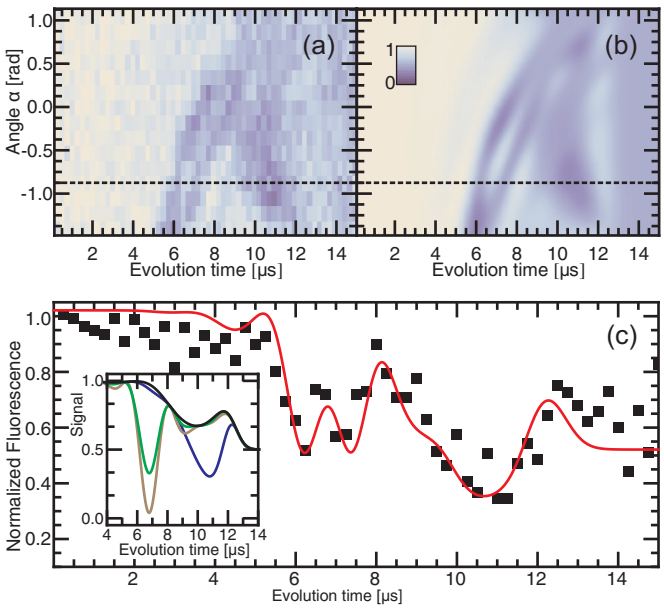

Figure 4.4: Simultaneous detection of three ^{13}C nuclei. (a) and (b) NV fluorescence is shown vs. evolution time t and magnetic field orientation α (data and fit), the applied field strength is 19 G. The fit assumes three ^{13}C spins and yields robust and unique individual coupling strengths, while fits assuming fewer ^{13}C spins could not reproduce the data. The NV response along the dashed line is shown in (c) black, red: data, fit. The traces in the inset display the calculated response of the NV interacting separately with each ^{13}C, and with the spin bath alone (black.)

below the measured $1/T_2^* = 560 \pm 60$ kHz (see Appendix B.5). By tuning the evolution time and magnetic field, the NV can be individually entangled with each of these ^{13}C spins (see Appendix B.5). This method could also be used to detect a larger number of individual spins, as long as their hyperfine couplings are within the detection limits imposed by the NV coherence time, as discussed in the following section.

4.4 Discussion

Assuming the NV-^{13}C couplings arise solely from a point-dipole interaction, the measured couplings translate into NV-^{13}C distances of $\sim$ 0.4-0.8 nm (see Appendix B), consistent with the range expected for a probabilistic distribution of naturally abundant ^{13}C. However, ab

initio calculations suggest that the electronic wavefunction is non-negligible at this length scale, and may lead to a significant contact term in the hyperfine interaction [113–116]. The coupling strengths measured here significantly exceed the accuracy of state of the art calculations [113, 114, 116], preventing us from explicitly including the calculated contact interaction. We therefore conclude that assuming a purely dipolar interaction likely provides a minimum distance estimate. By using our technique to acquire a much larger data set in the spirit of recent surveys of strongly coupled ^{13}C spins [115, 116], it should be possible to identify individual distant ^{13}C lattice sites and shed light on the the spatial distribution of the electronic wave function beyond the limits of current theory.

The hyperfine couplings $|\mathbf{A}|/2\pi$ extracted in this experiment exceed the decoherence rate $1/T_2$ obtained in a Hahn spin echo sequence, and in principle the ^{13}C spins could therefore be detected using only a single π-pulse (see Appendix B.4). However, this would require precise optimization of the magnetic field strength and orientation, which is not practical in a typical experiment. One advantage of extended pulse sequences is to relax these conditions and greatly simplify the identification of nuclear spins whose couplings to the NV are initially unknown. As a result, using the presented technique we were able to detect the closest ^{13}C for every NV investigated.

The use of dynamical decoupling sequences with multiple π-pulses has the added benefit of decoupling the NV spin from the surrounding environment, increasing its coherence time from T_2 to $T_2^{\text{eff}} = T_2 N^{2/3}$ and thereby potentially improving the sensitivity. Increasing the number of π-pulses for the same total evolution time requires higher magnetic fields to ensure that the sequence remains synchronized with the evolution of the target nuclear spin. In this limit $|\mu_n \mathbf{B}| \gg |\mathbf{A}|$, and a weakly coupled single ^{13}C has the same Larmor precession frequency as the surrounding nuclear spin bath and cannot be isolated. Therefore $|\mathbf{A}|/2\pi > 1/T_2$ is the limit for the detection of individual ^{13}C nuclear spins in a sample of natural isotopic abundance. However, for applications involving the detection of spins with

a different gyromagnetic ratio than the surrounding bath we find the sensitivity scales with number of π-pulses as $N^{4/3}$ (see Appendix B.4). As a result, our approach could potentially be used to detect individual spins inside or outside the diamond lattice up to the ultimate limit $|\mathbf{A}|/2\pi > 1/2T_1$, where $1/T_1$ is the NV spin relaxation rate. At room temperature $1/2T_1$ can be as low as $\sim$100 Hz [59, 75], corresponding to the dipolar coupling between an NV and a proton spin at a distance of $\sim$7-9 nm, which is of great interest for single spin MRI applications [94, 101, 102].

4.5 Conclusions and outlook

In conclusion, we used coherently controlled single NV electronic spins to detect distant nuclear spins. In particular, extended pulse sequences enabled the detection of ^{13}C nuclei with couplings far below the electronic spin bare dephasing rate. We also demonstrated that the simultaneous detection of several distant ^{13}C spins is possible, even within an environment consisting of a large number of spins with the same gyromagnetic ratio. Our technique allows for sensitive, coherent measurements of the nuclear spin environment of a single electronic spin; moreover, extensions of this approach could be used to exploit the nuclear spin environment as a resource to extend the size of controllable multi-spin quantum registers. Potential novel applications range from information storage to environment-assisted sensing and single spin MRI.

Chapter 5

Probing Johnson noise and ballistic transport in normal metals with a single NV spin

5.1 Introduction

Understanding electron transport, dissipation, and fluctuations at sub-micron length scales is critical for the continued miniaturization of electronic [118, 119] and optical devices [120–122], as well as atom and ion traps [50, 123–126], and for the electrical control of solid-state quantum circuits [127]. While it is well-known that electronic transport in small samples defies the conventional wisdom associated with macroscopic devices, resistance-free transport is difficult to observe directly. Most of the measurements demonstrating these effects make use of ohmic contacts attached to sub-micron scale samples and observe quantized but finite resistance corresponding to the voltage drop at the contact of such a system with a macroscopic conductor [128, 129]. Techniques for non-invasive probing of electron transport are now actively explored [130, 131] because they can provide insights into electronic dynamics at small length scales. Our approach makes use of the electromagnetic fluctuations associated with Johnson noise close to a conducting surface, which can be directly linked to the dielectric function at similar length scales, providing a non-invasive probe of electronic transport inside the metal. Measurements of these fluctuations at micron length scales utilizing cold, trapped atoms showed excellent agreement with predictions

based on diffusive electron motion [50, 124, 125], while millimeter length scale measurements utilizing superconducting quantum interference devices (SQUIDs) have been demonstrated for use as an accurate, contact free thermometer [132].

Our approach makes use of the electronic spin associated with nitrogen-vacancy defect centers in diamond (NVs) to study the spectral, spatial, and temperature dependence of Johnson noise emanating from conductors. The magnetic Johnson noise results in a reduction of the spin lifetime of individual NV electronic spins, thereby allowing us to probe the intrinsic properties of the conductor non-invasively over a wide range of parameters. Individual, optically resolvable, NV centers are implanted ∼15 nm below the surface of a ∼30-μm thick diamond sample. A silver film is then deposited on or positioned on the diamond surface (Figure 5.1a). The spin sublevels $|m_s = 0\rangle$ and $|m_s = \pm 1\rangle$ of the NV electronic ground state exhibit a zero-field splitting of $\Delta = 2\pi \times 2.88$ GHz [12, 38, 63, 133]. The relaxation rates between the $|0\rangle$ and $|\pm 1\rangle$ states provide a sensitive probe of the magnetic field noise at the transition frequencies $\omega_\pm = \Delta \pm 2g\mu_B B_{||}/\hbar$, where $B_{||}$ is the magnetic field along the NV axis [134, 135] (Figure 5.1b).

5.2 Key concept

The impact of Johnson noise emanating from a polycrystalline silver film deposited on the diamond surface (Figure 5.1c) is evident when comparing the relaxation of a single NV spin below the silver (red circles) to the relaxation of the same NV prior to film deposition and after removal of the silver (open blue squares and triangles, respectively). At room temperature and in the absence of external noise, the spin lifetime is limited by phonon-induced relaxation to $T_1^{\mathrm{ph}} \approx 4$ ms. With the silver nearby, the lifetime of the $|m_s = 0\rangle$ state is reduced to $T_1 = 165$ μs, which we attribute to magnetic Johnson noise emanating from the film. To verify that the enhanced relaxation is due to magnetic noise, we compare the lifetime of the $|0\rangle$ state, which has magnetic dipole allowed transitions to both of the $|\pm 1\rangle$

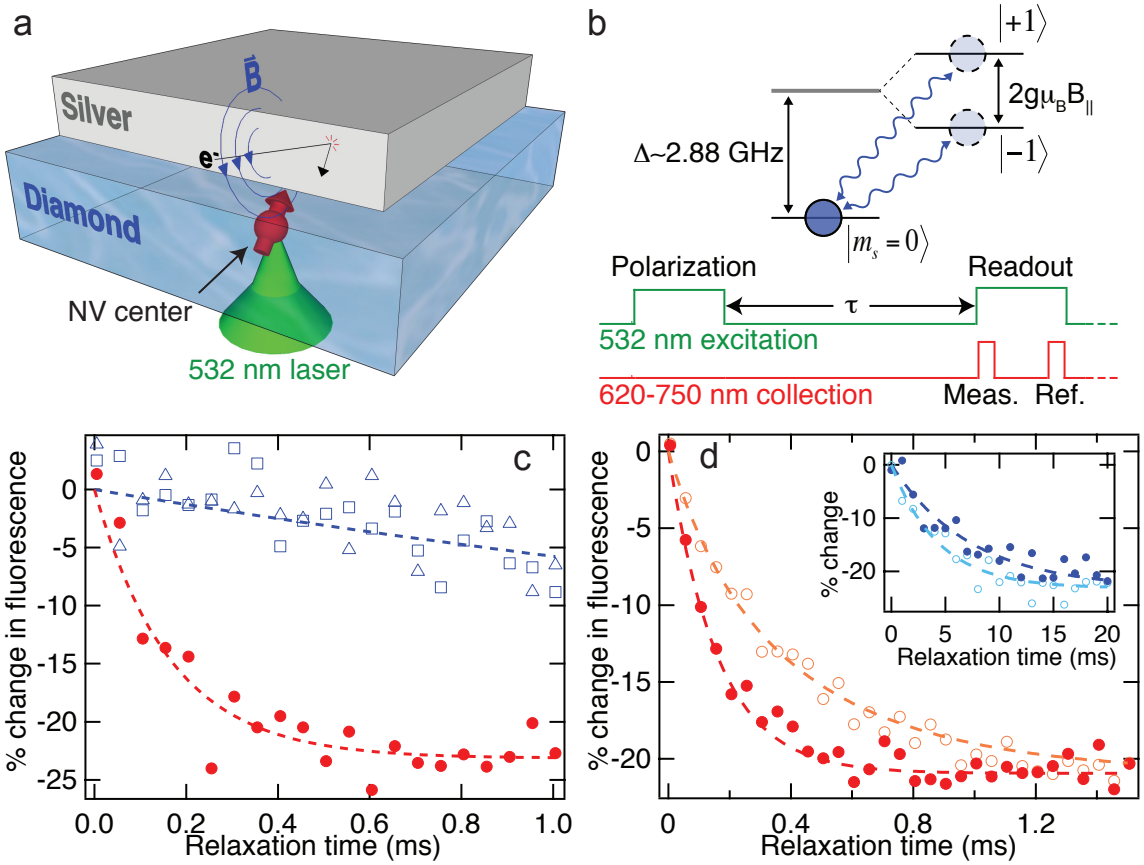

Figure 5.1: **Probing Johnson noise with single spin qubits.**(a) The thermally induced motion of electrons in silver generates fluctuating magnetic fields ($\vec{\mathbf{B}}$), which are detected using the spin of a single NV. The NV is polarized and read out through the back side of the diamond. (b) The NV spin is polarized into the $|m_s = 0\rangle$ state using a green laser pulse. Spin relaxation into the $|m_s = \pm 1\rangle$ states is induced by magnetic field noise at ∼2.88 GHz. After wait time τ the population left in $|0\rangle$ is read out by spin-dependent fluorescence. All measurements shown were performed at low magnetic fields ($\Delta \gg g\mu_B B_{||}/\hbar$). (c) Spin relaxation data for the same single shallow implant NV before silver deposition (open blue squares), with silver deposited (red circles), and after the silver has been removed (open blue triangles). (d) Spin relaxation for a single NV close to a silver film prepared in the $|m_s = 0\rangle$ state (red circles), and in the $|m_s = -1\rangle$ state (open orange circles). (Inset) Spin relaxation for a single native NV in bulk diamond in the $|m_s = 0\rangle$ state (blue circles), and in the $|m_s = -1\rangle$ state (open light blue circles).

states, to that of the $|-1\rangle$ state, which can only decay directly to the $|0\rangle$ state (Figure 5.1d). As expected for relaxation induced by magnetic noise, the $|-1\rangle$ state has approximately twice the lifetime of the $|0\rangle$ state (see Appendix C.4). This is in contrast to the observed lifetimes when limited by phonon-induced relaxation (Inset, Figure 5.1d), where the $|0\rangle$ and $|\pm 1\rangle$ states have almost identical lifetimes [136]. In what follows we define T_1 as the lifetime of the $|m_s = 0\rangle$ state.

5.3 Distance dependence of NV spin relaxation next to polycrystalline silver

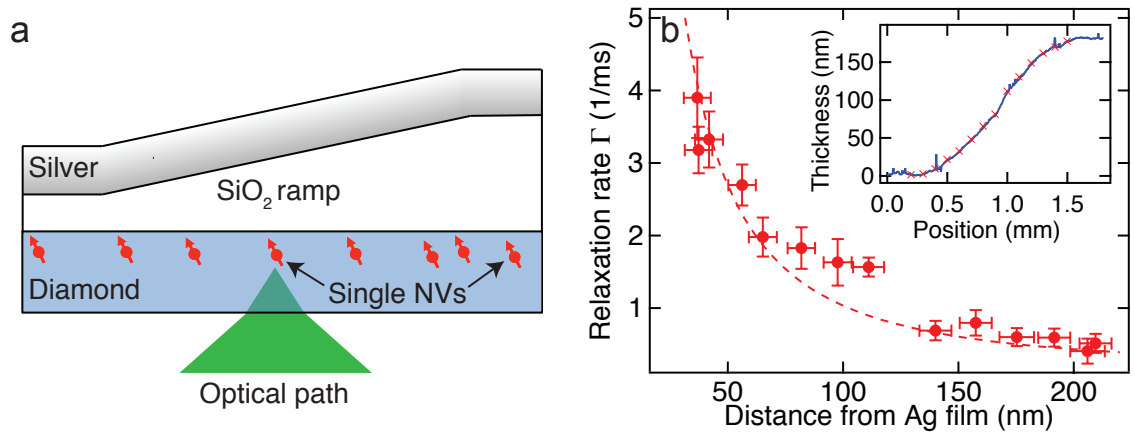

Figure 5.2: **Distance dependence of NV relaxation close to silver.** (a) A gradual SiO_2 ramp (slope of $\sim$.2 nm/micron) is grown on the diamond surface, followed by a 60 nm silver (Ag) film. (b) The NV relaxation rate is measured as a function of position along the ramp, which is then converted to distance to the film. At each point 5-10 NV centers are measured, and the minimum rate measured is plotted (red circles). The red dashed line shows the expected relaxation rate with no free parameters after accounting for the finite silver film thickness. (Inset) Thickness of the ramp as a function of lateral position along the diamond sample (blue curve). The red crosses correspond to the positions along the sample where the measurements were taken.

To test the scaling of Johnson noise with distance (d) to the metal, we deposit a layer of SiO_2 on the diamond surface with a gradually increasing thickness (Figure 5.2a).

We characterize the thickness of the SiO_2 layer as a function of position on the sample (Inset, Figure 5.2b), and deposit a 60-nm polycrystalline silver film on top of the SiO_2. The conductivity of the silver film is measured to be 2.9×10^7 S/m at room temperature. By measuring the relaxation rates $\Gamma = 1/T_1$ of individual NVs at different positions along the SiO_2 ramp we extract the distance dependence of the noise (Figure 5.2b), with the uncertainty in the distance dominated by the variation in the implanted depth of the NVs (taken to be 15±10 nm). To ensure that the measured rates are Johnson-noise limited, we measure the spin relaxation of 5-10 randomly selected NVs per location along the ramp, and plot the minimum observed rate at each location (see Appendix C.5.1). As expected [50, 124, 125], the magnitude of the noise increases as the NVs approach the silver surface.

5.4 Temperature dependence of NV spin relaxation next to polycrystalline silver

To investigate the dependence of the noise on temperature and conductivity, we deposit a 100-nm polycrystalline silver film on a diamond sample and measure the T_1 of a single NV beneath the silver over a range of temperatures (∼10-295 K). The measured relaxation rate for a single NV near the silver increases with temperature (red circles in Figure 5.3a), as expected for thermal noise, but the scaling is clearly non-linear. This can be understood by recognizing that the conductivity of the silver film is also a function of temperature, and that the magnitude of the thermal currents in the silver depend on the conductivity. To account for this effect, a four point resistance measurement of the silver film is performed to determine the temperature dependence of the bulk conductivity of the silver film (Figure 5.3b).

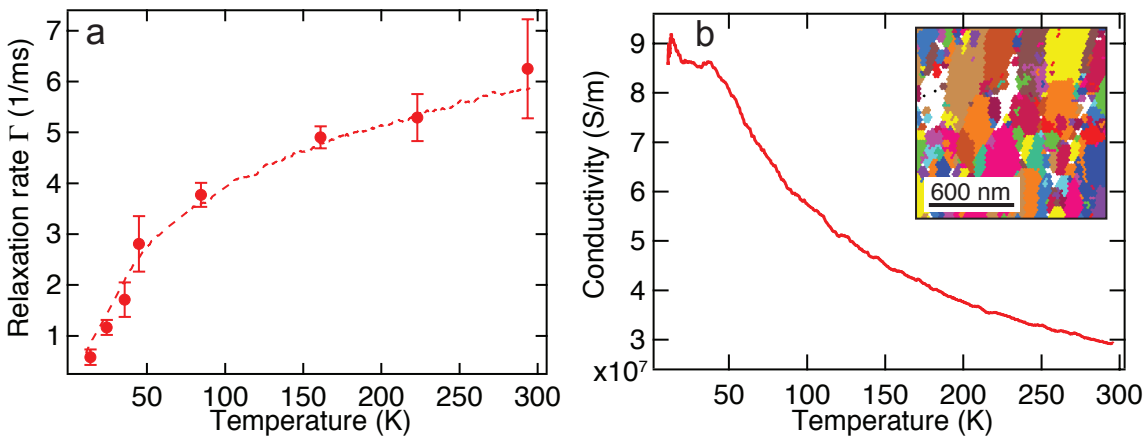

Figure 5.3: **Temperature dependence of NV relaxation close to polycrystalline silver.** (a) The measured relaxation rate T_1 of a single NV spin under a polycrystalline silver film as a function of temperature (red data points). The conductivity of the silver film as a function of temperature shown in (b) is included in a fit to Eq. 2, with the distance to the film as the single free parameter (red dashed line). The extracted distance is 31±1 nm. (b) The conductivity of the 100 nm thick polycrystalline silver film deposited on the diamond surface is measured as a function of temperature. (Inset) Grain boundaries within the polycrystalline silver film, imaged using electron backscatter diffraction (EBSD). The average grain diameter is 140 nm, with a standard deviation of 80 nm.

5.5 Conventional theory of magnetic Johnson noise

To analyze the dependance of the NV spin relaxation rate on distance, temperature, and conductivity, the model of ref. [123] is used, in which an electronic spin-1/2 qubit with Larmor frequency ω_L is positioned at a distance d from the surface of a metal. For silver at room temperature the skin depth at ω_L is $\delta \approx 1$ μm; consequently when $d <$100 nm we are in the "quasi-static" limit $d \ll \delta$. The thermal limit $k_B T \gg \hbar\omega_L$ is valid for all temperatures in this work. In this regime the magnetic noise spectral density perpendicular to the silver surface is given by

$$S_B^z = \frac{\mu_o^2}{16\pi}\frac{k_B T \sigma}{d}, \tag{5.1}$$

where σ is the temperature-dependent conductivity of the metal as defined by the Drude model. This scaling can be intuitively understood by considering the magnetic field gen-

erated by a single thermal electron in the metal at the NV position, $B_o = \frac{\mu_o e v_{th}}{4\pi d^2}$, where the thermal velocity $v_{th} \propto \sqrt{k_B T/m_e}$, m_e is the effective mass of electrons in silver and e is the electron charge. In the limit $d \ll \delta$ screening can be safely ignored, and the NV experiences the magnetic field spectrum arising from N independent electrons in a volume V, $S_B \propto Vn\langle B_o\rangle^2\tau_c$, where n is the electron density and τ_c is the correlation time of the noise, given by the average time between electron scattering events, $\tau_c = l/v_F$, where l is the electron mean free path and v_F is the Fermi velocity. Recognizing that the NV is sensitive to the motion of electrons within a sensing volume $V \propto d^3$, we arrive at the scaling given by Eq. 5.1, with $\sigma = \frac{ne^2\tau_c}{m_e}$. Applying Fermi's golden rule and accounting for the orientation and spin-1 of the NV yields the relaxation rate for the $|m_s = 0\rangle$ state

$$\Gamma = \frac{1}{T_1} = \frac{3g^2\mu_B^2}{2\hbar^2} S_B^z \left(1 + \frac{1}{2}\sin^2(\theta)\right), \tag{5.2}$$

where $g \approx 2$ is the electron g-factor, μ_B is the Bohr magneton, and $\theta \approx 54.7^\circ$ is the angle of the NV dipole relative to the surface normal vector. In Figure 5.2b the inverse scaling with distance d predicted by Eq. 5.1 is clearly evident for NVs very close to the silver. At distances comparable to the silver film thickness Eq. 5.1 is no longer valid, but we recover excellent agreement with the no-free-parameters prediction of Eq. 5.2 by including a correction for the thickness of the silver film (red dashed line in Figure 5.2b), which is measured independently. The measured relaxation rates as a function of temperature are also in excellent agreement with the predictions of Eq. 5.2 (red dashed line in Figure 5.3a), while the extracted distance of 31±1 nm is consistent with the expected depth (see Appendix C).

5.6 Temperature dependence of NV spin relaxation next to single crystal silver

Remarkably, very different results are obtained when we replace the polycrystalline film with single-crystal silver. For this experiment, a 1.5-μm thick single-crystal silver film grown by sputtering onto silicon [137, 138] is placed in contact with the diamond surface (see Appendix C.2.5). The measured conductivity of the single-crystal silver exhibits a much stronger temperature dependance (blue line in Figure 5.4a) as compared to that of the 100-nm thick polycrystalline film. Figure 5.4b presents the measured relaxation rate as a function of temperature for an NV in a region in direct contact with the single-crystal silver (blue squares). The dashed blue line corresponds to the temperature dependent rate predicted by Eq. 5.2, which strongly disagrees with the experimental results. Specifically, because the measured silver conductivity increases faster than the temperature decreases in the range from room temperature down to 40 K, Eq. 5.2 predicts the relaxation rate should increase as the temperature drops, peaking at 40 K and then dropping linearly with temperature once the conductivity saturates. Instead, the T_1 of the NV consistently increases as the temperature drops, implying that at lower temperatures the silver produces considerably less noise than expected from Eq. 5.2. We observe similar deviation from the prediction of Eq. 5.2 for all 23 NVs measured in the vicinity of the single-crystal silver (see Appendix C.5.2).

To analyze these observations, we note that the conventional theoretical approach [123] resulting in Eq. 5.2 treats the motion of the electrons in the metal as entirely diffusive, using Ohm's law, $\mathbf{J}(\mathbf{r}, t) = \sigma\mathbf{E}(\mathbf{r}, t)$, to associate the bulk conductivity of the metal with the magnitude of the thermal currents. While accurately describing the observed relaxation rates next to the polycrystalline material, where the resistivity of the film is dominated by electron scattering off of grain boundaries (Inset, Figure 5.3b), this assumption is invalid in the single-crystal silver film experiments, particularly at low temperatures. Here, the measured

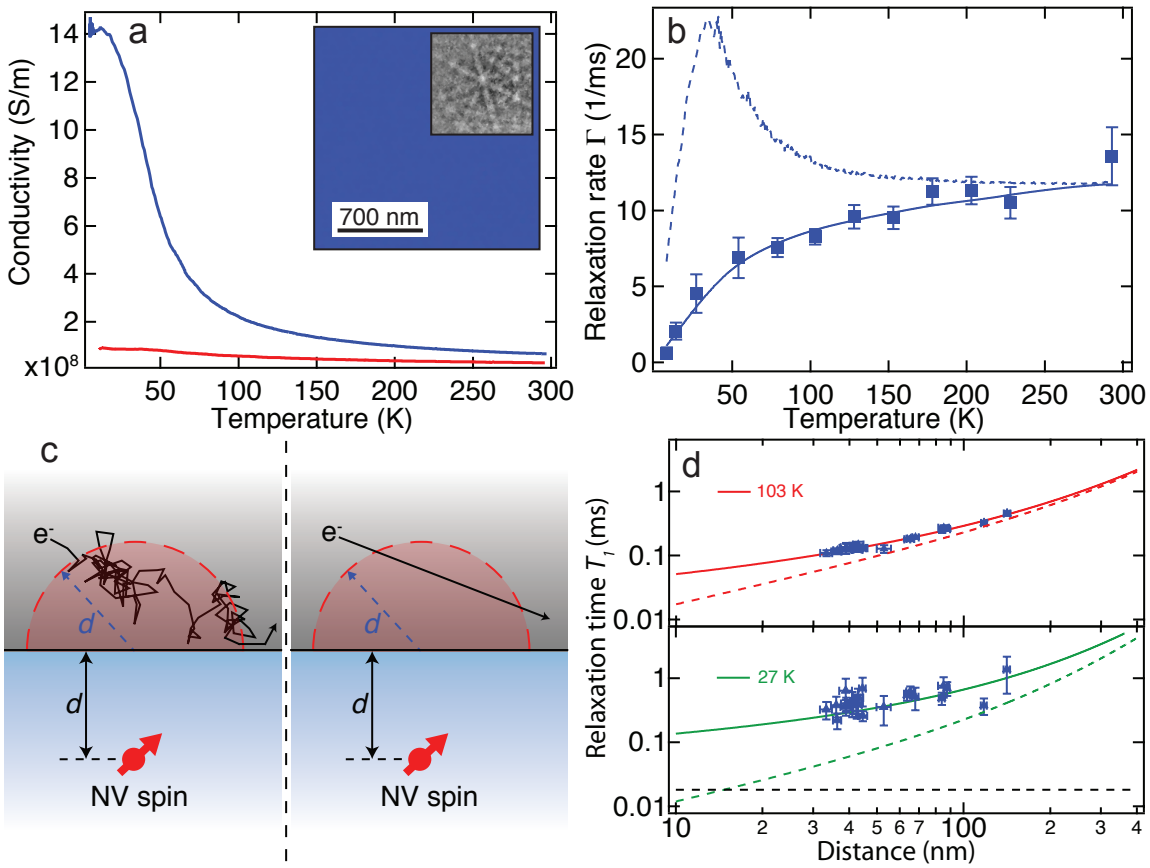

Figure 5.4: **Temperature dependence of NV relaxation close to single-crystal silver.** (a) Measured conductivity of single-crystal (blue curve) and polycrystalline (red curve, same as Figure 5.3b) silver as a function of temperature. (Inset) Electron backscatter diffraction image of the single-crystal silver film showing no grain boundaries, and the observed diffraction pattern. (b) Relaxation of a single NV spin under single-crystal silver as a function of temperature (blue squares). Eq. 2 is fit to the data from 200-295 K (blue dashed line). A non-local model (see Appendix C.3) is fit to the data (blue solid line), the extracted distance between the NV and the silver surface is 36±1 nm. (c) Cartoon illustrating the relevant limits, where the noise is dominated by diffusive electron motion (left, $l \ll d$), and ballistic motion (right, $l \gg d$). (d) The same data as (b) was taken for 23 NVs at varying distances from the film. The T_1 of each NV at 103 K (top) and 27 K (bottom) is plotted against the extracted depth (blue triangles). The non-local model (solid colored lines) saturates at a finite lifetime determined by Eq. 3 (bottom, dashed black line), while the local model does not (dashed colored lines).

conductivity of the single-crystal film indicate that the mean free path l is greater than one micron, significantly exceeding the sensing region determined by the NV-metal separation, and thus the ballistic motion of the electrons must be accounted for. Qualitatively, the correlation time of the magnetic noise in this regime is determined by the ballistic time of flight of electrons through the relevant interaction region $\tau_c \sim d/v_F$ (Figure 5.4c). This results in a saturation of the noise spectral density and the spin relaxation rate Γ as either the NV approaches the silver surface or as the mean free path becomes longer at lower temperatures (see Appendix C.3), with the ultimate limit to the noise spectrum given by:

$$S_B^z \sim \frac{2\mu_o^2 k_B T}{\pi} \frac{ne^2}{m_e v_F}. \tag{5.3}$$

This regime of magnetic Johnson noise was recently analyzed theoretically [127] using the Lindhard form non-local dielectric function for the metal modified for finite electron scattering times [139, 140] (see Appendix C.3). Comparison of this model (solid line in Figure 5.4b) to the data, with distance again as the only free parameter, yields excellent agreement for all 23 measured NVs (see Appendix C.5.2). Figure 5.4d shows the measured T_1 times at 103 K and 27 K for each NV as a function of extracted distance (blue triangles). Of the 23 NVs measured, 15 are in a region of the diamond sample in direct contact with the silver (see Appendix C.5.2). Excellent agreement between the non-local model (solid lines) and the data is observed for all 23 NVs at all 12 measured temperatures. Apparent in Figure 5.4d is the saturation of the relaxation rate as the NV approaches the silver surface, and as the mean free path becomes longer at lower temperatures (dashed black line), as predicted by Eq. 3.

5.7 Conclusions

While ballistic electron motion in nanoscale structures has previously been studied and utilized [128, 129], our approach allows for non-invasive probing of this and related phenomena, and provides the possibility for studying mesoscopic physics in macroscopic samples. The combination of sensitivity and spatial resolution demonstrated here enables direct probing of current fluctuations in the proximity of individual impurities, with potential applications such as imaging of Kondo states and probing of novel two-dimensional materials [141], where our technique may allow for the spatially resolved probing of edge states [128]. Likewise, it could enable investigation of the origin of $1/f$ flux noise by probing magnetic fluctuations near superconducting Josephson circuits [142, 143]. Finally, as Johnson noise presents an important limitation to the control of classical and quantum mechanical devices at small length scales [50, 123–126], the present results demonstrate that this limitation can be circumvented by operating below the length scale determined by the electron mean free path.

Chapter 6

Conclusion and outlook

6.1 Summary and outlook for Chapter 3

In Chapter 3, we presented experimental results demonstrating the detection of the driven and thermal motion of a mechanical resonator using a single NV center. While the motion detected in that experiment was entirely classical, we also found that detection of the resonator motion at the single phonon level is, in principle, achievable by combining parameters that have already been separately realized in experiment. In particular, the necessary condition for the detection of zero point motion was found to be $C = \lambda^2 \hbar Q \tilde{T}_2/(k_B T) > 1$, where λ is the Zeeman shift from a single phonon in the resonator, Q is the quality factor of the resonator, $\tilde{T}_2$ is the coherence time of the NV with a dynamical decoupling sequence applied, and T is the temperature of the environment. Furthermore, this condition, known as the "strong cooperativity" condition in the field of cavity QED, is identical to the requirement for mechanical transduction of spin-spin interactions [95], making this regime highly desirable. As a result, building upon the work presented in Chapter 3, we have continued to pursue the goal of entering the strong cooperativity regime between a single NV spin and mechanical resonator.

In order to increase the cooperativity parameter C, we have designed and fabricated our own magnetized, low mass, high quality factor mechanical resonators out of pre-stressed

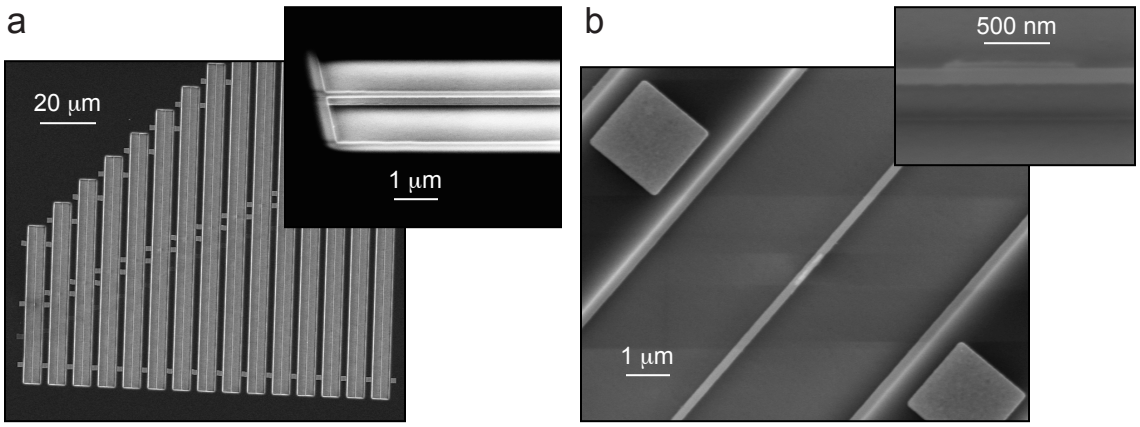

Figure 6.1: Nano-fabricated resonators. (a) Scanning electron microscope (SEM) image of an array of nano-fabricated, doubly-clamped, suspended SiN mechanical resonators of varying length with evaporated Ni magnets at the center of each resonator. Evaporated gold spacer squares are visible on either side of the top, bottom, and center of each resonator. (Inset) Zoomed in SEM image of a single suspended resonator, imaged at a 45° angle. The resonator is ∼150 nm thick, and is suspended ∼ 400 nm above the silicon substrate. The shadow of the resonator is also visible. (b) Zoomed in SEM of a single suspend resonator, with the deposited Ni magnet in the center of the image. The magnet is ∼100 nm wide, 1 micron long, and 30 nm thick. (Inset) The same resonator and magnet imaged at an angle, with the resonator suspended above the substrate.

sillicon-nitride (SiN) as shown in Figure 6.1. We have measured quality factors exceeding 2×10^5, and have successfully deposited nickel (Ni) magnets at the antinode of the resonators' fundamental mode, which were verified to be single domain prior to resonator release. To reduce the phonon dissipation rate by decreasing the temperature of the surrounding environment, we have constructed a new low-temperature setup in a closed-cycle Montana Instruments cryostat, with an integrated confocal microscope that enables the manipulation and readout of single NV spins at ∼ 4 K. This setup was used to take the temperature dependent data presented in Chapter 5. The outstanding experimental hurdles to achieving $C > 1$ are the deterministic positioning of the fabricated beams tens of nanometers from shallow NV centers at low temperature, and the need for strong magnetic field gradients, for which the evaporated Ni magnets may prove to be inadequate, although this has not

yet been determined. Both of these hurdles appear surmountable in the near future. In addition, we have expanded the theory presented in Chapter 3, considering in detail the sensitivity limits of coherent spin-based detection of mechanical motion, including the effects of measurement back-action [144].

Another promising development subsequent to the work presented in Chapter 3 has been the fabrication, by several different groups, of high quality factor mechanical resonators in single crystal diamond [145–147]. opening the door to bulk NVs with long coherence times inside high-Q mechanical resonators. While much of the theoretical and experimental work with these systems has so far focused on direct strain mediated coupling between the NV spin and the motion of the diamond resonator [44, 71, 148, 149] another promising path would be to use magnetic coupling by positioning an NV in a diamond resonator next to a nano-fabricated structure with large magnetic field gradients [93, 101], potentially enabling stronger coupling than is possible with our current SiN resonators.

6.2 Summary and outlook for Chapter 4

In Chapter 4, we demonstrated the detection of single weakly coupled nuclear spins with the electronic spins of single NV centers. We presented a new technique utilizing dynamical decoupling sequences that enabled us to entangle the NV electronic spin with individual ^{13}C spins from the surrounding nuclear spin bath. The hyperfine coupling rates to these spins were significantly slower than the inhomogenous NV spin dephasing rates, making these spins difficult to detect using previously established techniques [12, 60, 115, 116]. We demonstrated the detection of up to three ^{13}C spins coupled to a single NV, and were able to detect the nearest neighbor ^{13}C spin of every NV investigated.

The nuclear spin detection technique demonstrated in Chapter 4 dramatically increases the potential size of controllable multi-spin quantum registers based on NV centers. In fact, in parallel to our work, the same technique was used at high magnetic fields to detect

up to six ^{13}C spins coupled to a single NV [150], and to detect a single ^{13}C spin $\sim$3 nanometers away in isotopically purified diamond [151]. More recently, it was demonstrated that this technique, in combination with single nuclear spin operations, is sufficient for universal quantum control of the nuclear spins, and a three qubit error correction protocol was implemented within a single NV register [136]. Furthermore, our technique has since been utilized to study nuclear spin bath dynamics [152], and may ultimately enable the identification and control of single nuclear spins from within an external spin bath in NV-based NMR experiments [153–155].

6.3 Summary and outlook for Chapter 5

In Chapter 5, we utilized single NV centers to probe magnetic Johnson noise in proximity to conductive silver films. Using induced NV spin relaxation as of a probe of the spectral density of magnetic noise at the transition frequency, we investigated the spatial, spectral, and temperature dependent properties of Johnson noise at a length scale of tens of nanometers, a regime that has been out of reach with previously established techniques [50, 124, 125]. We found that the observed spectral density and scaling of the noise next to poly-crystalline silver films was in excellent agreement with the conventional theory for magnetic Johnson noise based on the Drude model of conductivity [123]. However, we observed a dramatic suppression of the noise close to single-crystal silver at low temperatures, which we attribute to a breakdown of Ohm's law and the Drude model arising from the ballistic motion of electrons in the metal. We found that the observed behavior was in excellent agreement with a generalized model for Johnson noise based on a non-local dielectric function that accounts for the ballistic electron motion [127].

There are a number of extensions and future directions to the work presented in Chapter 5. One exciting prospect is the study of magnetic Johnson noise in more complex geometries, for example near an edge or corner of a nano-fabricated structure, or the angu-

lar dependence and polarization of the magnetic noise using different NV orientations and spin states. Another potential application is the study of field noise close to conducting and superconducting surfaces in the d.c. to MHz frequency range, where a considerable amount of excess noise has been observed in ion traps [126] and superconducting qubits and SQUIDs [142, 143, 156]. Sensitivity at low frequencies can be achieved using the same dynamical decoupling sequences presented in Chapters 3 and 4, while the high spatial resolution of single NV magnetometry could provide new insights into the microscopic nature of the noise.

Beyond the study of field noise close to surfaces, the measurements presented in Chapter 5 demonstrate a new, non-invasive probe of electron transport in a bulk material, with a number of promising directions for future investigation. In particular, the high spatial resolution afforded by sensing with single NV centers could further the study of transport in novel materials such as graphene [141, 157] and transition metal dichalcogenides [158], as well as the investigation of mesoscopic phenomena associated with individual impurities, such as Freidel oscillations and Kondo clouds [140]. One intriguing possibility is the use of multiple, spatially separated NV centers to examine the spatial correlations and coherence lengths of these phenomena.

6.4 Final conclusions and outlook

The solid-state nature of the NV center results in an inherent sensitivity to the surrounding environment, in particular to nearby nuclear spins, defects, and surfaces, which at first may appear to be detrimental; as a result NVs are far more heterogenous and have shorter coherence times and broader optical line widths than atomic systems. However, this sensitivity also offers a number of unique opportunities. As demonstrated in Chapter 3, in which we coupled the spin of an NV to the motion of a macroscopic mechanical resonator, the sensitivity to nearby surfaces and external noise sources can be used to engineer coherent

coupling with other systems of interest for the creation of novel hybrid quantum systems. In Chapter 4, we showed that the NV electron spin's sensitivity to the surrounding nuclear spin bath can be harnessed as a resource for long-lived quantum registers, or to gain insight into many-body spin dynamics. In Chapter 5, we showed how the NV spin's sensitivity to magnetic field noise emanating from a nearby metal surface can be used as a noninvasive probe of electron transport inside the metal.

Furthermore, the work presented in this thesis is only the beginning. All three of the experiments have promising future extensions and applications. The results in Chapter 3 represents the first step towards the creation of a mechanical spin transducer, suitable for engineering long range spin-spin couplings, which is presently being pursued by a number of groups around the world. The single nuclear spin sensing technique presented in Chapter 4 is now routinely applied to the detection and control of external spins outside the diamond, which may enable the determination of the structure of single proteins. The sensitivity of the NV to electron transport demonstrated in Chapter 5 could be applied to the study of more complex condensed matter physics. It is my hope that this thesis constitutes a small but significant contribution to the rich, exciting, and rapidly expanding field of research with solid state spins, and in particular with the NV center in diamond.

Appendix A

Methods and analysis for the experiments presented in Chapter 3

A.1 Methods

A.1.1 Apparatus

We use a home-built AFM integrated with a confocal microscope to address and readout single NV defect centers implanted ∼5 nm below the surface of a bulk diamond sample (Element 6). A green (∼1 mW at 532 nm) excitation beam is used to polarize the target NV in the $m_s = |0\rangle$ state. Spin state detection is performed by collecting fluorescence emitted into the phonon-sideband (∼620-750 nm) using a single photon counting avalanche photon detector (APD, Perkins-Elmer). The non-spin preserving transitions from the excited state that result in polarization of the NV during excitation also cause spin-dependent fluorescence rates. Radio-frequency magnetic fields tuned to the $|0\rangle \rightarrow |+1\rangle$ transition manipulate the NV spin state. They are delivered via a co-planar waveguide patterned onto a glass coverslip on which the sample is mounted. An external d.c. magnetic field aligned with the NV axis is generated via a permanent rare-earth magnet placed ∼2 cm from the sample, which splits the degenerate $m_s = |\pm 1\rangle$ states. The magnet is moved with a motorized stage to tune the magnitude of the d.c. field.

The AFM probe consists of a magnetic force microscopy (MFM) cantilever of dimen-

sions $(l, w, t) \approx (240, 30, 2.7)\mu m$, with a resonance frequency of $\omega_r \approx 2\pi \times 80$ kHz (Asylum AFM.) The pyramidal tip is coated with a 100 nm thick layer of CoCr and has a magnetic moment specified at $\sim 3 \times 10^{-16}$ J/T. The cantilever is mounted on a piezo stack (attocube) that allows for both fine and coarse positioning along all three spatial axes. The cantilever is driven at its resonance frequency using an excitation piezo epoxied to the cantilever mount. The tip is maintained at a fixed height above the diamond surface by interferometrically measuring the cantilever's motional amplitude using an infrared (1550 nm) laser. Measurements were performed with several cantilevers and NV centers, all with similar parameters.

A.1.2 Positioning of the tip

Our setup incorporates a scanning galvometer (Cambridge Technologies) to scan our confocal spot across the diamond sample. Using filters we collect either the NV fluorescence or the reflected green light. In order to detect the lateral tip position, we take a reflection image by scanning our confocal spot. When the tip is close to the surface (on the order of one wavelength), it shows up in the reflection image, as shown in Figure B.10. This image is then compared to a reference and a correlation of the two images is performed to determine their relative spatial offset. Feeding this information to our piezo positioning system we are able to set or stabilize the tip position to an accuracy of $\sim$10 nm. During a single measurement this procedure is repeated frequently, typically every 300s.

To calibrate the conversion from galvo voltage into spatial units, we take an image of a reference structure. The uncertainties accumulated in the tip positioning are estimated as follows. First, we consider possible distortions in the reference structure and uncertainties in the extraction of its spatial dimensions, and conservatively assume a systematic error of 5%. Second, we repeat the positioning every 300s and detect an rms deviation of approx. 20 nm between subsequent images, consisting of drifts in between measurements and the

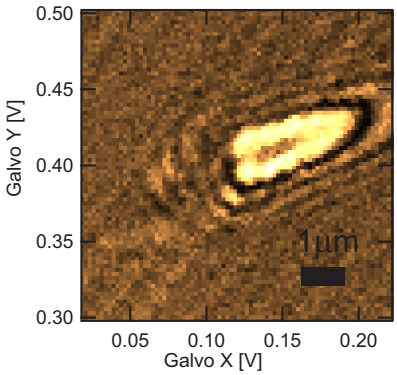

Figure A.1: Spatial scan of the sample in reflection, showing the magnetic tip.

uncertainty of the measurement method.

A.2 Measurement of the magnetic gradient

To measure the magnetic gradient of the tip along the NV-axis we statically position our tip on a rectangular array and perform continuous wave (CW) electron spin resonance (ESR) measurements as discussed in Chapter 3. A position is chosen at which the gradient is uniform and preferentially in the direction of the cantilever oscillations. A linear regression of the data then yields the gradient in the direction of oscillation (x) to be 53 ± 2.5MHz/μm, corresponding to 1900 T/m $\pm5\%$, see Figure A.2.

Incorporating the systematic uncertainty of the position, we estimate the error in the gradient to be 7%.

A.3 Calibration of the driving strength

Having measured the magnetic gradient at a specific location, we excite the tip to multiple excitation amplitudes that are much larger than that of Brownian motion, and perform a Hahn echo measurement, similar to those described in Chapter 3. Fitting to the resulting data allows us to convert the actuation signal into tip displacement. The accuracy of this

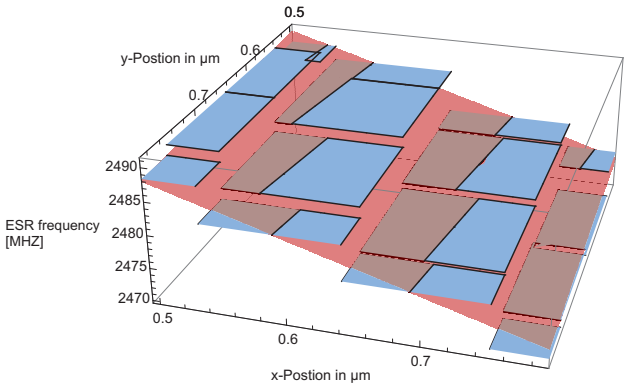

Figure A.2: Measurement of the CW ESR transition frequency vs. lateral tip position for 16 tip locations. The red plane corresponds to a linear regression of the data, corresponding to 53±2.5MHz/μm in the direction of tip oscillations (x).

fit is ±5%. We find that this calibration is consistent across a wide range of tip locations, gradients, and excitation amplitudes. Subsequently, we typically determine the gradient at a specific tip location by exciting the cantilever to a known motional amplitude and measuring the a.c. magnetic field amplitude using a Hahn echo sequence. Apart from enabling faster gradient characterization, this procedure also allows us to quantify the gradient at locations in which the gradient is not uniform on length scales of several hundred nanometers.

A.4 Error bars

For the data shown in Figure 3.3c in Chapter 3, the magnetic gradient is measured to be 2978 T/m ±9% using the three steps described above, while in Figure 3.3d it is 2940 T/m ±9%. With the additional standard error of the individual fits to the data the error bars can be calculated, as shown in Table B.2. Note that for increasing amplitude the imprecision is dominated by our uncertainty of the magnetic gradient. All error bars shown in this work correspond to one standard deviation.

Actuation strength [μV]	Amplitude [nT, pm] (rms)	Fit Standard Error [%]	Total Imprecision [%]
0 (Fig. 3c)	117, 40	7.7	12.1
0 (Fig. 3b)	113, 38	10.5	14.0
50	215, 72	11.1	14.5
100	376, 126	7.5	11.9
150	515, 173	4.3	10.2

Table A.1: Accumulated imprecisions of the (un-)driven motion

A.5 Calculation of the signal

A.5.1 Model

We treat the cantilever as a quantum mechanical oscillator coupled to an ohmic dissipative bath. This approach yields the classical result in the high temperature limit $T \gg \omega_r$, relevant for the current experiment, and also remains valid for a cantilever cooled near its ground state ($\hbar = k_B = 1$ throughout this supplement). This is required in our estimation of sensitivity to zero point motion. We describe the coupled NV-oscillator system by the Hamiltonian

$$\hat{H} = \frac{\Delta}{2}\hat{\sigma}_z + \frac{\lambda}{2}\left(\hat{a} + \hat{a}^\dagger\right)\hat{\sigma}_z + \hat{H}_{\rm osc}, \tag{A.1}$$

where $\hat{\sigma}_z$ is the Pauli operator describing the two level system of $|\uparrow\rangle = |m_s = 1\rangle$ and $|\downarrow\rangle = |m_s = 0\rangle$ in the spin-1 ground state of the NV center, and $\hat{a}$ is the annihilation operator of the oscillator. We ignore the $|m_s = -1\rangle$ state since it is detuned from the microwave manipulation by the applied d.c. magnetic field. $\Delta = 2.87$ GHz is the zero field splitting, ω_r is the oscillator frequency and $\lambda = g_e \mu_B G_m a_0$ is the coupling strength, where g_e is the Landé g-factor, μ_B is the Bohr magneton, G_m is the magnetic field gradient along the NV axis and $a_0 = \sqrt{1/2m\omega_r}$ is the zero point motion of the the cantilever mode. The damped oscillator is described by

$$\hat{H}_{\rm osc} = \omega_r \hat{a}^\dagger \hat{a} + \sum_k g_k \left(\hat{a} + \hat{a}^\dagger\right)\left(\hat{b}_k + \hat{b}_k^\dagger\right) + \sum_k \omega_k \hat{b}_k^\dagger \hat{b}_k, \tag{A.2}$$

where dissipation is described as coupling to a bath of harmonic oscillators with annihilation operators $\hat{b}_k$. We choose the coupling strengths g_k to correspond to standard ohmic dissipation.

The effect of π_x and π_y pulses in an echo, CPMG or XY4 sequence is to invert $\hat{\sigma}_z \rightarrow -\hat{\sigma}_z$, so we describe the pulses using a function $f(t,\tau)$ which toggles the sign of the interaction, with time τ between π pulses. In this way we write the Hamiltonian in the interaction picture with respect to $\hat{H}_0 = \frac{\Delta}{2}\hat{\sigma}_z + \hat{H}_{\rm osc}$ as

$$\hat{H}_{\rm int}(t) = \frac{\lambda}{2}\hat{\sigma}_z\hat{X}(t)f(t,\tau), \tag{A.3}$$

where $\hat{X} = \hat{a} + \hat{a}^\dagger$ and $\hat{X}(t) = e^{i\hat{H}_{\rm osc}t}\hat{X}e^{-i\hat{H}_{\rm osc}t}$. The function $f(t,\tau)$ is given in Table A.2 for spin echo and CPMG. The timing of π pulses described by $f(t,\tau)$ is the same for XY4 as for CPMG.

In an echo or CPMG measurement, the spin is prepared in a superposition which we take for simplicity to be $|\psi_0\rangle = \frac{1}{\sqrt{2}}(|\uparrow\rangle + |\downarrow\rangle)$. Since $\hat{\sigma}_z$ commutes with $\hat{H}$, the diagonal elements of the reduced spin density matrix do not evolve and the probability to find the spin in the initially prepared state, which is then converted to population in $|\uparrow\rangle$ by the final $\pi/2$ pulse, is $P_1(\tau) = \frac{1}{2}\left[1 + 2\Re\rho_{\uparrow\downarrow}(\tau)\right]$. The quantity of interest is the off-diagonal element of the reduced density matrix of the spin, $\rho_{\uparrow\downarrow} = {\rm tr}_{\rm osc}\hat{\rho}_{\uparrow\downarrow}$ where $\hat{\rho}_{\uparrow\downarrow} = \langle\uparrow|\,\hat{\rho}\,|\downarrow\rangle$ and $\hat{\rho}$ is the full spin-oscillator density operator. We obtain the standard result,

$$\rho_{\uparrow\downarrow}(\tau) = \rho_{\uparrow\downarrow}(0)D(\tau), \tag{A.4}$$

where the so-called decoherence function is

$$D(\tau) = \left\langle \tilde{\mathcal{T}}e^{-i\hat{\theta}/2}\mathcal{T}e^{-i\hat{\theta}/2}\right\rangle, \tag{A.5}$$

and $\mathcal{T}$ ($\tilde{\mathcal{T}}$) denotes time (anti-time) ordering. The accumulated phase operator is

$$\hat{\theta} = \lambda \int dt \hat{X}(t) f(t,\tau). \tag{A.6}$$

Since $\rho_{\uparrow\downarrow}(0) = 1/2$, the probability to find the spin in state $|1\rangle$ at the end of the measurement is

$$P_1(\tau) = \frac{1}{2}\left[1 + D(\tau)\right]. \tag{A.7}$$

In the present case we can evaluate Eq. (A.5) exactly for both thermal and driven motion, as we now discuss.

Name	Pulse sequence	$f(t)$	$F(z)$
Spin Echo	$\frac{\pi}{2} - \tau - \pi - \tau - \frac{\pi}{2}$	$\Theta(t) - 2\Theta(t-\tau) + \Theta(t-2\tau)$	$8\sin^4(z/2)$
CPMG	$\frac{\pi}{2} - \left(\frac{\tau}{2} - \pi - \frac{\tau}{2}\right)^{N/2} - \frac{\pi}{2}$	$\Theta(t) - \Theta(t-N\tau) + 2\sum_{j=1}^{N}(-1)^j \Theta\left[t - \left(j-\frac{1}{2}\right)\tau\right]$	$2\sin^2\left(\frac{Nz}{2}\right)\left[1 - \sec\left(\frac{z}{2}\right)\right]^2$

Table A.2: Pulse sequences and corresponding filter functions for spin echo and CPMG. The XY4 sequence is described by the same filter function as the CPMG sequence; only the axes (x or y) around which the π pulses are applied is different.

A.5.2 Signal from thermal motion

The decoherence function in Eq. (A.5) can be calculated by a cumulant expansion. Since $\hat{H}_{\rm osc}$ including dissipation is quadratic in $\hat{a}$ and $\hat{a}^\dagger$, the second order term in the expansion yields $D(\tau) = e^{-\chi(\tau)}$ exactly, and thus

$$P_1(\tau) = \frac{1}{2}\left(1 + e^{-\chi(\tau)}\right), \tag{A.8}$$

where

$$\chi(\tau) = \lambda^2 \int \frac{d\omega}{2\pi} \frac{F(\omega\tau)}{\omega^2} \bar{S}_X(\omega). \tag{A.9}$$

Here, $\bar{S}_X(\omega) = \int dt e^{i\omega t} \frac{1}{2}\left\langle \{\hat{X}(t), \hat{X}(0)\} \right\rangle$ is the symmetrized noise spectrum of $\hat{X}$ and the filter function is $F(\omega\tau) = \frac{\omega^2}{2}\left|\tilde{f}(\omega,\tau)\right|^2$ with $\tilde{f}(\omega,\tau) = \int dt e^{i\omega t} f(t,\tau)$. Filter functions for

spin echo and CPMG are provided in Table A.2. The symmetrized spectrum of the damped thermal oscillator described by $\hat{H}_{\rm osc}$ is

$$\bar{S}_X(\omega) = \frac{2\omega_r\gamma\omega}{(\omega^2-\omega_r^2)^2+\gamma^2\omega^2}\coth\left(\frac{\omega}{2T}\right), \tag{A.10}$$

where $\gamma = \omega_r/Q$ is the damping rate due to coupling to the ohmic environment. In the limit of finite $Q \gg 1$ we can approximate the oscillator spectrum by a Lorentzian,

$$\bar{S}_X(\omega) \simeq (\bar{n}_{\rm th}+1/2)\left[\frac{\gamma}{(\omega-\omega_r)^2+\gamma^2/4}+\frac{\gamma}{(\omega+\omega_r)^2+\gamma^2/4}\right], \tag{A.11}$$

where $\bar{n}_{\rm th} = \left(e^{\omega_r/T}-1\right)^{-1}$ is the average thermal occupation number. In this limit we obtain an analytic expression for an N pulse CPMG sequence,

$$\begin{aligned}\chi(\tau) =& \lambda^2(2\bar{n}_{\rm th}+1)\left\{q(N\tau)-\frac{4}{\omega_r^2+\gamma^2/4}\right. \\ &\left.\times\,\Re\left[\omega_-^2\sec\left(\frac{\omega_+\tau}{2}\right)\left[\frac{N}{2}e^{i\omega_+\tau/2}+ie^{iN\omega_+\tau/2}\sin\left(\frac{N\omega_+\tau}{2}\right)\left[\frac{1}{2}\sec\left(\frac{\omega_+\tau}{2}\right)-1\right]\right]\right]\right\}\end{aligned} \tag{A.12}$$

where we defined $\omega_\pm = \omega_r \pm i\gamma/2$ and

$$q(t) = \frac{1}{\omega_r^2+\gamma^2/4}\left[\frac{\gamma t}{2}+\frac{\omega_r^2-\gamma^2/4}{\omega_r^2+\gamma^2/4}\left(1-e^{-\gamma t/2}\cos\omega_r t\right)-\frac{\gamma\omega_r}{\omega_r^2+\gamma^2/4}e^{-\gamma t/2}\sin\omega_r t\right]. \tag{A.13}$$

We use this formula to fit the data in Figs. 2 and 3 in Chapter 3 in the limit of high $Q \gg 1$, and in the classical limit of high temperature, $T \gg \omega_0$. To estimate minimum phonon number sensitivity we approximate $\chi(\tau)$ at the point of maximum sensitivity, $\tau = \pi/\omega_r$, as we discuss below in Section A.6.

A.5.3 Signal from driven motion

Adding a resonant classical drive simply adds a nonfluctuating contribution to $\hat{X}(t)$. Due to the linearity in $\hat{X}$ of the accumulated phase (see Eq. (A.6)) we can decompose it as $\hat{\theta} = \theta_{\rm dr} + \hat{\theta}_{\rm th}$ where

$$\theta_{\rm dr} = \lambda \int dt A \cos(\omega_r t + \phi_0) f(t, \tau) \tag{A.14}$$

is the accumulated phase due to the drive. Here A is the amplitude of driven motion and ϕ_0 is the initial phase of the drive at the start of the measurement. In our experiment the cantilever drive is not phase-locked to the spin control sequence, so ϕ_0 is random and uniformly distributed. Inserting this into Eq. (A.5) and averaging over ϕ_0 we find

$$D(\tau) = \left\langle e^{-i\theta_{\rm dr}} \right\rangle_{\phi_0} \left\langle \tilde{\mathcal{T}} e^{-i\hat{\theta}/2} \mathcal{T} e^{-i\hat{\theta}/2} \right\rangle \tag{A.15}$$

The second factor is the same thermal contribution as found above, averaged with respect to $\hat{H}_{\rm osc}$, and the first factor is averaged over the uniformly distributed ϕ_0. Performing both averages we find the probability to find the spin in state $|1\rangle$ after the measurement is

$$P_1 = \frac{1}{2}\left(1 + J_0(a) e^{-\chi}\right) \tag{A.16}$$

where J_0 is the zeroth order Bessel function and $a = A\sqrt{2F(\omega_r \tau)}/\omega_r$. For a strong drive, the thermal fluctuations are unimportant and only the Bessel function is visible, as seen in Figure A.3b and in Figure 3.3a in Chapter 3. For a very weak drive both thermal and driven contributions are important, as seen in Figures 3.3B,C in Chapter 3, and in Figure A.3B. We use this expression to fit the driven measurements and extract the amplitude A of driven motion.

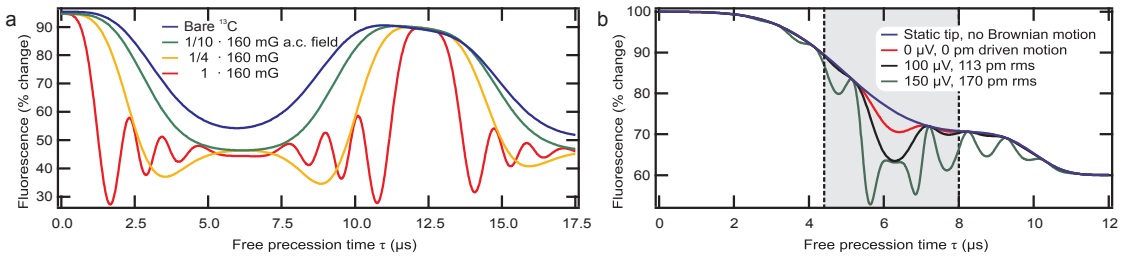

Figure A.3: Expected signal from the driven and thermal motion of the cantilever including the effect of the surrounding ^{13}C nuclear spin bath. (a) Expected echo signal for driven motion as shown in Figure 3.2b in Chapter 3. With the drive switched off (blue curve) only the collapses and revivals resulting from the Larmor precession of the ^{13}C nuclei are visible. The red curve shows the expected signal, including the effect of ^{13}C nuclei, from a 160 mG a.c. magnetic field from the driven cantilever as shown in Figure 3.2b. The green and orange curves show the signal at fractions of this amplitude, and illustrate the onset of Bessel fringes from the driven motion. (b) Expected signal from thermal and weakly driven motion for an XY4 sequence with $N = 12$ π-pulses as shown in Figure 3.3b in Chapter 3. The blue curve shows the signal from ^{13}C nuclei at low field ($\sim$10 G) in the absence of driven or thermal cantilever motion. The signal for thermal motion (red curve) and two weak driving voltages (black and green curves) corresponding to those in Figure 3.3 are also shown. The shaded region bounded by dotted lines corresponds to the region displayed in Figure 3.3b.

A.6 Sensitivity

A.6.1 Optimal phonon number sensitivity

In addition to dephasing due to the cantilever, the NV spin experiences dephasing from the surrounding bath of spin-$\frac{1}{2}$ ^{13}C nuclei in the diamond lattice. This enters as an additional decoherence factor, resulting in

$$P_1(\tau) = \frac{1}{2}\left(1 + e^{-N(\tau/T_2)^3} e^{-\chi(\tau)}\right) \tag{A.17}$$

in a sequence with N pulses. We are interested in the impact of the cantilever on the measured probability P_1, so we isolate the signal from the cantilever by writing $P_1(\tau) =$

$\frac{1}{2}\left(1+e^{-N(\tau/T_2)^3}\right)-S$, which defines the cantilever signal,

$$S=\frac{1}{2}e^{-N(\tau/T_2)^3}\left(1-e^{-\chi(\tau)}\right). \tag{A.18}$$

The sensitivity to thermal motion is set by the dependence of the signal S on $\bar{n}_{\rm th}$ at the point of maximum sensitivity, $\tau=\pi/\omega_r$. While $\chi(\tau)$ can be calculated exactly, we use an approximate solution to obtain a simple estimate of the sensitivity. In the $Q\gg 1$ limit the oscillator spectrum is approximately given by Eq. (A.11). In the $N\gg 1$ limit, the filter function at $\tau=\pi/\omega_r$ is approximately

$$F(\pi\omega/\omega_r)\simeq\frac{2N^2\gamma_N^2/4}{(\omega-\omega_r)^2+\gamma_N^2/4}, \tag{A.19}$$

where $\gamma_N=2\omega_r/N$ is the approximate bandwidth of the N-pulse CPMG sequence. Within these approximations we obtain

$$\chi(\pi/\omega_r)\simeq\frac{2N^2\lambda^2}{\omega_r^2}\left(\frac{2\bar{n}_{\rm th}+1}{1+N/2Q}\right). \tag{A.20}$$

Inserting $\bar{n}_{\rm th}=0$, this yields the optimal signal given in Eq. (1) in Chapter 3. The parameter $W=(1+N/2Q)^{-1}$ arises from the overlap of the cantilever spectrum with the filter function, each approximated as a Lorentzian.

To calculate the phonon number sensitivity we next need to account for the noise. We consider two contributions: the first is spin projection noise, which averaged over M measurements is $\sigma_{\rm proj}=1/\sqrt{M}$. Second is photon shot noise. The number of photons that discriminate between states $|0\rangle$ and $|1\rangle$ after M measurements is $\langle n_{\rm ph}\rangle=M(\alpha_0-\alpha_1)/2$, where α_0 or α_1 is the average number of photons collected per measurement when the NV spin is in state $|0\rangle$ or $|1\rangle$. The standard deviation in the number of photons collected per measurement is $\Delta n_{\rm ph}=\sqrt{M(\alpha_0+\alpha_1)/2}$, so the noise averaged over M measurements is $\sigma_{\rm shot}=\Delta n_{\rm ph}/\langle n_{\rm ph}\rangle=\sqrt{2(\alpha_0+\alpha_1)/M}/(\alpha_0-\alpha_1)$. Assuming the two noise sources are un-

correlated, the total noise averaged over M measurements is $\sigma = \sqrt{\sigma_{\rm proj}^2 + \sigma_{\rm shot}^2} = 1/K\sqrt{M}$, where $K = 1/\sqrt{1 + 2(\alpha_0 + \alpha_1)/(\alpha_0 - \alpha_1)^2}$. Since the number of N-pulse measurement sequences in total time $t_{\rm tot}$ is $M = t_{\rm tot}/N\tau$, we obtain $\sigma = \sqrt{N\tau}/K\sqrt{t_{\rm tot}}$ as given in Chapter 3. The phonon number sensitivity is given by $\eta = \bar{n}_{\rm min}\sqrt{t_{\rm tot}}$ where the minimum detectable phonon number is $\bar{n}_{\rm min} = \sigma/\left|dS/d\bar{n}_{\rm th}\right|$. We calculate the derivative using Eqs. (A.18) and (A.20), and obtain the expression for the sensitivity given in Chapter 3,

$$\eta = \frac{\sqrt{\pi}}{2KW\lambda^2} e^{N(\pi/\omega_r T_2)^3} \left(\frac{\omega_r}{N}\right)^{3/2}. \tag{A.21}$$

Plugging the experimental parameters from Figure 3.3D in Chapter 3 ($K \approx 0.015$, $Q \approx 220$, $N = 16$, $\omega_r = 80.15$ kHz, T_2=19 μs, $G_m = 2940$ T/m,) into Eq. (A.21), we arrive at an estimated sensitivity of $\eta \sim 2.5 \times 10^8$ phonons/$\sqrt{\rm Hz}$. Each data point in the figure was an average of 6×10^6 measurements for a total averaging time of ~ 720 seconds, which for the observed signal contrast at the point of maximum sensitivity, $\tau = \pi/\omega_r$, gives an observed experimental sensitivity $\eta_{exp} \approx 4.9 \times 10^8$ phonons/$\sqrt{\rm Hz}$.

A.6.2 Sensing zero point motion of a cooled oscillator

To prepare a mechanical oscillator of $\sim$ MHz frequency near its groundstate, active cooling below accessible environmental temperatures is required. Such cooling is always accompanied by an enhanced mechanical dissipation rate of $\tilde{\gamma} \sim \bar{n}_{\rm env}\gamma$, where $\bar{n}_{\rm env}$ is the occupation number at the environment temperature and $\gamma = \omega_r/Q$ is the intrinsic dissipation rate in the absence of cooling. This can be understood from the steady state phonon occupation number of a high Q mechanical oscillator being cooled by e.g. cavity photons [15,16] or a driven spin [5],

$$\bar{n} = \frac{\gamma_{\rm cool}\bar{n}_0 + \gamma\bar{n}_{\rm env}}{\gamma_{\rm cool} + \gamma}, \tag{A.22}$$

where $\gamma_{\rm cool}$ is the cooling rate and $\bar{n}_0$ is the final occupation number due to cooling in the absence of intrinsic damping γ. The oscillator is effectively coupled to two thermal baths: one consisting of the environment and the other consisting of the quantum system used for cooling. Both optomechanical and spin cooling mechanisms can reach $\bar{n}_0 < 1$, so to achieve $\bar{n}$ below one phonon requires $\gamma_{\rm cool} \sim \gamma \bar{n}_{\rm env} \gg \gamma$. This means the total effective damping is $\tilde{\gamma} \sim \gamma_{\rm cool}$, which is equivalent to a reduced quality factor of $Q_{\rm eff} = Q/\bar{n}_{\rm env}$.

For the calculation of the signal in Figure 3.4, we assumed near ground state cooling and thus set $\bar{n}_{\rm th} \to 0$ and $Q \to Q_{\rm eff}$ in Eq. (A.20). We calculated the signal using Eq. (A.12), including the effects of finite Q that were safely neglected in our estimate of optimal sensitivity. A result of keeping Q finite is that for very strong coupling, the cantilever itself leads to spin decoherence and thus a decrease in the signal, as seen in Figure 3.4b and pointed out in the corresponding caption. The reason for this is clear: once the coupling is strong enough to induce nearly complete collapse of $P_1(\tau)$, further increasing the coupling only increases decoherence due to the finite Q cantilever. This effect is not a concern in the present work, since it only arises for very strong coupling where the zero point motion can easily be detected, and far into the large cooperativity regime.

The cooperativity condition to sense zero point motion emerges directly from Eq. (1) in Chapter 3. From that equation we see that an appreciable signal of $S \sim 1/2$ is achieved when both $N(\pi/\omega_r T_2)^3 < 1$ and $N^2\lambda^2 W/\omega_r^2 < 1$. Using the effective quality factor $Q_{\rm eff}$ and taking the experimentally relevant limit, $Q_{\rm eff} \ll N$, we find $W \sim 2Q_{\rm eff}/N$. Combining the two inequalities and ignoring factors of order 1 we obtain the cooperativity condition, $C = \lambda^2 \tilde{T}_2/\tilde{\gamma} > 1$, where the effective spin decoherence time is $\tilde{T}_2 = N^{2/3} T_2$ and the effective cantilever dissipation rate is $\tilde{\gamma} = \omega_r/Q_{\rm eff}$.

Appendix B

Methods and analysis for the experiments presented in Chapter 4

B.1 System Hamiltonian and signal derivation

Because of the large zero-field splitting of the NV-spin $\mathbf{S}$ and moderate external magnetic fields, its interaction with the nearby nuclear spin $\mathbf{I}$ is treated within the secular approximation ($\mathbf{S} = S_z\hat{\mathbf{z}}$). The effect of the external magnetic field on the electron is undone by the echo sequence and therefore neglected ($\hbar = 1$). The reduced Hamiltonian is

$$H = S_z\mathbf{A}\cdot\mathbf{I} + \mu_{\mathrm{n}}\mathbf{I}\cdot\mathbf{B} \tag{B.1}$$

As the Hamiltonian is diagonal with respect to the NV spin, the nuclear spin evolves conditionally on the NV spin state in an effective magnetic field $\mathbf{B}_{m_s} = \omega_{m_s}\hat{\mathbf{n}}_{m_s}$; ($\omega_{m_s} = |\mu_n\mathbf{B} + m_s\mathbf{A}|, \hat{\mathbf{n}}_{m_s} = (\mu_n\mathbf{B} + m_s\mathbf{A})/\omega_{m_s}$).

$$H_{\mathrm{nuc}}[m_s] = \omega_{m_s}/2\boldsymbol{\sigma}\cdot\hat{\mathbf{n}}_{m_s} \tag{B.2}$$

In the experiment, the NV spin states $m_s = \pm 1$ are detuned, we can therefore treat the NV spin as a two-level system; here we restrict ourselves to $m_s = 0$ and $m_s = 1$. We define the nuclear spins states using the same convention as in [12], where $|\uparrow\rangle, |\downarrow\rangle$ are the eigenstates

of the ^{13}C nuclear spin when the NV electron spin is in the state $m_s = 1$. In the applied echo sequence the NV spin state is initially prepared in the $+\sigma_x$ direction (in the rotating frame); the nuclear state is in a completely mixed state, the initial state of the system is therefore given by the density matrix.

$$\rho_0 = \tfrac{1}{2}(\mathbb{1}_S + \sigma_x) \otimes \tfrac{1}{2}\mathbb{1}_I \tag{B.3}$$

As the final $\pi/2$-pulse rotates about the same axis as the initial one, we measure the expectation value $\langle\sigma_x\rangle$ (referred to as $\mathcal{S}$ in Chapter 4). The fluorescence rate (experimental signal p) is simply derived from this as

$$p = \frac{1}{2}(1 + \langle\sigma_x\rangle) \tag{B.4}$$

The expectation value is rewritten as ($\Re$ designates the real part)

$$\langle\sigma_x\rangle \equiv \mathrm{Tr}[\rho\sigma_x] = \Re\mathrm{Tr}[\rho(t)\sigma_+] = 2\Re\mathrm{Tr}_{\mathrm{nuc}}\langle 0|\rho|1\rangle \tag{B.5}$$

This is structurally similar to an interference amplitude of the two NV spin states $|0\rangle, |1\rangle$, subject to some evolution described by $\rho(t)$. Throughout the sequence, the NV spin is flipped $m_s = 0 \leftrightarrow m_s = 1$; in total N times, N is even (odd) in case of XY4 (PDD). Figure B.1 schematically shows the microwave manipulation of the sequences. Depending on the sequence the rotation axes are either $\hat{\mathbf{x}}$ (PDD and CP) or alternating $\hat{\mathbf{x}}$ and $\hat{\mathbf{y}}$ (XY4). The time evolution is generally given by

$$\mathcal{U} = \ldots \exp[-\tfrac{\mathrm{i}}{\hbar}H_{\mathrm{nuc}}[m_s]\tau_2] \exp[-\mathrm{i}\pi/2\sigma_x] \exp[-\tfrac{\mathrm{i}}{\hbar}H_{\mathrm{nuc}}[m_s]\tau_1] \tag{B.6}$$

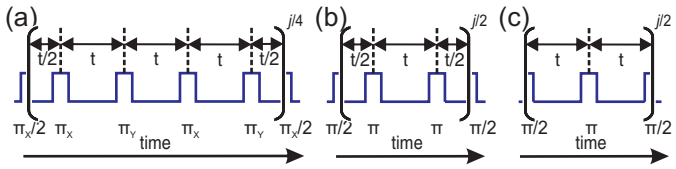

Figure B.1: Schematic Sequences, (a) XY4-N sequence with N being the total number of π-pulses. As the rotation axes $\hat{\mathbf{x}}$ and $\hat{\mathbf{y}}$ have the same effect on the time evolution operator, it can be deduced that the periodicity is shorter, as indicated in (b). (c) shows the PDD sequence.

Inserting (B.3),(B.6) in (B.5) and utilizing the commutator relations

$$\exp[\mathrm{i}\pi/2\sigma_{x,y}]H_{\mathrm{nuc}}[0] = H_{\mathrm{nuc}}[1]\exp[\mathrm{i}\pi/2\sigma_{x,y}] \text{ and vice versa} \tag{B.7}$$
$$\exp[\mathrm{i}\pi/2\sigma_y]\sigma_x = -\sigma_x\exp[\mathrm{i}\pi/2\sigma_y]$$

we obtain

$$\langle\sigma_x\rangle = \tfrac{1}{2}\Re\underbrace{\langle 0|(\mathbb{1}_S + (-1)^j\sigma_x)|1\rangle}_{(-1)^j}\mathrm{Tr}_{\mathrm{nuc}}[\exp[\mathrm{i}H_{\mathrm{nuc}}[0]\tau_n]\exp[\mathrm{i}H_{\mathrm{nuc}}[1]\tau_{n-1}][\ldots] \tag{B.8}$$
$$\times\exp[-\mathrm{i}H_{\mathrm{nuc}}[0]\tau_{n-1}]\exp[-\mathrm{i}H_{\mathrm{nuc}}[1]\tau_n]],$$

where j designates the total number of applied π-pulses around the y-axis. This is the only difference between a Carl-Purcell (CP-N) and XY4-N sequence [111]; in accordance with most publications we ignore that sign and set it to $+1$. The expression will now be evaluated in the case of PDD-N and (XY4)-N sequences. We identify repeating parts of the sequence and describe their total evolution by a single effective rotation around $\hat{\mathbf{n}}$ with angle ϕ, both depending on the evolution time t. From the last equation it is clear that a XY4-N sequence can be split into smaller repeating parts (referred to as XY below) (see Figure B.1b). In the experiment the XY4 sequence is utilized, as it decreases the impact of pulse imperfections compared to XY or PDD.

The repetition of these parts can then conveniently be carried by multiplying the total angle by the number of repetitions k. In case of XY4 (PDD) it applies $k = N/2$ ($k = (N+1)/2$)

$$\mathcal{U}_{\hat{\mathbf{n}}} \equiv (\mathcal{U}_{\mathrm{rep}})^k = (\mathbb{1}\cos\phi + \mathrm{i}\boldsymbol{\sigma}\underbrace{\hat{\mathbf{n}}\sin\phi}_{\equiv\mathbf{n}})^k = \mathbb{1}\cos k\phi + \mathrm{i}\boldsymbol{\sigma}\hat{\mathbf{n}}\sin k\phi \tag{B.9}$$

In equation (B.9) the product of two such rotations is regarded, arising from the $|0\rangle$ and $|1\rangle$ state of the NV spin. With the assumption that both rotations employ the same effective angle ϕ, yet different rotation axes $\hat{\mathbf{n}}, \hat{\mathbf{m}}$, we obtain

$$\begin{aligned}\mathcal{U}_{\hat{\mathbf{n}}}\mathcal{U}_{\hat{\mathbf{m}}} =& \mathbb{1}(\cos^2 k\phi + \hat{\mathbf{n}}\hat{\mathbf{m}}\sin^2 k\phi) + \mathrm{i}\boldsymbol{\sigma}((\hat{\mathbf{n}}+\hat{\mathbf{m}})\sin k\phi\cos k\phi - \hat{\mathbf{n}}\times\hat{\mathbf{m}}\sin^2 k\phi) \\ =& \mathbb{1}(T_k^2(\cos\phi) + \mathbf{nm}U_{k-1}^2(\cos\phi)) + \mathrm{i}\boldsymbol{\sigma}((\mathbf{n}+\mathbf{m})T_k(\cos\phi)U_{k-1}(\cos\phi) \\ & - \mathbf{n}\times\mathbf{m}U_{k-1}^2(\cos\phi))\end{aligned} \tag{B.10}$$

Where in the last step the Chebyshev polynomials are utilized. Inserting this into eq. (B.9) we obtain (utilizing Pell's equation $T_k^2(\cos\phi) + \cos^2\phi U_{k-1}^2(\cos\phi) = 1$)

$$\begin{aligned}\langle\sigma_x\rangle =& T_k^2(\cos\phi) - \mathbf{nm}U_{k-1}^2(\cos\phi) = 1 - (1 + \mathbf{nm} - \cos^2\phi)U_{k-1}^2(\cos\phi) \\ =& T_k^2(\cos\phi) - \frac{\mathbf{nm}}{1-\cos^2\phi}(1 - T_k^2(\cos\phi))\end{aligned} \tag{B.11}$$

The second equation is useful to determine the boundaries of the signal for all possible number of repetitions k.

B.1.1 XY4 SEQUENCE

In the case of XY4 the iterative part of the sequence can be expressed as (see Figure B.1); we use the abbreviation $\phi_{m_s} = \omega_{m_s} t/2$

$$\begin{aligned}\mathcal{U}_1[t/2]\mathcal{U}_0[t]\mathcal{U}_1[t/2] =& \mathbb{1}(\cos\phi_0\cos\phi_1 - \hat{\mathbf{n}}_0\cdot\hat{\mathbf{n}}_1\sin\phi_0\sin\phi_1) \\ &+\mathrm{i}\boldsymbol{\sigma}\cdot(-\hat{\mathbf{n}}_0\sin\phi_0\cos\phi_1 - \hat{\mathbf{n}}_1\sin\phi_1\cos\phi_0 \\ &+2\hat{\mathbf{n}}_1\times(\hat{\mathbf{n}}_1\times\hat{\mathbf{n}}_0)\sin^2\phi_1/2\sin\phi_0) \\ \equiv& \mathbb{1}\cos\phi + \mathrm{i}\boldsymbol{\sigma}\hat{\mathbf{n}}\sin\phi = \mathbb{1}\cos\phi + \mathrm{i}\boldsymbol{\sigma}\mathbf{n}\end{aligned} \tag{B.12}$$

and

$$\begin{aligned}\mathcal{U}_0^\dagger[t/2]\mathcal{U}_1^\dagger[t]\mathcal{U}_0^\dagger[t/2] =& \mathbb{1}(\cos\phi_0\cos\phi_1 - \hat{\mathbf{n}}_0\cdot\hat{\mathbf{n}}_1\sin\phi_0\sin\phi_1) \\ &+\mathrm{i}\boldsymbol{\sigma}\cdot(\hat{\mathbf{n}}_0\sin\phi_0\cos\phi_1 + \hat{\mathbf{n}}_1\sin\phi_1\cos\phi_0 \\ &-2\hat{\mathbf{n}}_0\times(\hat{\mathbf{n}}_0\times\hat{\mathbf{n}}_1)\sin^2\phi_0/2\sin\phi_1) \\ \equiv& \mathbb{1}\cos\phi + \mathrm{i}\boldsymbol{\sigma}\hat{\mathbf{m}}\sin\phi\end{aligned} \tag{B.13}$$

Inserting $\mathbf{n}, \mathbf{m}$ and $\cos\phi$ into eq. (B.11), we obtain the explicit result with $\cos\phi$ given by the preceding equations.

$$\langle\sigma_x\rangle = 1 - 4(1 - (\hat{\mathbf{n}}_0\hat{\mathbf{n}}_1)^2)\sin^2\phi_0/2\sin^2\phi_1/2\,(1-\cos\phi)\,U_{k-1}^2(\cos\phi) \tag{B.14}$$

We now regard the solution written in the form (B.12). As $0 \leq \ T_k^2[|x| < 1] \leq 1$, the fraction in the equation represents the lower limit of the signal independent of number of repetitions k, see FigureB.2. In particular, the absolute minimum is obtained when the axes of the effective rotations $\mathbf{n}, \mathbf{m}$ are parallel. As they have the same length, they are

identical $\mathbf{n} = \mathbf{m}$. Inserting this into eqs. (B.13),(B.14) yields the two conditions.

$$\begin{aligned} &\sin\phi_0\cos\phi_1 + \sin^2\phi_1/2\sin\phi_0 - \hat{\mathbf{n}}_0\hat{\mathbf{n}}_1\sin^2\phi_0/2\sin\phi_1 = 0 \\ &\sin\phi_1\cos\phi_0 + \sin^2\phi_0/2\sin\phi_1 - \hat{\mathbf{n}}_0\hat{\mathbf{n}}_1\sin^2\phi_1/2\sin\phi_0 = 0 \end{aligned} \tag{B.15}$$

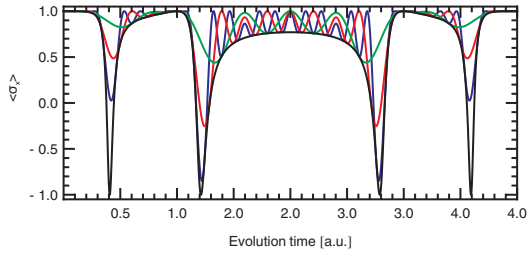

Figure B.2: Signal strengths for varying number of repetitions (green, red, blue: XY 2,4,6; respectively); the black curve is the lower boundary to all the possible XY sequences.

B.1.2 PDD SEQUENCE

The evolution can be written as

$$\begin{aligned} \mathcal{U}_0[t]\mathcal{U}_1[t] =& \mathbb{1}(\cos\phi_0\cos\phi_1 - \hat{\mathbf{n}}_0\cdot\hat{\mathbf{n}}_1\sin\phi_0\sin\phi_1) \\ &+\mathrm{i}\boldsymbol{\sigma}\cdot(\hat{\mathbf{n}}_0\sin\phi_0\cos\phi_1 + \hat{\mathbf{n}}_1\sin\phi_1\cos\phi_0 - \sin\phi_0\sin\phi_1\hat{\mathbf{n}}_0\times\hat{\mathbf{n}}_1) \\ &\equiv \mathbb{1}\cos\phi + \mathrm{i}\boldsymbol{\sigma}\hat{\mathbf{n}}\sin\phi = \mathbb{1}\cos\phi + \mathrm{i}\boldsymbol{\sigma}\mathbf{n} \end{aligned} \tag{B.16}$$

$\hat{\mathbf{m}}$ is obtained by reversing the angles $\phi_0 \to -\phi_0, \phi_1 \to -\phi_1$, inserting this into eq. (B.11) yields the result for PDD.

$$\langle\sigma_x\rangle = 1 - 2(1 - (\hat{\mathbf{n}}_0\hat{\mathbf{n}}_1)^2)\sin^2\phi_0\sin^2\phi_1 U_{k-1}^2(\cos\phi) \tag{B.17}$$

Which is easily seen to reduce to the well known result for Hahn spin-echo as $U_{k-1=0} = 1$.

B.2 Background due to the spin bath

We treat the impact of the bath of ^{13}C spins as a classical magnetic field, whose frequency distribution $\bar{S}(\omega)$ is a weighted Gaussian centered at the Larmor precession frequency due to the external field, giving rise to decaying collapses and revivals. Please note that this does not include the dominant part of the decoherence, which is a result of low-frequency noise due to flip-flop processes within in the bath, see e.g. [159, 160]. The coherence envelope $\langle\langle\sigma_+\rangle\rangle$ in the system may be written as

$$\langle\langle\sigma_+\rangle\rangle = \exp[-\chi[t]] \equiv \exp\left[-\int \frac{d\omega}{2\pi}\frac{F(\omega t)}{\omega^2}\bar{S}(\omega)\right] \tag{B.18}$$

Here $F(z)$ defines the sequence-dependent filter function (see Appendix A for details); it takes the form

$$F(z) = a_0 + \sum_n a_n \cos(nz/2) \tag{B.19}$$

Assuming the width σ of the Gaussian distribution to be narrow $\sigma \ll \omega_0$ we can simplify it as

$$\bar{S}(\omega) = \tilde{\lambda}^2\omega_0^2 \exp[-(\omega-\omega_{\rm L})^2/(2\sigma^2)] \approx \tfrac{\sqrt{2\pi}}{\sigma}\lambda^2\omega^2 \exp[-(\omega-\omega_{\rm L})^2/(2\sigma^2)] \tag{B.20}$$

$\chi(t)$ can be easily integrated piecewise, yielding

$$\chi(t) = \lambda^2\left(a_0 + \sum_n a_n \exp(\tfrac{1}{8}n^2t^2\sigma^2)\cos(nt\omega_0)\right) \tag{B.21}$$

The high frequency components in the filter function die out faster, as shown in Figure B.3.

In addition, the low frequency components in magnetic noise lead to a dominant overall decay in coherence. Increasing the number N of π-pulses in a sequence reduces the susceptibility to low frequency noise and thereby enhances the effective coherence time $T_2^{\rm eff}$,

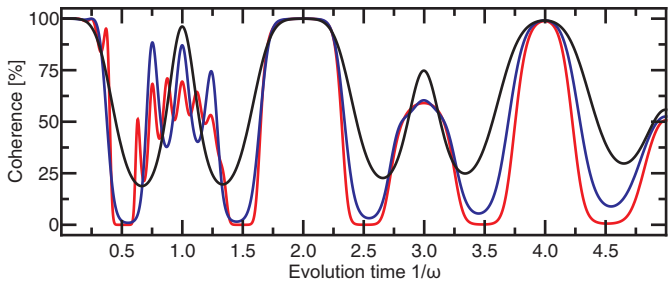

Figure B.3: Simulated bath decoherence, XY-2,4,8 (black, blue, red, respectively) $\sigma = 0.1\omega/(2\pi), \lambda = 0.25$. Faster oscillations can be seen to be damped more quickly.

see. [77, 111].

$$\langle\langle\sigma_+\rangle\rangle_{\text{lowfreq}} = \exp\left[-k\left(\frac{2t}{T_2}\right)^3\right] \equiv \exp\left[-\left(\frac{2t}{T_2^{\text{eff}}}\right)^3\right] \tag{B.22}$$

We include this term when we regard a revival of the bath induced coherence (Figure 4.3 in the Chapter 4) and use it for scaling arguments when analyzing the limits of our method.

B.3 Approximation of the hyperfine interaction

For the following discussion, we regard the situation in which the coordinate system is chosen such that the z-axis coincides with the symmetry axis of the NV center, the NV spin's center of mass defines the origin, and the ^{13}C lies within the x-z plane, (a special case of the more general case shown in Figure B.4). Motivated by its small magnitude, we treat the hyperfine coupling as rotationally symmetric about z, reducing the hyperfine interaction $\mathbf{A}$ to $\mathbf{A} = \{A_x, 0, A_z\}$. As the NV wavefunction is not perfectly rotationally symmetric, it can potentially produce a magnetic field at the ^{13}C location that has components in the $\hat{\mathbf{y}}$ direction, which we neglect here. From the consistency of our fits we infer that these terms are small.

Previous works have observed an enhanced ^{13}C gyromagnetic ratio for transverse fields, arising from coupling to the NV electronic spin (see for example [12].) This enhancement of the gyromagnetic ratio is a result of corrections to the secular approximation that we

do not consider as they are negligible when the coupling $\mathbf{A}$ is weak enough such that $\mu_e/\mu_n \ll \Delta/|\mathbf{A}|$, as is the case for all ^{13}C spins considered in this work.

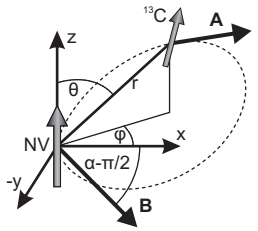

Figure B.4: Definition of the coordinate system. The z-axis is defined by the symmetry axis of the NV center, while the x-axis is defined such that the magnetic field vector $\mathbf{B}$ always lies within the x-z plane as the magnet is rotated. The angle of magnetic field rotation α is defined relative to the z-axis, but the arc is shown here without the first $\pi/2$ segment from the z to x axes for clarity. The position of the ^{13}C relative to the NV is then given by the spherical coordinates r, ϕ, and θ, while $\mathbf{A}$ is the hyperfine coupling vector resulting from this spatial configuration.

B.4 Signal strength vs. number of applied pulses

When the hyperfine coupling strength $|\mathbf{A}|$ exceeds the bare Hahn echo decoherence rate $1/T_2$, a strong signal can be obtained without requiring the enhanced coherence T_2^{eff} afforded by using extended sequences. We therefore numerically investigate the maximal impact $p_{\max}$ of an individual nuclear spin in the regime $1/T_2 > |\mathbf{A}|$ using extended sequences.

First we consider the impact arising from the coherent evolution described by eq. (B.14) which is exponentially suppressed by low frequency noise, see eq. (B.22). We neglect for the time being the impact of the Larmor procession of the surrounding bath. We therefore regard an expression of the form

$$p = \tfrac{1}{2}\left[1 - \langle\sigma_x\rangle\right]\langle\langle\sigma_+\rangle\rangle \tag{B.23}$$

We calculate the maximum signal $p_{\max}$ for a given coupling strength $|\mathbf{A}|$, the orientation and strength of the external magnetic field as well as the evolution time t are optimized

numerically. Figure B.5 shows the result. The signal strength can be seen to scale with

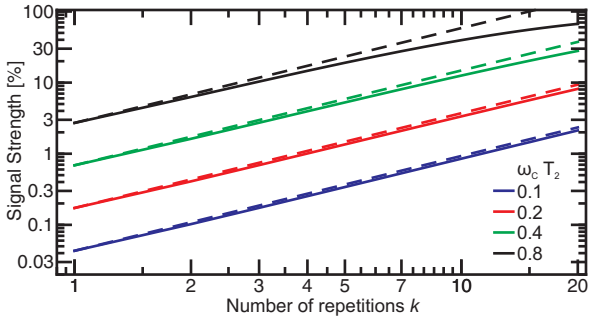

Figure B.5: Numerically calculated signal strength vs. number of pulses and coherence time; the dashed lines highlight the scaling as $k^{4/3}$

the number of repetitions k as $k^{4/3}$; this can be understood as follows: ideally, the phase accumulated by the NV spin from its interaction with the ^{13}C increases linearly with the number of repetitions k and the evolution time t. For small accumulated phases, this leads to a quadratic increase in signal strength. One therefore obtains

$$p \propto t^2 k^2 \exp\left[-k\left(\frac{2t}{T_2}\right)^3\right]; \quad \frac{\partial p}{\partial t} = 0 \quad \Rightarrow \quad t \propto k^{-1/3} \text{ and } p_{\max} \propto k^{4/3} \tag{B.24}$$

However, if the investigated spin is a ^{13}C in a sample of natural isotopic abundance, one has to include the collapses and revivals in coherence coming from the Larmor precession of the ^{13}C bath spins at frequency ω_L. For $\omega_L \gg |\mathbf{A}|$, as would be required for large k, the signal p tends to peak at $t \approx \pi/\omega_L(1/2 + n)$, where n is an integer; however the signal in this range is exponentially suppressed due to the collapses from the bath. We therefore find that in this case there is no enhancement in the maximal impact $p_{\max}$ with k.

B.5 Additional measurements supporting Chapter 4

B.5.1 Ramsey measurements

We infer the inhomogeneous dephasing rate $1/T_2^*$ of the NV spin from Ramsey measurements, as shown in Figure B.6. The result can be accurately reproduced taking only the coupling to the nuclear spin of the nitrogen into account (coupling strength: 2.2 MHz). We measure up to an evolution time of 40 µs to ensure that there are no revivals in coherence.

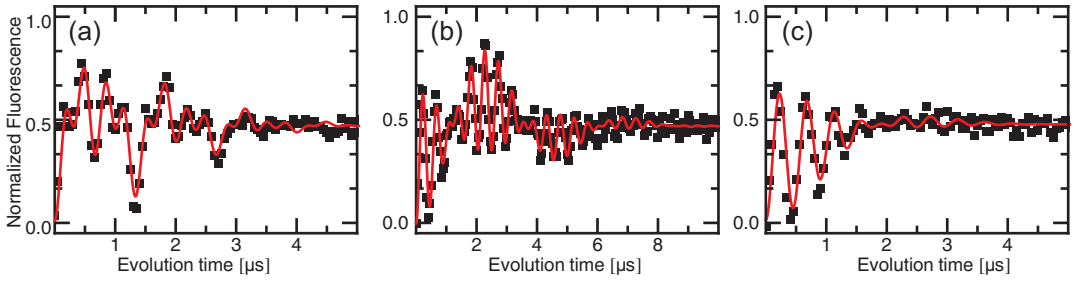

Figure B.6: Ramsey measurements of the NV centers investigated in Chapter 4. Data shown in (a), (b) and (c), corresponds to the NV data shown in Figures 4.2, 4.3, and 4.4 in Chapter 4, respectively. Extracted T_2^* are $2.5 \pm 0.1, 4.6 \pm 0.2, 1.8 \pm 0.2$ µs, respectively.

B.5.2 Consistency of Ramsey and XY4 measurements

As a consistency check of our method, we show in Figure B.7 measurements performed on an NV center with a strongly coupled ^{13}C,where $\mathbf{A} > 1/T_2^*$. We measure its impact on the NV spin evolution in a XY4-8 measurement (a,b) as well as in a Ramsey sequence (c,d). The extracted hyperfine couplings are 422 kHz (Ramsey) and 438 kHz (XY4-8); these values are larger the inhomogeneous dephasing rate 286 kHz.

B.5.3 Additional XY4-8 measurements - complementing Figures 4.2,4.4

In Figure B.8 we show additional data from the data sets used to generate the fits shown in Figures 4.2 and 4.4 of Chapter 4. In general, we measure the NV response while varying

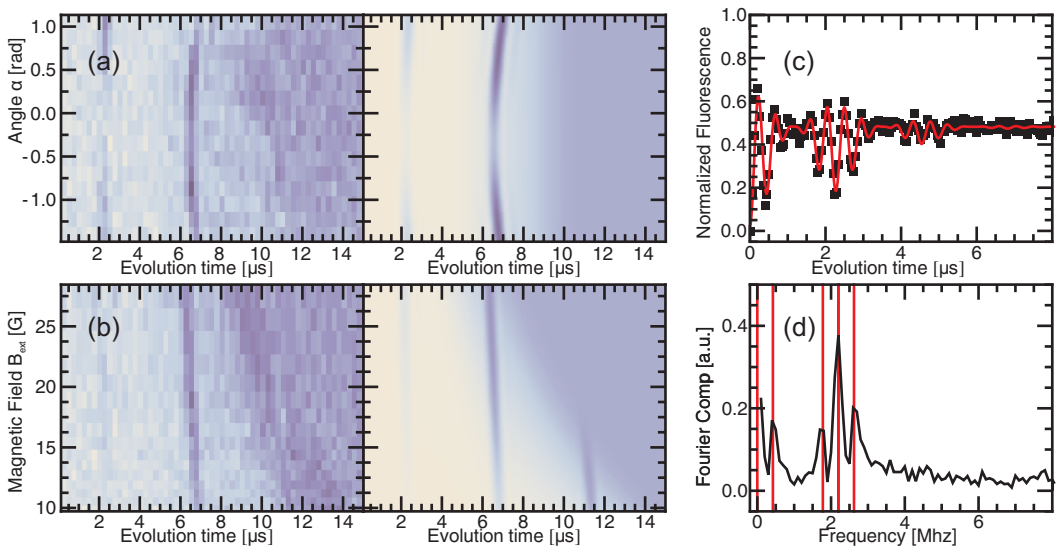

Figure B.7: XY4-8 and Ramsey measurements. (a) and (b) display XY4-8 measurement and fit vs. magnetic field orientation and strength, respectively. (c) shows a Ramsey measurement performed on the same NV, it is fitted incorporating an additional energy splitting due to the coupling to the ^{13}C. (d) is the fourier transform of the data shown in (c). In addition to the 2.2 MHz splitting from the nitrogen, a clear splitting due to the hyperfine coupling is visible; lines mark the position of the peaks as determined from (c).

magnetic field strength with fixed orientation, and while varying magnetic field orientation with fixed strength, for both possible superpositions of magnetic sublevels: $\frac{1}{\sqrt{2}}(|0\rangle + |1\rangle)$ and $\frac{1}{\sqrt{2}}(|0\rangle + |-1\rangle)$. Changing which of the $|\pm 1\rangle$ electron spin states we address effectively flips the sign of the hyperfine interaction relative to the magnetic field, helping to pin down the precise hyperfine vector. In Chapter 4, all data shown is for the NV in the superposition $\frac{1}{\sqrt{2}}(|0\rangle + |1\rangle)$. In Figure B.8(c) the double dip resulting from the two ^{13}C spins with similar coupling strengths can be seen to split apart as the magnetic field strength is varied, enabling the individual entanglement of each ^{13}C with the NV by choosing the appropriate magnetic field and evolution time.

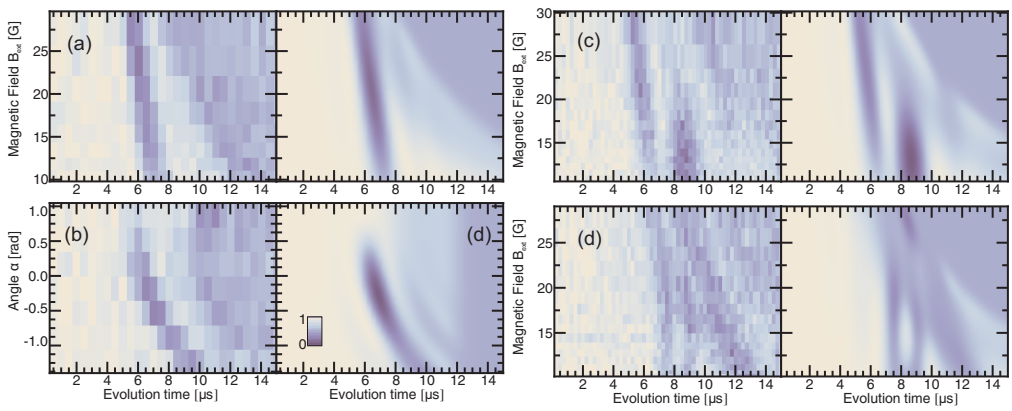

Figure B.8: Additional measurements and simulations for the NVs shown in Figures 4.2 and 4.4 of Chapter 4, showing the NV response vs magnetic field strength (a,c,d) and orientation (b). (a and b) Signal when the NV shown in Figure 4.2 (Chapter 4) is in a superposition of $\frac{1}{\sqrt{2}}(|0\rangle+|-1\rangle)$. (c,d) The data set corresponding to the NV shown in Figure 4.4 of Chapter 4 when the NV is in the superposition (c): $\frac{1}{\sqrt{2}}(|0\rangle + |1\rangle)$, and (d): $\frac{1}{\sqrt{2}}(|0\rangle + |-1\rangle)$.

B.5.4 Additional XY4 measurements - complementing Figure 4.3

In Figure B.9 we show additional data for the NV with the weakest coupled ^{13}C observed, (Figure 4.3 of Chapter 4). The experimental settings are the same as those of Figures 4.2 and 4.4 in Chapter 4, but here XY4-16 is used in place of XY4-8 to further enhance any impact of the weakly coupled ^{13}C. No clear impact from the ^{13}C is observed, which is consistent with our calculated response based on the fit displayed in Chapter 4. This illustrates why it was necessary to measure within the spin bath revival at longer evolution times in order to detect this ^{13}C.

B.6 Parameter table of investigated NV Centers

In table B.1 we present the extracted parameters from the NV centers we observed that could be treated within the framework derived above. In particular, NVs with strongly coupled ^{13}C spins ($|\mathbf{A}| > 1$MHz) were not investigated in detail. The hyperfine coupling strengths $\mathbf{A}$ are determined from the fits to the XY-4 measurements; the extracted distance

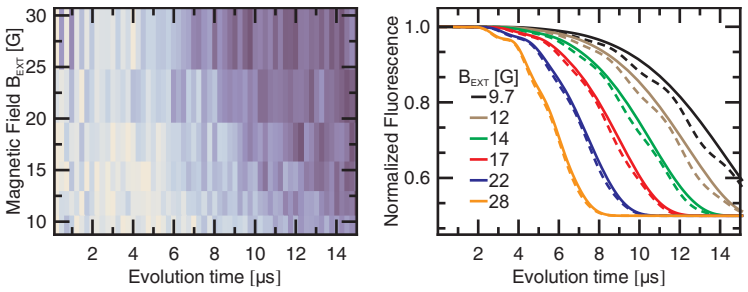

Figure B.9: (a) Measurement of NV subject to a XY4-16 sequence. (b) Calculated response (solid lines) of the NV obtained by fitting (B.21) to the data shown in (a); dashed lines include the additional effect of the isolated nearby ^{13}C based on the coupling parameters extracted from the fit to the data shown in Figure 4.3 in Chapter 4.

r and angle θ (defined in Figure B.4,) are based on the assumption of point-like dipole interactions, see Chapter 4 for details and discussion.

NV index	T_2^* [μs]	# of ^{13}C spins	A_x [kHz]	A_z [kHz]	$\|\mathbf{A}\|$ [kHz]	r [Å]	θ [deg]	appears in Figure
1	2.5	1	100	-75	126	5.6	18	4.2,B.6,B.8
2	4.6	1	-40	-22	46	8.0	-22	4.3,B.6
3	3.5	1	-222	-359	422	3.6	-10	B.7
4	2.0	2	180	-51	187	5.1	27	-
			63	-61	88	6.3	15	-
5	1.8	3	98	97	138	6.3	60	4.4,B.6,B.8
			115	-13	116	6.1	32	4.4,B.6,B.8
			37	-52	64	6.9	12	4.4,B.6,B.8

Table B.1: Extracted parameters from XY4-8 and Ramsey measurements.

B.7 Scaling of T_2^* with concentration

The data presented in Table B.1 shows a strong inverse correlation between coupling strength to the nearest neighbor ^{13}C and T_2^*, and implies that the average single NV T_2^* time will depend on ^{13}C concentration. While the dependence of average T_2 on ^{13}C concentration was been considered in detail [161], the T_2^* has only been considered briefly in

Mizuochi *et al.* [162] and Balasubramanian *et al.* [59], and their conclusions appear to be inconsistent with more recent experimental results, so we discuss the matter here. We are interested in the scaling of the average individual nitrogen-vacancy center's T_2^* time with the concentration of paramagnetic impurities, C. We will focus for the time being exclusively on ^{13}C impurities, as this is what limits T_2^* in most samples, and later on we will generalize to other impurities. Reference [162] has the most extensive study of T_2^* versus ^{13}C concentration, but we were able to find three other data points for isotopically purified samples, in references [59, 60, 151]. All the results are summarized in Table B.2.

Concentration C (%)	T_2^* (μs)	Linewidth (kHz)	Reference
0.01	470	1	Maurer *et al.*
0.01	228	1	Zhao *et al.*
0.03	30	15	Mizuochi *et al.*
0.3	10	44	Balasubramanian *et al.*
0.35	6.6	67	Mizuochi *et al.*
1.1	2.5	176	Mizuochi *et al.*
8.4	.025	18000	Mizuochi *et al.*
20.7	.015	30000	Mizuochi *et al.*
100	.007	60000	Mizuochi *et al.*

Table B.2: Accumulated T_2^* vs ^{13}C concentration data

It is immediately apparent that there is a dramatic increase in T_2^* when the concentration is decreased from 8.4% to 1.1%. This is because between these two concentrations the nature of the interaction between the NV and the average nearest neighbor ^{13}C crosses over from the contact interaction to the weaker dipole-dipole interaction. This cross-over is discussed in detail in reference [162], and because the scaling of the interaction is more complicated and the model proposed in [162] (namely $T_2^* \propto 1/\sqrt{C}$) seems to describe the high concentration data quite well, we will restrict the remainder of this section to analyzing small concentrations, $C \leq 1.1\%$, where the average nearest neighbor coupling can be treated as strictly dipolar.

References [162] and [59] both use an isotropic hyperfine coupling model adapted from P donors in ^{29}Si to model T_2^* as a function of C. Specifically, they sum the hyperfine coupling contribution of each lattice site multiplied by the concentration (or in other words the probability there actually is a spin at that site) to arrive at a scaling of $T_2^* \propto 1/\sqrt{C}$. While this model does an excellent job of describing the data presented in [162], it fails to adequately account for the results of [60], [151], and [59] (see Figure B.10). Intuitively, this makes sense, as at lower concentrations it seems odd to include the contributions of nearby lattice sites that are most likely not occupied by nuclear spins, and which contribute disproportionately to the dephasing predicted by the model due to the r^{-3} scaling of the dipolar interaction. We therefore propose a simple alternative model that seems to better describe the low concentration data.

We follow the basic prescription laid out in reference [161] to model T_2 with concentration, but with some simplifying assumptions as we are interested in T_2^*. In particular, we assume that T_2^* is limited by the hyperfine coupling A to the nearest neighbor impurity, that the spin state of the impurity is static for the timescales of a single Ramsey measurement, but that the spin state is randomized from measurement to measurement. While the coupling to a single spin can be coherent and lead to collapse and revivals in the Ramsey measurement, we assume that on average most NVs will have other spins with comparable but smaller couplings that don't contribute significantly to the collapse, but suppress the revivals (of course some NVs will have shorter or longer T_2^* times than predicted by our model depending on their random spin environment, but on average we should be in the right ball park.) According to [59], the average distance to the nearest neighbor impurity r_{nn} as a function of concentration C is given by:

$$r_{nn} \approx \frac{3}{10}\frac{a}{C^{1/3}} \tag{B.25}$$

where a =3.57 Å is the lattice constant of diamond. Eq. B.25 was checked numerically by

randomly populating a ∼3000 site diamond lattice many times and taking the mean r_{nn} for each concentration, and was found to be in excellent agreement. The strength of the dipole-dipole interaction between an NV and a ^{13}C a distance r away is given by

$$A \approx \frac{\mu_o g_e \mu_e g_N \mu_N}{4\pi\hbar} \frac{1}{r^3} \tag{B.26}$$

where we have assumed both dipoles are oriented along the same axis (valid for a magnetic field oriented along the NV axis.) Therefore, as r_{nn} scales with $C^{-1/3}$, and A scales with r^{-3}, we arrive at $T_2^* \approx 2\pi/A_{nn} \propto 1/C$. In other words, just as was found in [161] for T_2, at low concentrations T_2^* scales inversely with concentration. Plugging in numbers, a simple order of magnitude estimate gives $T_2^* = 3 \times 10^{-8}/C$, which we plot against the data from Table B.2, and compare to the model given in [162] and [59]. Our rough model actually agrees with the data quite well, except for one outlier point from [162].

Adapting our model to impurities with electronic spin (such as nitrogen,) is relatively simple. While the assumption that the spin of the nearest neighbor impurity remains static over the course of a single measurement is no longer valid due to the faster electron spin bath dynamics, this can be accounted for by including a time constant τ_c for the average amount of time before the spin of the nearest neighbor impurity flips. It can be shown that in this case $T_2^* \approx \sqrt{2\pi\tau_c/A_{nn}}$. Since the time constant τ_c is determined by the electron-electron dipolar interactions between the nearest neighbor spin and the bath, and this is determined by the mean distance between electron spin impurities, the exact same arguments as presented above apply, and $\tau_c \approx 2\pi/A_{nn}$, so again the scaling is the same, $T_2^* \approx 2\pi/A_{nn} \propto 1/C_N$, where C_N is the nitrogen concentration. The only difference is that A_{nn} is now ∼1000 times stronger, because it is an electron-electron dipolar interaction instead of an electron-nuclear interaction. Plugging this into our simple order of magnitude estimate gives $T_2^* = 3 \times 10^{-11}/C_N$, indicating that in a sample with a natural isotopic abundance of ^{13}C, a nitrogen concentration of $\sim 10^{-5}$ (10 ppm) or higher would begin to

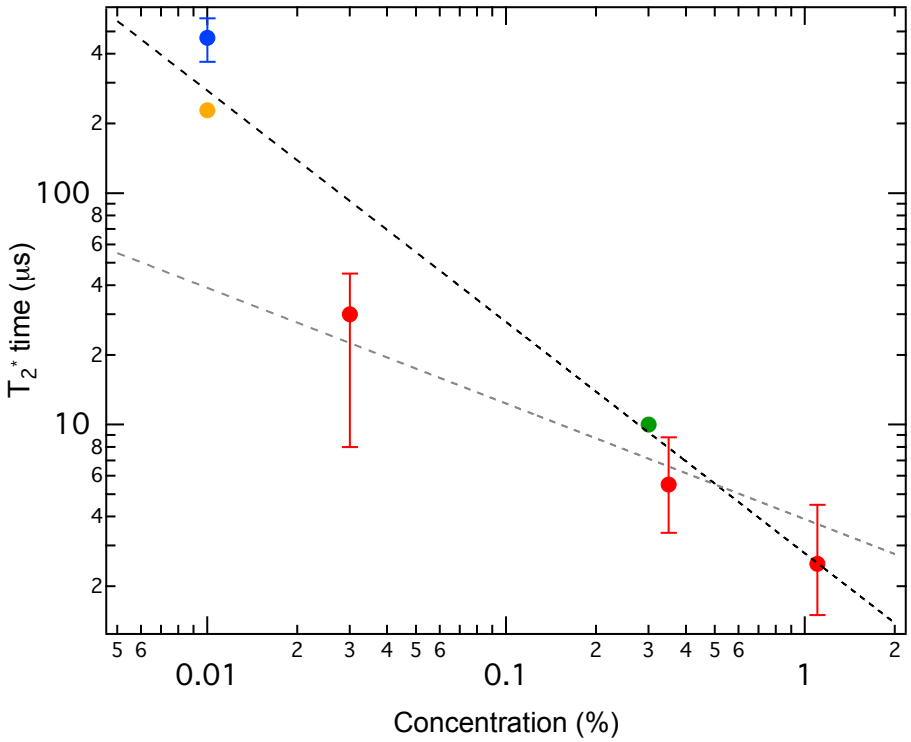

Figure B.10: T_2^* vs ^{13}C concentration. Data from Mizuochi *et al.* (red points), Maurer *et al.* (blue point), Zhao *et al.*(orange point), and Balasubramanian *et al.* (green points), with error bars when stated. The grey dashed line is the model presented in Mizuochi *et al.* and Balasubramanian *et al.*, in which $T_2^* \propto 1/\sqrt{C}$, while the black dashed line is the model presented here, with $T_2^* \propto 1/C$.

limit T_2^*.

Finally, it is worth noting that all of the above ignores other potential limitations to T_2^*, such as the fundamental limit of T_1, which at room temperature is ∼5 ms, or magnetic field noise from other sources outside the diamond sample. Decreasing the concentration of impurities below these limits will no longer improve T_2^*, although at low temperatures with magnetic shielding both these limits could be quite low, and giving very long T_2^* times.

Appendix C

Methods and analysis for the experiments presented in Chapter 5

C.1 Experimental materials and methods

The experiments were performed using 30 micron thick electronic grade diamonds grown, thinned, and polished by Element Six with a natural isotopic abundance of carbon. Shallow NV centers were generated through Nitrogen-14 implantation at 6 keV energy at a density of $2\times10^9/\text{cm}^2$, followed by annealing at 800 ^{o}C. The single-crystal silver films were grown by sputtering at 300 ^{o}C onto a (111) oriented single-crystal silicon substrate [137, 138], with a deposition rate of $\sim$1.5 nm/s, as discussed in detail in section C.2.1. The polycrystalline silver films were evaporated directly onto the diamond. A 5-nm layer of silica (SiO_2) was grown on the diamond surface prior to the metal deposition to preserve NV properties. Temperature dependence measurements were performed in a Montana Instruments closed cycle cryostat.

C.1.1 Averaging, number of points, and wait times for relaxation measurements

All T_1 measurements in this work are composed of the average of many repeated sequences as described in Figure 5.1b of Chapter 5. Number of averages, number of points, and the

range of evenly spaced wait times for each figure are given in Table C.1. All error bars shown in this work correspond to one standard deviation.

Figure(s)	Number of Averages	Number of points	Wait time range
5.1c	2×10^5	21	0 - 1 ms
5.1d, S4	2×10^5	31	0 - 1.5 ms
5.2b, S5	1×10^5	21	0 - 2 ms
5.3a	2×10^5	11	0 - 2 ms
5.4b, 5.4d, S6	2×10^5	21	0 - 1.5 ms for $\leq$ 103 K 0 - 0.6 ms for $>$ 103 K

Table C.1: Number of averages, number of measured points, and range of evenly spaced wait times for the T_1 measurements presented in each figure.

C.2 Fabrication and sample characterization

C.2.1 Single-crystal silver deposition and characterization

The single-crystalline silver films were grown using direct current plasma sputtering (AJA International Orion 3)[137, 138]. The sputtering targets used were 99.99% pure silver (Kurt Lesker, Inc). Films were deposited onto prime-grade, degenerately doped (111)-Si wafers (0.0015-0.005 Ω-cm). The substrates were ultrasonically cleaned in acetone, followed by a 2:1 sulfuric acid:hydrogen peroxide solution to eliminate organics. The substrates were then immersed in 49% hydrofluoric acid for 10–15 seconds to remove any native oxide. Next, the substrates were rapidly transferred into the sputtering chamber and the chamber was pumped down to minimize re-oxidation of the surface. Upon reaching a base pressure of about 5×10^{-7} Torr, the substrate was heated to 300 °C and silver was deposited at a rate of 1.5-1.7 nm/s.

Following the growth, multiple characterization techniques were used to test the quality of the deposited films. The crystallinity and surface quality of the films were probed via transmission electron microscopy (TEM) and atomic force microscopy (see Figure C.1).

The TEM scans confirm that the silver films are single-crystal, with lattice fringes apparent from the bulk to the surface. The AFM scans confirm that the films are ultra-smooth with typical root-mean-square roughness of ∼1 nm. Consistent with the TEM scans and electron backscatter diffraction imaging (see below), no grain boundaries were observed within the 10 μm × 10 μm scan region.

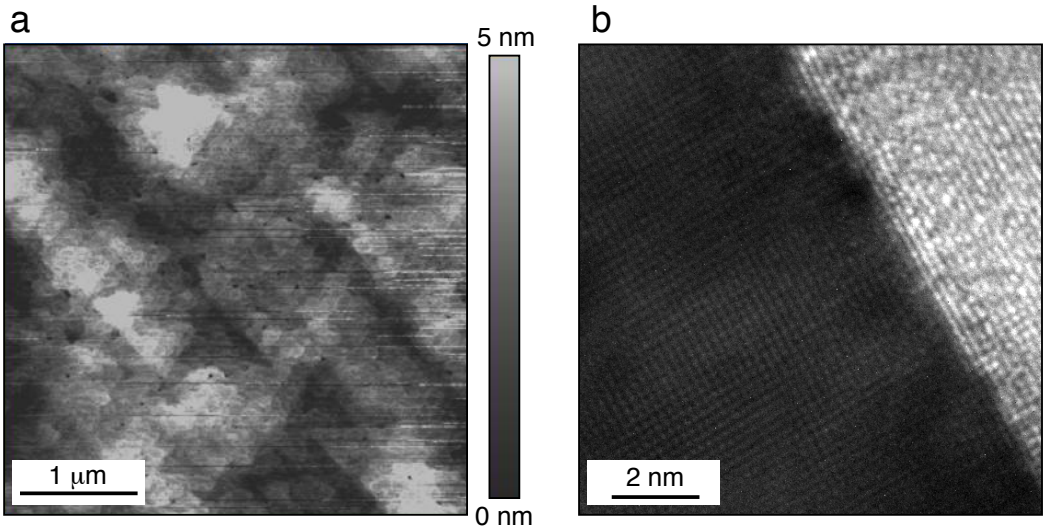

Figure C.1: Single-crystal AFM and TEM characterization. (a) AFM image of a typical single-crystal silver surface grown for this work. The scan indicates a ∼1 nm RMS roughness over a 4 μm × 4 μm range, thus allowing for good diamond-silver contact. (b) A TEM image of a typical silver sample, where the growth direction is from left to right and the silver is capped with a titanium capping layer resulting in the brighter region on the right of the image. The image reveals single-crystallinity of the silver up to the surface.

C.2.2 Characterization of silver film grain size

Crystal orientation and average grain size of the silver samples were measured with electron backscatter diffraction (EBSD). For the polycrystalline films, we use as reference a 100 nm film deposited on 5 nm of SiO_2 on (100) silicon. In the insets of Figures 5.3 and 5.4 of Chapter 5, inverse pole figures of the electron backscatter diffraction data were post-processed to highlight grain boundaries. The areas in white are areas of large noise where

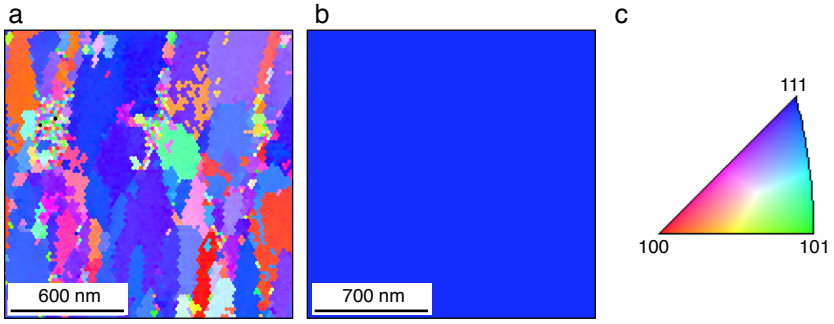

Figure C.2: EBSD characterization of polycrystalline and single-crystal silver. Using electron backscatter diffraction imaging in an SEM, we image the local crystal orientations of our silver films, and measure the average grain size. (a) Data for a 2 μm $\times$ 2 μm area of evaporated silver on 5 nm of SiO_2 on (100) silicon. The crystal variations along the direction perpendicular to the sample can cause mixed diffraction signals, and the crystal orientation fits in those regions have low confidence and result in an IPF with unphysical pixel-to-pixel variations in the crystal orientation (left region of image). (b) EBSD data for the same size region for single-crystal silver. No grain boundaries are visible. (c) Color scale conversion legend to map color to silver crystal orientation.

the the crystal orientation could not be discerned with high confidence, while the other colors indicate different crystal orientations. The inverse pole figures from which those images are derived are given in Figure C.2. EBSD data of the polycrystalline silver film indicated a very granular film, with an average grain diameter of 140 nm and a standard deviation of 80 nm. Grain diameter was approximated by taking the diameter of the circle with the same area as each grain. For the single-crystal films, EBSD data indicated the sample is a single-crystal from nanometer to millimeter length scales, and confirmed a (111) exposed crystal surface for the single-crystal silver, as expected from the growth conditions.

C.2.3 Diamond surface characterization

AFM and profilometer scans were performed on the implantation-side surface of the diamond used for the single-crystal silver measurements, as shown in Figure C.3. The diamond was found to have a local surface roughness of $\sim$ 1 nm RMS over a 10 μm $\times$ 10 μm range,

and to have variations of $\sim$ 10-20 nm peak to peak at the $\sim$100 micron length scale across the entire sample. The NVs sampled from the spatial region over which the diamond was considered to be in contact with the silver were all within a single 40 μm $\times$ 40 μm field of view (see subsection C.5.2 for details.)

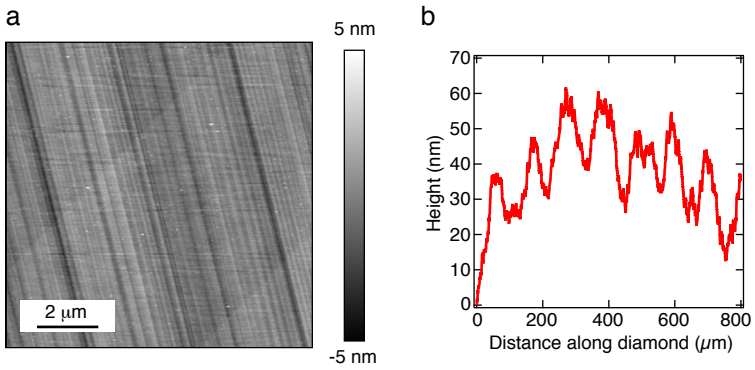

Figure C.3: AFM and profilometer characterization of diamond surface. (a) An AFM image of the surface of the diamond used for the single-crystal silver measurements. The scan indicates a $\sim$1 nm RMS roughness over a 10 μm $\times$ 10 μm range, thus allowing for good diamond-silver contact. (b) A profilometer scan of the surface of the diamond sample.

C.2.4 Spacer layer fabrication for distance dependance studies

Distance-dependence studies of the noise were carried out by growing a spacer layer of SiO_2 between the evaporated silver metal and diamond. A 100-um thick sapphire slide was placed $\sim$300 μm above the surface of a diamond crystal-bonded to a silicon carrier wafer. The anisotropic CVD SiO_2 deposition results in a smooth ramp, as measured by a profilometer (See inset of Figure 5.1b in Chapter 5). A 60 nm film of silver was then deposited on the structure in an electron-beam evaporator. See illustration in Figure 5.4.

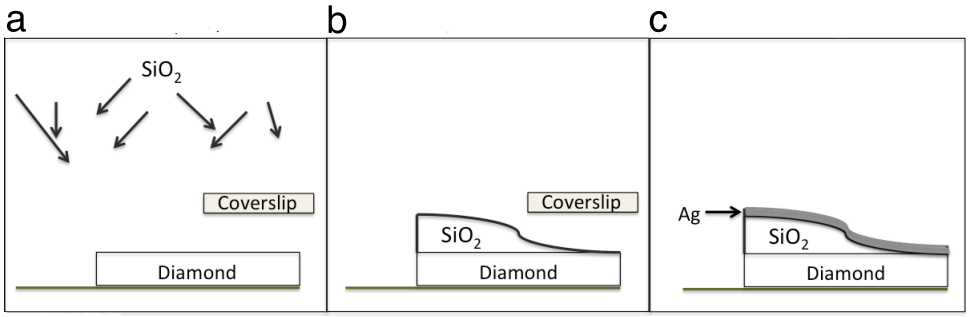

Figure C.4: Silica Ramp Fabrication. (a,b) A silica layer of gradually increasing thickness is fabricated on a diamond sample by placing a raised coverslip (raised $\sim$ 300 um) over the diamond, and growing the silica layer via an anisotropic CVD process. (c) A final 60 nm layer of silver is deposited on the ramp, so that NV centers at different points along the diamond are different distances away from the silver film.

C.2.5 Fabrication of devices for temperature-dependent studies

For the temperature dependence measurements under evaporated polycrystalline silver (Figure 5.3 in Chapter 5), a 5 nm layer of silica was deposited onto the diamond via CVD growth, and a 100 nm layer of silver was then deposited onto the silica film.

In the case of the measurements under single-crystal silver, direct-deposition techniques to create single-crystal silver directly on diamond devices do not presently exist. Instead, the device used in this experiment was fabricated using optical contact bonding between the diamond and the single-crystal silver surfaces. The diamond sample was prepared for bonding by cleaning in a boiling 1:1:1 solution of nitric, sulfuric, and perchloric acids for at least one hour, directly prior to bonding. After growth, the single-crystal silver films were stored with a 50 nm capping layer of alumina to prevent surface oxidation. Directly prior to the bonding process, the alumina capping layer was stripped away in hydrofluoric acid. The diamond was then placed NV side down in contact with the freshly exposed silver surface. A drop of de-ionized water was placed on top of the diamond and allowed to wick in-between the diamond and the silver, and the the diamond was lightly pressed against the silver from above, while the two samples were blow-dried with a nitrogen

spray gun, leaving the diamond bonded directly to the silver surface. This procedure was performed in a cleanroom, with careful attention to the cleanliness of the tweezers and sample holders. Several attempts were required to produce the final device used in this experiment, which demonstrated very robust bonding between the diamond and the silver, and survived multiple thermal cycles from 300-10 K.

C.3 Johnson noise theory

C.3.1 Spin decay rate near a conducting metallic half-space

We derive expressions for the lifetime of a spin interacting with magnetic Johnson Noise outside of a metallic half space following the prescription in [123] and [127].

From Fermi's golden rule and the fluctuation-dissipation theorem, the decay rate from $|m_s = 0\rangle$ to $|m_s = 1\rangle$ for a spin-1 system at a distance z above the surface of a metal at temperature T, with level separation ω and magnetic dipole moment in the ith direction is then given by

$$\Gamma_{0\to1} = \frac{\mu^2}{\hbar^2} \coth\left(\frac{\hbar\omega}{2k_BT}\right) S_B^{ii}(z,\omega) \tag{C.1}$$

where

$$S_B^x(z,\omega) = S_B^y(z,\omega) = \frac{\hbar}{8\pi\epsilon_0 c^3}\mathrm{Re}\int_0^\infty dp \frac{p\left(\omega^2 r^p(p) + (p^2c^2-\omega^2)r^s(p)\right)}{\sqrt{\omega^2-p^2c^2}} e^{2iz\sqrt{\omega^2/c^2-p^2}} \tag{C.2}$$

$$S_B^z(z,\omega) = \frac{\hbar}{4\pi\epsilon_0 c^2}\mathrm{Re}\int_0^\infty dp \frac{p^3}{\sqrt{\omega^2/c^2-p^2}} e^{2iz\sqrt{\omega^2/c^2-p^2}} r^s(p), \tag{C.3}$$

and r^p and r^s denote the Fresnel Coefficients for plane waves incident on the material interface for p and s polarized light, respectively. We choose a coordinate system in which the z axis is perpendicular to the material interface; as $S_B^{\alpha\beta}$ is a diagonal tensor in this

coordinate system, we drop one index and denote the diagonal elements by identifying $S_B^{ii} = S_B^i$. We have also assumed off-diagonal density matrix elements to be 0, $\rho_{ij} = \langle i|\rho|j\rangle = \sum \delta_{ij}$, consistent with T_2^* of the NVs in our experiment being much faster than the population dynamics of system.

C.3.2 Reflection coefficients

Explicitly, the reflection coefficients for a single material boundary are given by

$$\begin{aligned} r^s(p) &= \frac{k_1 - k_2}{k_1 + k_2} \\ r^p(p) &= \frac{\epsilon_2 k_1 - \epsilon_1 k_2}{\epsilon_2 k_1 + \epsilon_1 k_2} \end{aligned} \tag{C.4}$$

with

$$\begin{aligned} k_1 &= \sqrt{\epsilon_1 \omega^2/c^2 - p^2} \\ k_2 &= \sqrt{\epsilon_2 \omega^2/c^2 - p^2} \end{aligned} \tag{C.5}$$

where we have assumed $\mu_i \approx 1$ in all space, consistent with the materials used in this study. In the case of a spin above a metal, the above coefficients are valid when the thickness of the metal greatly exceeds the skin depth or when the spin-metal distance is much less than the thickness. To take into account the finite thickness of the film, the reflection coefficients take the form

$$\begin{aligned} r^s(p) &= \frac{k_1^2 - k_2^2}{k_1^2 + k_2^2 + 2ik_1k_2\cot(k_2a)} \\ r^p(p) &= \frac{\epsilon_2 k_1 - \epsilon_1 k_2}{\epsilon_2 k_1 + \epsilon_1 k_2 + 2i\epsilon_2 k_1 k_2 \cot(k_2 a)}, \end{aligned} \tag{C.6}$$

where a is the thickness of the film [163].

In our experiments with polycrystalline silver, finite thickness effects have a significant

impact on the noise power spectrum outside of the film. The distance and temperature dependence experiments, depicted in Figures 5.2 and 5.3, used films with thicknesses $a = 60$ nm and $a = 100$ nm, respectively. The theoretical predictions shown in Figures 5.2 and 5.3 of Chapter 5 incorporate these finite-thickness corrections. Conversely, in the case of the single-crystal films, which are much thicker ($a = 1.5$ μm), we find that the corrections due to finite thickness are negligible.

Furthermore, in the experiments involving polycrystalline silver, an extra 5 nm layer of SiO_2 lies between the diamond and the metal. Such a geometry can also be accounted for with the appropriate reflection coefficients. However, because $\mu \approx 1$ in diamond and SiO_2, the length scales z and electromagnetic field wave vectors $|\mathbf{k}| = \epsilon\omega/c$ such that $|\mathbf{k}|z \gg 1$, and the electromagnetic response is dominated by $|\epsilon_2| = |\epsilon_{\mathrm{Ag}}| \gg \{|\epsilon_{\mathrm{Diamond}}|, |\epsilon_{\mathrm{SiO2}}|\}$, the effects of the diamond medium and the silica layer are both negligible.

C.3.3 Quasi-static approximation

It is convenient to perform approximations to the integrals in equations (C.2) and (C.3) to gain insight into the decay rate behavior in different regimes. In particular, in the case of a full metallic half space, and in the regime where the electromagnetic wavelength is much larger than the skin depth of the metal, $\lambda \gg \delta$, and the skin depth is much larger than the spin's distance to the metal, $\delta \gg z$,

$$S_B^x(z) = S_B^y(z) \approx \frac{\hbar\omega\sigma}{64\pi\epsilon_0^2 z} \tag{C.7}$$
$$S_B^z(z) \approx 2S_B^x$$

In this regime, known as the quasi-static regime, the decay rate, as described in equation (C.1), is proportional to $1/z$, and thus $T_1 = 1/\Gamma \propto z$.

C.3.4 NV magnetic dipole orientation

We also account for the orientation of the magnetic dipole of our NV centers when calculating the expected decay rate. The decay rate from $|m_s = 0\rangle$ to $|m_s = 1\rangle$ for a spin-1 system with a quantization axis making an angle θ with $\hat{\mathbf{z}}$, the vector normal to the metal surface, in the quasi-static limit is given by

$$\begin{aligned}\gamma_{0\to1} &= \frac{1}{\hbar^2}\coth\left(\frac{\hbar\omega}{2k_BT}\right)\sum g^2\mu_B^2|\langle 1|S_i|0\rangle|^2 S_B^{ii}(z,\omega) \\ &\approx \frac{g^2\mu_B^2}{\hbar^2}\frac{2k_BT}{\hbar\omega}\left(\frac{1}{2}\cos^2(\theta)S_B^x(z,\omega)+\frac{1}{2}S_B^{yy}(z,\omega)+\frac{1}{2}\sin^2(\theta)S_B^z(z,\omega)\right) \\ &\approx \frac{g^2\mu_B^2\mu_0^2 k_BT\sigma}{32\pi z\hbar^2}\left(1+\frac{1}{2}\sin^2(\theta)\right).\end{aligned} \tag{C.8}$$

where in our temperature and frequency range of interest ($T > 4$ K and $\omega < 20$ GHz), $\coth(\hbar\omega/2k_BT) \approx 2k_BT/\hbar\omega$, and we choose our coordinate system such that the spin is always in the $x-z$ plane. All diamond samples used in the experiment are cut such that all four possible NV dipole orientations make the same angle $\theta = \frac{1}{2}(180^\circ - \cos^{-1}(1/3)) \approx 54.9^\circ$ with $\hat{\mathbf{z}}$.

C.3.5 Three-level system dynamics

We also account for the population dynamics of our three level spin-1 coupled to a magnetic noise bath. The rate equations for this system are given by

$$\partial_t\begin{pmatrix}\rho_{00}\\ \rho_{-1-1}\\ \rho_{11}\end{pmatrix} = \begin{pmatrix}-2\gamma & \gamma & \gamma\\ \gamma & -\gamma & 0\\ \gamma & 0 & -\gamma\end{pmatrix}\begin{pmatrix}\rho_{00}\\ \rho_{-1-1}\\ \rho_{11}\end{pmatrix}, \tag{C.9}$$

which, for boundary conditions $\rho_{00}(t=0)=1$, give the solution

$$\rho_{00}(t) = \frac{2}{3}\exp(-3\gamma t) + \frac{1}{3}. \tag{C.10}$$

Thus, the population decay from the $m_s = 0$ state is a factor 3 larger than the rate given by equation (C.8), and we arrive at

$$\Gamma \approx \frac{3\mu^2 g^2 \mu_B^2 k_B T \sigma}{32\pi\hbar^2 z}\left(1+\frac{1}{2}\sin^2\theta\right), \tag{C.11}$$

which is equivalent to equation (2) given in Chapter 5.

C.3.6 Non-local corrections to the decay rate

To take into account the ballistic nature of the electron motion in the silver, we follow [127] and introduce a non-local permittivity. In this regime we find $S_B^z \approx 2S_B^x$ still holds, so for simplicity in the discussion that follows we consider only S_B^z. With the Lindhard form modified for finite electron lifetime, the s polarized reflection coefficient becomes

$$r^s(k_x,k_y) = \frac{\frac{2iqc^2}{\pi\omega^2}\int_0^\infty \frac{d\kappa}{\epsilon_t(k,\omega)-c^2k^2/\omega^2} - 1}{\frac{2iqc^2}{\pi\omega^2}\int_0^\infty \frac{d\kappa}{\epsilon_t(k,\omega)-c^2k^2/\omega^2} + 1}, \tag{C.12}$$

with $k^2 = p^2 + \kappa^2$ and the transverse permittivity defined as

$$\epsilon_t(k,\omega) = 1 - \frac{\omega_p^2}{\omega(\omega+i\nu)} f_t((\omega+i\nu)/kv_f), \tag{C.13}$$

and the function f_t defined as

$$f_t(x) = \frac{3}{2}x^2 - \frac{3}{4}x(x^2-1)\ln\left(\frac{x+1}{x-1}\right), \tag{C.14}$$

and ω_p is the electron plasma frequency, ν is the electron scattering rate, ω is the frequency of radiation, and v_f is the fermi velocity. In the above expressions, the non-locality manifests itself through the k dependence of the permittivity. In order to derive an analytical expression for S_B^z in the limit $z \to 0$, we first rewrite the S_B^z in terms of the rescaled, dimensionless momentum $\tilde{p} = (v_f/\nu)p$ and introduce $\alpha = \frac{\nu}{\omega}\frac{c}{v_f}$:

$$S_B^z = \frac{\hbar}{4\pi\epsilon_0 c^2}\frac{\nu^3}{v_f^3}\mathrm{Re}\int_0^\infty d\tilde{p}\frac{\tilde{p}^3}{\sqrt{1/\alpha^2-\tilde{p}^2}}e^{i\frac{2\nu z}{v_f}\sqrt{1/\alpha^2-\tilde{p}^2}}r^s(\tilde{p}), \tag{C.15}$$

$$r^s(\tilde{p}) = \frac{2i\sqrt{1/\alpha^2-\tilde{p}^2}\int_0^\infty \frac{d\tilde{\kappa}}{\epsilon_t/\alpha^2-\tilde{p}^2-\tilde{\kappa}^2}-\pi}{2i\sqrt{1/\alpha^2-\tilde{p}^2}\int_0^\infty \frac{d\tilde{\kappa}}{\epsilon_t/\alpha^2-\tilde{p}^2-\tilde{\kappa}^2}+\pi}. \tag{C.16}$$

In the regime of our interest $\alpha \sim 10^6$, we can replace $\sqrt{1/\alpha^2-\tilde{p}^2}$ with $i\tilde{p}$ to good approximation. Also, by separating the real and imaginary parts of the numerator and the denominator of equation (C.16), it can be shown that when $\nu/\omega \sim 10^3 \gg 1$, the imaginary part of r^s is well-approximated by

$$\mathrm{Im}\,(r^s) \approx \frac{\tilde{p}}{\pi}\frac{1}{\alpha^2}\int_0^\infty \frac{\mathrm{Im}(\epsilon_t)d\tilde{\kappa}}{\left(\tilde{p}^2+\tilde{\kappa}^2\right)^2}. \tag{C.17}$$

Finally, the substitution of equation (C.17) into equation (C.15) and the change of variables $\tilde{p} = r\cos(\theta)$, and $\tilde{\kappa} = r\sin(\theta)$, and $\tan(\phi) = 1/r$ give us

$$S_B^z = \frac{\hbar}{4\pi^2\epsilon_0 c^4}\frac{\omega_p^2\omega}{v_f}\,C\left(2\nu z/v_f\right) \tag{C.18}$$

where the dimensionless function $C(a)$ is given by

$$C(a) = \int_0^{\pi/2}\int_0^{\pi/2} d\theta d\phi \frac{\cos^3(\theta)e^{-a\frac{\cos(\theta)}{\tan(\phi)}}}{\sin(\phi)\cos^2(\phi)}\frac{3}{2}\left(\frac{\pi/2-\phi}{\cos(\phi)}-\sin(\phi)\right). \tag{C.19}$$

The function $C(a)$ has a logarithmic divergence $C(a) \approx -\frac{\pi}{2}\ln(a)$ in the limit $a \to 0$. This originates from integration over infinitely large momentum p in the integral in equa-

tion (C.3). Therefore, we introduce a physical cut-off, which modifies the range of integration for ϕ from $[0, \pi/2]$ to $[\phi_c, \pi/2]$ with $\tan(\phi_c) \equiv \frac{\nu}{v_f k_{\text{cut}}}$. Using $k_{\text{cut}} = 2\pi/a_{\text{Ag}}$ with $a_{\text{Ag}} = 0.4$ nm, the lattice spacing of silver, we obtain well-defined behavior in the limit $z \to 0$, $C_{\text{cut}}(2\nu z/v_f) \approx 4.6\pi$, which leads to equation (3) in Chapter 5.

C.4 Spectral dependance of Johnson noise

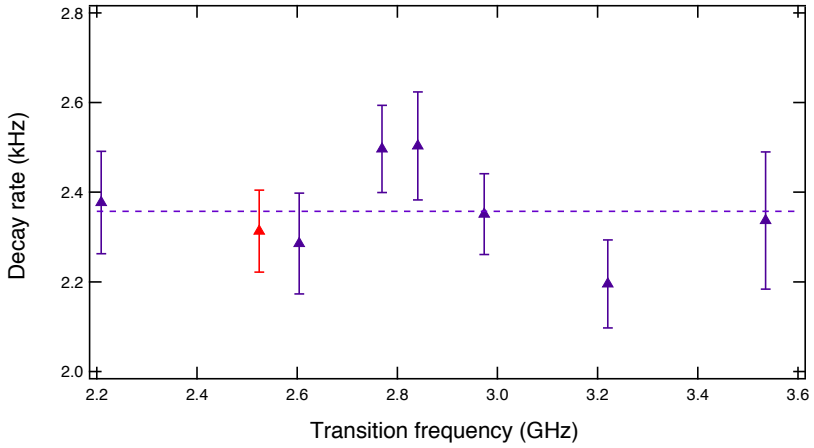

Figure C.5: Spectral dependence of NV relaxation rates close to silver. We apply static magnetic fields to shift the NV spin transition frequencies. When polarized in the $|\pm 1\rangle$ state, the relaxation rate of the NV center is sensitive to the magnetic field noise at the frequency $\omega_\pm$ given by Eq. S26. The red triangle corresponds to the decay rate extracted from the data shown in Figure 5.1d of Chapter 5.

From equation (C.11), it is clear that we expect the noise spectrum of magnetic Johnson noise to be white for frequencies over which $\coth(\hbar\omega/2k_BT) \approx 2k_BT/\hbar\omega$. We verify this by applying an external magnetic field, $B_{||}$, along the NV axis to tune the NV spin transition frequencies

$$\omega_\pm = \Delta \pm 2g\mu_B B_{||}/\hbar \tag{C.20}$$

where $\omega_\pm$ denotes the transition frequency from the $|m_s = 0\rangle$ to the $|m_s = \pm 1\rangle$ states, Δ denotes the NV spin ground state zero-field splitting ($2\pi \times 2.88$ GHz), and $g\mu_B$ is the NV

electronic spin magnetic moment. We measure the relaxation rate when the NV is polarized in the $|0\rangle$ state, and when it is polarized in the $|\pm 1\rangle$ states. Based on the rate equations given in section 1.2 (equation (C.9)), the population relaxation from the $|0\rangle$ state is given by equation (16), while the population relaxation from the $|\pm 1\rangle$ state should the following form:

$$\rho_{\pm 1 \pm 1}(t) = \frac{1}{6}e^{-3\gamma t} + \frac{1}{2}e^{-\gamma t} + \frac{1}{3}. \tag{C.21}$$

We observe excellent agreement with these predictions, and simultaneously fit to the relaxation from the $|0\rangle$ and $|\pm 1\rangle$ states with only a single decay rate γ. The extracted rates γ at different magnetic fields, and therefore different NV transition frequencies, are shown in Figure C.5. We find good agreement with the hypothesis of a white noise bath, with $\chi^2/N = .87$, for the $\omega = 2\pi \times 2.2 - 3.6$ GHz range.

C.5 NV T_1 statistics

For NVs implanted at shallow depth, we occasionally observe short NV T_1 times for NVs under bare diamond (see Table C.2). The origin of the fast decay for some NVs is unclear. No spatial correlations in T_1 are observed for the NVs with reduced T_1 times.

Number of NVs	T_1
13	$\geq$ 2 ms
1	1.2 ms
1	500 μs
1	300 μs

Table C.2: T_1 statistics for 16 of the NVs shown in Figure 5.4 of Chapter 5 (corresponding to the blue triangles in Figure C.7d), in the absence of silver.

C.5.1 Extraction of relaxation rates and distances under polycrystalline silver ramp

As we would expect due to the variability in NV T_1 times under bare diamond, when measuring under silver we observe a spread in the T_1 times of the NVs, as shown in Figure 5, especially at larger distances from the silver, consistent with the variation we observe on bare diamond. This is because the Johnson noise only sets an upper limit on the NV spin lifetime, and other local sources of noise can still reduce it further. To compensate for this we measured 5-10 NVs at each point along the ramp, such that we can expect the maximum T_1 observed in at each point to be Johnson noise limited (10 NVs per points were measured for the 7 closest points measured from 20-80 nm, and 5 NVs per points for the other 7 points, from 100-200 nm). We then only include NVs with a spin-dependent fluorescence contrast within the expected range of 15-35%. The result is plotted in Figure C.6. The data plotted in Figure 5.2 in Chapter 5 is the inverse of the maximum T_1 measured at each point along the ramp (the red data points in Figure C.6.)

When estimating the distance to the film for the NVs plotted in Figure 5.2 in Chapter 5, the largest source of error is the variation in depth below the surface of the implanted NVs. As a result, we must also account for the statistical bias in NV depth introduced by selecting the maximum T_1 in each region. In particular, as most NVs have Johnson noise limited lifetimes, by taking the maximum T_1 measured we are likely selecting for the deepest NV in each region. To account for this, we assume the NV implantation depths are normally distributed, with a mean depth μ=15 nm and a standard deviation σ=10 nm [164]. Let $N_{\mu,\sigma}(x)$ denote the normal distribution representing the NV depth profile. If n NVs are randomly selected from this distribution, it can be shown that the probability the deepest NV selected has depth x is given by

$$P_{max}(x) = n\left(\int_{-\infty}^{x} N_{\mu,\sigma}(x')dx'\right)^{n-1} N_{\mu,\sigma}(x). \tag{C.22}$$

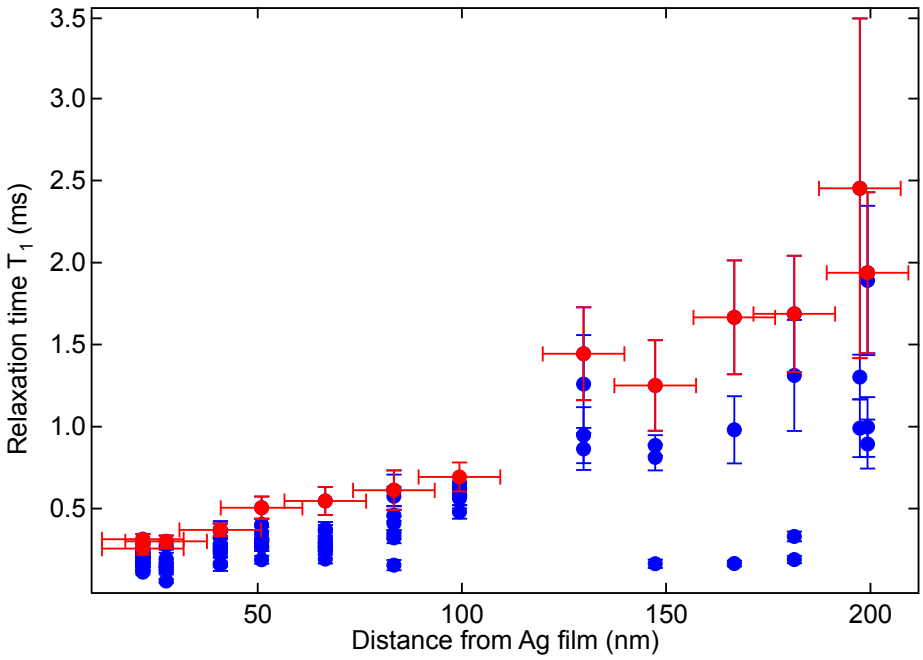

Figure C.6: T_1 distance dependence close to silver film, raw data. We vary the distance from NVs to the silver surface via a gradual silica ramp (∼15-200 nm over ∼1.5 mm), and plot the measured NV T_1 times as a function of distance to the film in each region. The maxima, corresponding to the data shown in Figure 5.2b of Chapter 5, are plotted in red, and data from all other measured NVs is plotted in blue.

We use this new distribution to determine the expected value and standard deviation of the depth of the NV selected at each point along the ramp. For example, if we measured $n = 5$ NVs at one point along the ramp, from the above probability distribution function P_{max} we find that the expected value for the depth of the deepest NV measured is 27 nm with a standard deviation of 7 nm, while at a point where we measured $n = 10$ NVs the distribution of depths is 30 ± 6 nm. These depths are then added to thickness of the ramp at that point to give the total distance to the silver surface plotted in Figure 5.2 of Chapter 5.

C.5.2 NVs under single crystal silver

In total, we measured the T_1 of 25 NVs close to the single crystal silver sample at 12 temperatures, in three different spatial regions on the sample. Of these NVs, 16 were in

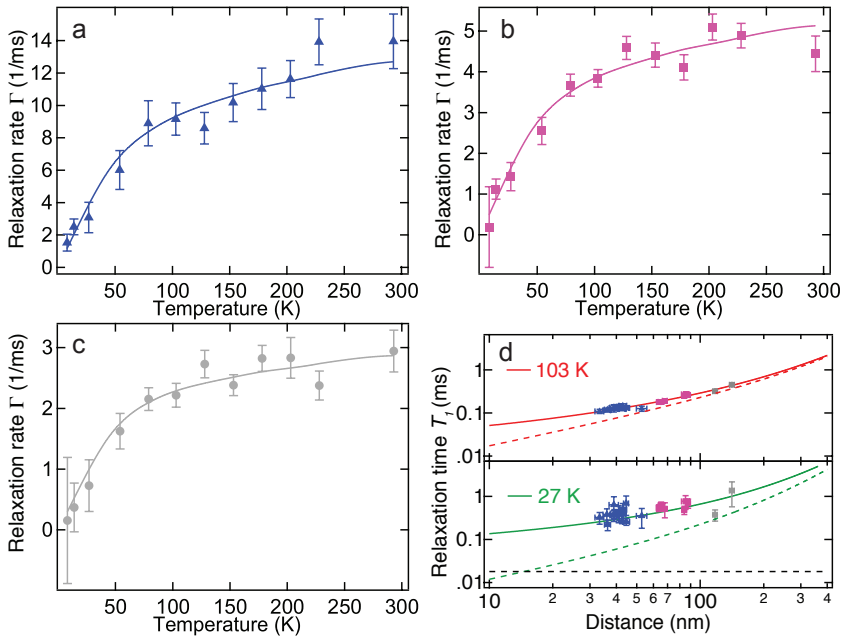

Figure C.7: NV decay rates near single-crystal silver with non-local fits. (a) Data for an NV in the same region as the NV in Figure 5.4b of Chapter 5, region A. The extracted distance from the fit is $z = 33.3 \pm 1.6$ nm. This was the smallest extracted distance we observed for the single-crystal silver measurements. (b) Data for an NV in region B, where we expect NVs to be farther away from the silver film than in region A. The extracted distance from the fit is $z = 88 \pm 2$ nm (c) Data for an NV in region C, where we expect the largest separation between the NV and the metal film. The extracted distance is $z = 141 \pm 4$ nm. (d) The same data as in Figure 5.4d of Chapter 5, measured T_1 versus extracted distance for two temperatures, 103 K (top) and 27 K (bottom), color coded by sample region (blue triangles in region A, pink squares in region B, gray circles in region C).

region A (blue triangles in Figure C.7d), where the diamond surface was observed to be in contact with the silver, 7 were in region B where a gap was expected to be growing between the diamond and the silver (pink squares in Figure C.7d), and 2 were in region C, where the gap was expected to be fairly large (gray circles in Figure C.7d).

The gap between the diamond and silver was qualitatively apparent based on a number of separate observations. We observed a variation in the brightness of the NVs in the different regions when exposed to the same laser power at the objective, which we attribute primarily to optical interference coming from the reflections off the silver and diamond

Region	Mean excited state lifetime
A	8.2 ns
B	12.5 ns
C	13.6 ns

Table C.3: Mean optical excited state lifetimes by spatial region for the NVs show in Figure 5.4 of Chapter 5 and Figure C.7d.

surfaces. In addition, we measured reduced NV optical excited state lifetimes in region A (the region in contact with silver,) which we attribute to quenching from the silver (see Table C.3). We also observed an accumulation of a small amount of fluorescent background on the diamond surface over time in regions B and C, which was absent from region A, as would be expected if the diamond and silver were in direct contact there.

The T_1 time at room temperature of all the NVs was also subsequently measured after the silver sample was removed. Of these NVs, one NV in region A was rejected because the measured T_1s under silver were not repeatable, and one NV in region B was rejected because it had very short T_1 times even at low temperatures ($<$300 μs at 8 K,) leaving 23 NVs that compose the dataset shown in Figure 5.4d of Chapter 5. The anomalous behavior of the two rejected NVs is not well understood, and could be the subject of further study.

References

[1] L. S. Brown and G. Gabrielse, *Reviews of Modern Physics* **58**, 233 (1986).

[2] J. Ye, D. W. Vernooy, and H. J. Kimble, *Physical Review Letters* **83**, 4987 (1999).

[3] J. Raimond, M. Brune, and S. Haroche, *Reviews of Modern Physics* **73**, 565 (2001).

[4] W. S. Bakr, A. Peng, M. E. Tai, R. Ma, J. Simon, J. I. Gillen, S. Fölling, L. Pollet, and M. Greiner, *Science* **329**, 547 (2010).

[5] D. Leibfried, R. Blatt, C. Monroe, and D. Wineland, *Reviews of Modern Physics* **75**, 281 (2003).

[6] W. E. Moerner, *The Journal of Physical Chemistry B* **106**, 910 (2002).

[7] A. Yacoby, M. Heiblum, D. Mahalu, and H. Shtrikman, *Physical Review Letters* **74**, 4047 (1995).

[8] A. Imamoğlu, D. D. Awschalom, G. Burkard, D. P. DiVincenzo, D. Loss, M. Sherwin, and A. Small, *Physical Review Letters* **83**, 4204 (1999).

[9] J. M. Martinis, S. Nam, J. Aumentado, and C. Urbina, *Physical Review Letters* **89**, 117901 (2002).

[10] A. Wallraff, D. I. Schuster, A. Blais, L. Frunzio, R. S. Huang, J. Majer, S. Kumar, S. M. Girvin, and R. J. Schoelkopf, *Nature* **431**, 162 (2004).

[11] F. Jelezko, T. Gaebel, I. Popa, A. Gruber, and J. Wrachtrup, *Physical Review Letters* **92**, 076401 (2004).

[12] L. Childress, M. Gurudev Dutt, J. Taylor, A. Zibrov, F. Jelezko, J. Wachtrup, P. Hemmer, and M. Lukin, *Science* **314**, 281 (2006).

[13] B. Odom, D. Hanneke, B. d'Urso, and G. Gabrielse, *Physical Review Letters* **97**, 030801 (2006).

[14] R. Pohl, A. Antognini, F. Nez, F. D. Amaro, F. Biraben, J. M. R. Cardoso, D. S. Covita, A. Dax, S. Dhawan, L. M. P. Fernandes, et al., *Nature* **466**, 213 (2010).

[15] T. A. Collaboration, J. Baron, W. C. Campbell, D. DeMille, J. M. Doyle, G. Gabrielse, Y. V. Gurevich, P. W. Hess, N. R. Hutzler, E. Kirilov, et al., *Science* **343**, 269 (2014).

[16] T. Udem, R. Holzwarth, and T. W. Hansch, *Nature* **416**, 233 (2002).

[17] T. Steinmetz, T. Wilken, C. Araujo-Hauck, R. Holzwarth, T. W. Hänsch, L. Pasquini, A. Manescau, S. D'Odorico, M. T. Murphy, T. Kentischer, et al., *Science* **321**, 1335 (2008).

[18] G. Binnig and H. Rohrer, *IBM Journal of research and development* **44**, 279 (2000).

[19] J. Clarke and A. I. Braginski, *The SQUID handbook* (Wiley Online Library, 2006).

[20] R. P. Feynman, *International journal of theoretical physics* **21**, 467 (1982).

[21] S. Lloyd, *Science* **273**, 1073 (1996).

[22] P. W. Shor, *SIAM journal on computing* **26**, 1484 (1997).

[23] P. W. Shor and J. Preskill, *Physical Review Letters* **85**, 441 (2000).

[24] K. Kim, M. S. Chang, S. Korenblit, R. Islam, E. E. Edwards, J. K. Freericks, G. D. Lin, L. M. Duan, and C. Monroe, *Nature* **465**, 590 (2010).

[25] B. P. Lanyon, C. Hempel, D. Nigg, M. Müller, R. Gerritsma, F. Zähringer, P. Schindler, J. T. Barreiro, M. Rambach, G. Kirchmair, et al., *Science* **334**, 57 (2011).

[26] J. Simon, W. S. Bakr, R. Ma, M. E. Tai, P. M. Preiss, and M. Greiner, *Nature* **472**, 307 (2011).

[27] I. Bloch, J. Dalibard, and S. Nascimbene, *Nature Physics* **8**, 267 (2012).

[28] L. K. Grover, *Physical Review Letters* **79**, 325 (1997).

[29] J. A. Jones, M. Mosca, and R. H. Hansen, *Nature* **393**, 344 (1998).

[30] L. M. K. Vandersypen, M. Steffen, G. Breyta, C. S. Yannoni, M. H. Sherwood, and I. L. Chuang, *Nature* **414**, 883 (2001).

[31] B. P. Lanyon, T. J. Weinhold, N. K. Langford, M. Barbieri, D. F. V. James, A. Gilchrist, and A. G. White, *Physical Review Letters* **99**, 250505 (2007).

[32] L. DiCarlo, J. M. Chow, J. M. Gambetta, L. S. Bishop, B. R. Johnson, D. I. Schuster, J. Majer, A. Blais, L. Frunzio, S. M. Girvin, et al., *Nature* **460**, 240 (2009).

[33] H. Briegel, W. Dür, J. I. Cirac, and P. Zoller, *Physical Review Letters* **81**, 5932 (1998).

[34] L. M. Duan, M. D. Lukin, J. I. Cirac, and P. Zoller, *Nature* **414**, 413 (2001).

[35] B. J. Bloom, T. L. Nicholson, J. R. Williams, S. L. Campbell, M. Bishof, X. Zhang, W. Zhang, S. L. Bromley, and J. Ye, *Nature* **506**, 71 (2014).

[36] D. Budker and M. Romalis, *Nature Physics* **3**, 227 (2007).

[37] J. Taylor, P. Cappellaro, L. Childress, L. Jiang, D. Budker, P. Hemmer, A. Yacoby, R. Walsworth, and M. Lukin, *Nature Physics* **4**, 810 (2008).

[38] J. Maze, P. Stanwix, J. Hodges, S. Hong, J. Taylor, P. Cappellaro, L. Jiang, M. Dutt, E. Togan, A. Zibrov, et al., *Nature* **455**, 644 (2008).

[39] M. Kasevich and S. Chu, *Physical Review Letters* **67**, 181 (1991).

[40] T. L. Gustavson, P. Bouyer, and M. A. Kasevich, *Physical Review Letters* **78**, 2046 (1997).

[41] D. J. Wineland, J. J. Bollinger, W. M. Itano, F. L. Moore, and D. J. Heinzen, *Physical Review A* **46**, R6797 (1992).

[42] I. D. Leroux, M. H. Schleier-Smith, and V. Vuletić, *Physical Review Letters* **104**, 073602 (2010).

[43] J. G. Bohnet, K. C. Cox, M. A. Norcia, J. M. Weiner, Z. Chen, and J. K. Thompson, *Nature Photonics* **8**, 731 (2014).

[44] S. Bennett, N. Yao, J. Otterbach, P. Zoller, P. Rabl, and M. Lukin, *Physical Review Letters* **110**, 156402 (2013).

[45] E. Kessler, P. Komar, M. Bishof, L. Jiang, A. Sorensen, J. Ye, and M. Lukin, *Physical Review Letters* **112**, 190403 (2014).

[46] C. Langer, R. Ozeri, J. D. Jost, J. Chiaverini, B. DeMarco, A. Ben-Kish, R. B. Blakestad, J. Britton, D. B. Hume, W. M. Itano, et al., *Physical Review Letters* **95**, 060502 (2005).

[47] R. Blatt and D. Wineland, *Nature* **453**, 1008 (2008).

[48] D. L. Moehring, P. Maunz, S. Olmschenk, K. C. Younge, D. N. Matsukevich, L. M. Duan, and C. Monroe, *Nature* **449**, 68 (2007).

[49] S. Ritter, C. Nolleke, C. Hahn, A. Reiserer, A. Neuzner, M. Uphoff, M. Mucke, E. Figueroa, J. Bochmann, and G. Rempe, *Nature* **484**, 195 (2012).

[50] Y. Lin, I. Teper, C. Chin, and V. Vuletic, *Physical Review Letters* **92**, 050404 (2004).

[51] J. D. Thompson, T. G. Tiecke, N. P. de Leon, J. Feist, A. V. Akimov, M. Gullans, A. S. Zibrov, V. Vuletić, and M. D. Lukin, *Science* **340**, 1202 (2013).

[52] J. D. Joannopoulos, S. G. Johnson, J. N. Winn, and R. D. Meade, *Photonic crystals: molding the flow of light* (Princeton University Press, 2011).

[53] D. Hunger, S. Camerer, T. Hansch, D. König, J. Kotthaus, J. Reichel, and P. Treutlein, *Physical Review Letters* **104**, 143002 (2010).

[54] S. Wildermuth, S. Hofferberth, I. Lesanovsky, E. Haller, L. M. Andersson, S. Groth, I. Bar-Joseph, P. Kruger, and J. Schmiedmayer, *Nature* **435**, 440 (2005).

[55] J. Meijer, B. Burchard, M. Domhan, C. Wittmann, T. Gaebel, I. Popa, F. Jelezko, and J. Wrachtrup, *Applied Physics Letters* **87**, 261909 (2005).

[56] D. M. Toyli, C. D. Weis, G. D. Fuchs, T. Schenkel, and D. D. Awschalom, *Nano Letters* **10**, 3168 (2010).

[57] K. Ohno, F. Joseph Heremans, L. C. Bassett, B. A. Myers, D. M. Toyli, A. C. Bleszynski Jayich, C. J. Palmstrøm, and D. D. Awschalom, *Applied Physics Letters* **101**, 082413 (2012).

[58] P. L. Stanwix, L. M. Pham, J. R. Maze, D. Le Sage, T. K. Yeung, P. Cappellaro, P. R. Hemmer, A. Yacoby, M. D. Lukin, and R. L. Walsworth, *Physical Review B* **82**, 201201 (2010).

[59] G. Balasubramanian, P. Neumann, D. Twitchen, M. Markham, R. Kolesov, N. Mizuochi, J. Isoya, J. Achard, J. Beck, J. Tissler, et al., *Nature Materials* **8**, 383 (2009).

[60] P. C. Maurer, G. Kucsko, C. Latta, L. Jiang, N. Y. Yao, S. D. Bennett, F. Pastawski, D. Hunger, N. Chisholm, M. Markham, et al., *Science* **336**, 1283 (2012).

[61] A. Sipahigil, M. L. Goldman, E. Togan, Y. Chu, M. Markham, D. J. Twitchen, A. S. Zibrov, A. Kubanek, and M. D. Lukin, *Physical Review Letters* **108**, 143601 (2012).

[62] E. Togan, Y. Chu, A. S. Trifonov, L. Jiang, J. Maze, L. Childress, M. V. G. Dutt, A. S. Sorensen, P. R. Hemmer, A. S. Zibrov, et al., *Nature* **466**, 730 (2010).

[63] G. Balasubramanian, I. Y. Chan, R. Kolesov, M. Al-Hmoud, J. Tisler, C. Shin, C. Kim, A. Wojcik, P. R. Hemmer, A. Krueger, et al., *Nature* **455**, 648 (2008).

[64] L. M. Pham, D. L. Sage, P. L. Stanwix, T. K. Yeung, D. Glenn, A. Trifonov, P. Cappellaro, P. R. Hemmer, M. D. Lukin, H. Park, et al., *New Journal of Physics* **13**, 045021 (2011).

[65] P. Maletinsky, S. Hong, M. S. Grinolds, B. Hausmann, M. D. Lukin, R. L. Walsworth, M. Loncar, and A. Yacoby, *Nature Nanotechnology* **7**, 320 (2012).

[66] D. Le Sage, K. Arai, D. R. Glenn, S. J. DeVience, L. M. Pham, L. Rahn-Lee, M. D. Lukin, A. Yacoby, A. Komeili, and R. L. Walsworth, *Nature* **496**, 486 (2013).

[67] M. S. Grinolds, S. Hong, P. Maletinsky, L. Luan, M. D. Lukin, R. L. Walsworth, and A. Yacoby, *Nature Physics* **9**, 215 (2013).

[68] F. Dolde, H. Fedder, M. W. Doherty, T. Nobauer, F. Rempp, G. Balasubramanian, T. Wolf, F. Reinhard, L. C. L. Hollenberg, F. Jelezko, et al., *Nature Physics* **7**, 459 (2011).

[69] V. Acosta, E. Bauch, M. Ledbetter, A. Waxman, L.-S. Bouchard, and D. Budker, *Physical review letters* **104**, 070801 (2010).

[70] G. Kucsko, P. C. Maurer, N. Y. Yao, M. Kubo, H. J. Noh, P. K. Lo, H. Park, and M. D. Lukin, *Nature* **500**, 54 (2013).

[71] P. Ovartchaiyapong, K. W. Lee, B. A. Myers, and A. C. B. Jayich, *Nature communications* **5** (2014).

[72] J. Tisler, G. Balasubramanian, B. Naydenov, R. Kolesov, B. Grotz, R. Reuter, J.-P. Boudou, P. A. Curmi, M. Sennour, A. Thorel, et al., *ACS Nano* **3**, 1959 (2009).

[73] C. L. Degen, *Applied Physics Letters* **92**, 243111 (2008).

[74] M. W. Doherty, N. B. Manson, P. Delaney, F. Jelezko, J. Wrachtrup, and L. C. Hollenberg, *Physics Reports* **528**, 1 (2013).

[75] A. Jarmola, V. M. Acosta, K. Jensen, S. Chemerisov, and D. Budker, *Physical Review Letters* **108**, 197601 (2012).

[76] M. Scully and M. Zubairy, *Quantum Optics* (Cambridge Univ. Press, 1997).

[77] G. de Lange, Z. Wang, D. Ristè, V. Dobrovitski, and R. Hanson, *Science* **330**, 60 (2010).

[78] J. Du, X. Rong, N. Zhao, Y. Wang, J. Yang, and R. Liu, *Nature* **461**, 1265 (2009).

[79] B. Naydenov, F. Dolde, L. T. Hall, C. Shin, H. Fedder, L. C. L. Hollenberg, F. Jelezko, and J. Wrachtrup, *Physical Review B* **83**, 081201 (2011).

[80] N. Bar-Gill, L. M. Pham, A. Jarmola, D. Budker, and R. L. Walsworth, *Nature Communications* **4**, 1743 (2013).

[81] S. Haroche and J. Raimond, *Exploring the Quantum: Atoms, Cavities, and Photons* (Oxford Univ. Press, 2006).

[82] R. Schoelkopf and S. Girvin, *Nature* **451**, 664 (2008).

[83] P. Rabl, P. Cappellaro, M. Dutt, L. Jiang, J. Maze, and M. Lukin, *Physical Review B* **79**, 041302 (2009).

[84] P. Treutlein, D. Hunger, S. Camerer, T. Hänsch, and J. Reichel, *Physical Review Letters* **99**, 140403 (2007).

[85] F. Xue, L. Zhong, Y. Li, and C. P. Sun, *Physical Review B* **75**, 033407 (2007).

[86] I. Bargatin and M. L. Roukes, *Physical Review Letters* **91**, 138302 (2003).

[87] T. Kippenberg and K. Valhala, *Science* **321**, 1172 (2008).

[88] G. A. Steele, A. K. Hüttel, B. Witkamp, M. Poot, H. B. Meerwaldt, L. P. Kouwenhoven, and H. S. J. van der Zant, *Science* **325**, 1103 (2009).

[89] A. O'Connell, M. Hofheinz, M. Ansmann, R. Bialczak, M. Lenander, E. Lucero, M. Neeley, D. Sank, H. Wang, M. Weides, et al., *Nature* **464**, 697 (2010).

[90] J. Teufel, T. Donner, D. Li, J. Harlow, M. Allman, K. Cicak, A. Sirois, J. Whittaker, K. Lehnert, and R. Simmonds, *Nature* **475**, 359 (2011).

[91] J. Chan, T. P. M. Alegre, A. H. Safavi-Naeini, J. T. Hill, A. Krause, S. Groblacher, M. Aspelmeyer, and O. Painter, *Nature* **478**, 89 (2011).

[92] M. LaHaye, J. Suh, P. Echternach, K. Schwab, and M. Roukes, *Nature* **459**, 960 (2009).

[93] O. Arcizet, V. Jacques, A. Siria, P. Poncharal, P. Vincent, and S. Seidelin, *Nature Physics* **7**, 879 (2011).

[94] D. Rugar, R. Budakian, H. Mamin, and B. Chui, *Nature* **430**, 329 (2004).

[95] P. Rabl, S. Kolkowitz, F. Koppens, J. Harris, P. Zoller, and M. Lukin, *Nature Physics* **6**, 602 (2010).

[96] M. Grinolds, P. Maletinsky, S. Hong, M. Lukin, R. Walsworth, and A. Yacoby, *Nature Physics* **7**, 687 (2011).

[97] S. Kotler, N. Akerman, Y. Glickman, A. Keselman, and R. Ozeri, *Nature* **473**, 61 (2011).

[98] H. Mamin, T. Stowe, T. Kenny, and D. Rugar, *Physical Review Letters* **86**, 2874 (2001).

[99] S. Verbridge, H. Craighead, and M. Jeevak, *Applied Physics Letters* **92**, 013112 (2008).

[100] L. Robledo, L. Childress, H. Bernien, B. Hensen, P. F. A. Alkemade, and R. Hanson, *Nature* **477**, 574 (2011).

[101] C. Degen, M. Poggio, H. Mamin, C. Rettner, and D. Rugar, *Proceedings of the National Academy of Sciences* **106**, 1313 (2009).

[102] P. C. Hammel and D. V. Pelekhov, *Handbook of Magnetism and Advanced Magnetic Materials* (Wiley, New York, 2007), vol. 5, chap. 4.

[103] F. Jelezko, T. Gaebel, I. Popa, M. Domhan, A. Gruber, and J. Wrachtrup, *Physical Review Letters* **93**, 130501 (2004).

[104] R. Hanson, V. V. Dobrovitski, A. E. Feiguin, O. Gywat, and D. D. Awschalom, *Science* **320**, 352 (2008).

[105] M. V. G. Dutt, L. Childress, L. Jiang, E. Togan, J. Maze, F. Jelezko, A. S. Zibrov, P. R. Hemmer, and M. D. Lukin, *Science* **316**, 1312 (2007).

[106] L. Jiang, J. S. Hodges, J. R. Maze, P. Maurer, J. M. Taylor, D. G. Cory, P. R. Hemmer, R. L. Walsworth, A. Yacoby, A. S. Zibrov, et al., *Science* **326**, 267 (2009).

[107] T. van der Sar, Z. H. Wang, M. S. Blok, H. Bernien, T. H. Taminiau, D. M. Toyli, D. A. Lidar, D. D. Awschalom, R. Hanson, and V. V. Dobrovitski, *Nature* **484**, 82 (2012).

[108] P. Neumann, J. Beck, M. Steiner, F. Rempp, H. Fedder, P. R. Hemmer, J. Wrachtrup, and F. Jelezko, *Science* **329**, 542 (2010).

[109] L. T. Hall, C. D. Hill, J. H. Cole, and L. C. L. Hollenberg, *Physical Review B* **82**, 045208 (2010).

[110] G. de Lange, D. Riste, V. V. Dobrovitski, and R. Hanson, *Physical Review Letters* **106**, 80802 (2011).

[111] C. A. Ryan, J. S. Hodges, and D. G. Cory, *Physical Review Letters* **105**, 1 (2010).

[112] Z.-H. Wang, G. de Lange, D. Ristè, R. Hanson, and V. V. Dobrovitski, *Physical Review B* **85**, 155204 (2012).

[113] A. Gali, M. Fyta, and E. Kaxiras, *Physical Review B* **77**, 1 (2008).

[114] A. Gali, *Physical Review B* **80**, 241204 (2009).

[115] B. Smeltzer, L. Childress, and A. Gali, *New Journal of Physics* **13**, 025021 (2011).

[116] A. Dréau, J.-R. Maze, M. Lesik, J.-F. Roch, and V. Jacques, *Physical Review B* **85**, 134107 (2012).

[117] N. Zhao, J. L. Hu, S. W. Ho, J. T. K. Wan, and R. B. Liu, *Nature Nanotechnology* **6**, 242 (2011).

[118] M. Lundstrom, *Science* **299**, 210 (2003).

[119] B. Weber, S. Mahapatra, H. Ryu, S. Lee, A. Fuhrer, T. C. G. Reusch, D. L. Thompson, W. C. T. Lee, G. Klimeck, L. C. L. Hollenberg, et al., *Science* **335**, 64 (2012).

[120] Q. Xu, B. Schmidt, S. Pradhan, and M. Lipson, *Nature* **435**, 325 (2005).

[121] L. Novotny and B. Hecht, *Principles of nano-optics* (Cambridge university press, 2012).

[122] A. L. Falk, F. H. L. Koppens, C. L. Yu, K. Kang, N. de Leon Snapp, A. V. Akimov, M.-H. Jo, M. D. Lukin, and H. Park, *Nature Physics* **5**, 475 (2009).

[123] C. Henkel, S. Pötting, and M. Wilkens, *Applied Physics B* **69**, 379 (1999).

[124] M. P. A. Jones, C. J. Vale, D. Sahagun, B. V. Hall, and E. A. Hinds, *Physical Review Letters* **91**, 080401 (2003).

[125] D. Harber, J. McGuirk, J. Obrecht, and E. Cornell, *Journal of Low Temperature Physics* **133**, 229 (2003).

[126] M. Brownnutt, M. Kumph, P. Rabl, and R. Blatt, *Ion-trap measurements of electric-field noise near surfaces*, arXiv:1409.6572 (2014).

[127] L. S. Langsjoen, A. Poudel, M. G. Vavilov, and R. Joynt, *Physical Review A* **86**, 010301 (2012).

[128] C. Beenakker and H. van Houten, *Solid state physics* **44**, 228 (1991).

[129] S. Datta, *Electronic transport in mesoscopic systems* (Cambridge university press, 1997).

[130] A. C. Bleszynski-Jayich, W. E. Shanks, B. Peaudecerf, E. Ginossar, F. von Oppen, L. Glazman, and J. G. E. Harris, *Science* **326**, 272 (2009).

[131] H. Bluhm, N. C. Koshnick, J. A. Bert, M. E. Huber, and K. A. Moler, *Physical Review Letters* **102**, 136802 (2009).

[132] D. Rothfuß, A. Reiser, A. Fleischmann, and C. Enss, *Applied Physics Letters* **103**, 052605 (2013).

[133] J. Tetienne, T. Hingant, J. Kim, L. H. Diez, J.-P. Adam, K. Garcia, J.-F. Roch, S. Rohart, A. Thiaville, D. Ravelosona, et al., *Science* **344**, 1366 (2014).

[134] E. Schäfer-Nolte, L. Schlipf, M. Ternes, F. Reinhard, K. Kern, and J. Wrachtrup, *Tracking Temperature Dependent Relaxation Times of Individual Ferritin Nanomagnets with a Wide-band Quantum Spectrometer*, arXiv:1406.0362 (2014).

[135] M. Pelliccione, B. A. Myers, L. Pascal, A. Das, and A. C. Bleszynski Jayich, *Two-dimensional nanoscale imaging of gadolinium spins via scanning probe relaxometry with a single spin in diamond*, arXiv:1409.2422 (2014).

[136] T. H. Taminiau, J. Cramer, T. van der Sar, V. V. Dobrovitski, and R. Hanson, *Nature Nanotechnology* **9**, 171 (2014).

[137] A. A. Baski and H. Fuchs, *Surface Science* **313**, 275 (1994).

[138] J. H. Park, P. Ambwani, M. Manno, N. C. Lindquist, P. Nagpal, S. H. Oh, C. Leighton, and D. Norris, *Advanced Materials* **24**, 3988 (2012).

[139] G. W. Ford and W. Weber, *Physics Reports* **113**, 195 (1984).

[140] N. W. Ashcroft and N. D. Mermin, *Solid State Physics* (Holt, Rinehart and Winston, 1976).

[141] P. Maher, L. Wang, Y. Gao, C. Forsythe, T. Taniguchi, K. Watanabe, D. Abanin, Z. Papić, P. Cadden-Zimansky, J. Hone, et al., *Science* **345**, 61 (2014).

[142] L. Faoro and L. B. Ioffe, *Physical Review Letters* **100**, 227005 (2008).

[143] S. M. Anton, J. S. Birenbaum, S. R. O'Kelley, V. Bolkhovsky, D. A. Braje, G. Fitch, M. Neeley, G. C. Hilton, H.-M. Cho, K. D. Irwin, et al., *Physical Review Letters* **110**, 147002 (2013).

[144] S. D. Bennett, S. Kolkowitz, Q. P. Unterreithmeier, P. Rabl, A. C. B. Jayich, J. G. E. Harris, and M. D. Lukin, *New Journal of Physics* **14**, 125004 (2012).

[145] P. Ovartchaiyapong, L. M. A. Pascal, B. A. Myers, P. Lauria, and A. C. Bleszynski Jayich, *Applied Physics Letters* **101**, 163505 (2012).

[146] M. J. Burek, D. Ramos, P. Patel, I. W. Frank, and M. Lončar, *Applied Physics Letters* **103**, 131904 (2013).

[147] Y. Tao, J. M. Boss, B. A. Moores, and C. L. Degen, *Nature Communications* **5** (2014).

[148] E. MacQuarrie, T. Gosavi, N. Jungwirth, S. Bhave, and G. Fuchs, *Physical Review Letters* **111**, 227602 (2013).

[149] J. Teissier, A. Barfuss, P. Appel, E. Neu, and P. Maletinsky, *Physical Review Letters* **113**, 020503 (2014).

[150] T. Taminiau, J. Wagenaar, T. Van der Sar, F. Jelezko, V. V. Dobrovitski, and R. Hanson, *Physical Review Letters* **109**, 137602 (2012).

[151] N. Zhao, J. Honert, B. Schmid, M. Klas, J. Isoya, M. Markham, D. Twitchen, F. Jelezko, R.-B. Liu, H. Fedder, et al., *Nature Nanotechnology* **7**, 657 (2012).

[152] A. Dréau, P. Spinicelli, J. Maze, J. Roch, and V. Jacques, *Physical Review Letters* **110**, 060502 (2013).

[153] H. J. Mamin, M. Kim, M. H. Sherwood, C. T. Rettner, K. Ohno, D. D. Awschalom, and D. Rugar, *Science* **339**, 557 (2013).

[154] T. Staudacher, F. Shi, S. Pezzagna, J. Meijer, J. Du, C. A. Meriles, F. Reinhard, and J. Wrachtrup, *Science* **339**, 561 (2013).

[155] S. J. DeVience, L. M. Pham, I. Lovchinsky, A. O. Sushkov, N. Bar-Gill, C. Belthangady, F. Casola, M. Corbett, H. Zhang, M. Lukin, et al., *Nanoscale NMR Spectroscopy and Imaging of Multiple Nuclear Species*, arXiv:1406.3365 (2014).

[156] S. Sendelbach, D. Hover, M. Mück, and R. McDermott, *Physical Review Letters* **103**, 117001 (2009).

[157] X. Du, I. Skachko, A. Barker, and E. Y. Andrei, *Nature Nanotechnology* **3**, 491 (2008).

[158] X. Xu, W. Yao, D. Xiao, and T. F. Heinz, *Nature Physics* **10**, 343 (2014).

[159] R. de Sousa, *Electron Spin as a Spectrometer of Nuclear-Spin Noise and Other Fluctuations*, vol. 115 of *Topics in Applied Physics* (Springer Berlin Heidelberg, 2009).

[160] S. Kolkowitz, A. C. Bleszynski Jayich, Q. P. Unterreithmeier, S. D. Bennett, P. Rabl, J. G. E. Harris, and M. D. Lukin, *Science* **335**, 1603 (2012).

[161] J. Maze, J. Taylor, and M. Lukin, *Physical Review B* **78**, 094303 (2008).

[162] N. Mizuochi, P. Neumann, F. Rempp, J. Beck, V. Jacques, P. Siyushev, K. Nakamura, D. Twitchen, H. Watanabe, S. Yamasaki, et al., *Physical Review B* **80**, 041201 (2009).

[163] L. S. Langsjoen, A. Poudel, M. G. Vavilov, and R. Joynt, *Physical Review B* **89**, 115401 (2014).

[164] S. Pezzagna, B. Naydenov, F. Jelezko, J. Wrachtrup, and J. Meijer, *New Journal of Physics* **12**, 065017 (2010).